The Dissertation Committee for Hoo Kim Certifies that this is the approved version of the following dissertation:

PATTERNED RESISTIVE SHEETS FOR POTENTIAL USE IN 3D STACKED MULTISPECTRAL REDUCED THERMAL MASS MICROBOLOMETER

Committee:

Dean Paul Neikirk, Supervisor

Andrea Alù

Mikhail A. Belkin

Zheng Wang

Li Shi

PATTERNED RESISTIVE SHEETS FOR POTENTIAL USE IN 3D STACKED MULTISPECTRAL REDUCED THERMAL MASS MICROBOLOMETER

by

Hoo Kim, B.S.; M.S.

Dissertation

Presented to the Faculty of the Graduate School of

The University of Texas at Austin

in Partial Fulfillment

of the Requirements

for the Degree of

Doctor of Philosophy

The University of Texas at Austin

DECEMBER 2013

Dedication

This dissertation is dedicated to all my family and friends who have prayed for me and encouraged me, and to my God, Jesus Christ, who has been unceasingly gracious to me, not to mention patient with the insufficient descriptions I have made about the world He has created.

This dissertation would not have been possible without the constant loving support of my wife Seon Young, my adorable son Bon, and my cheerful daughter Hyang.

Acknowledgements

For having led me safely through all the difficulties and uncertainties of being a Ph.D. student at UT–Austin, I thank my God. He has always guided me down the best paths through the help of many, some of whom I mention here and others I regretfully cannot due to space.

First of all, I would like to express my deep appreciation for the guidance I received from my supervisor and mentor, Dean P. Neikirk. I have thoroughly enjoyed working with him and will miss all of our conversations, which have opened my eyes to the beauty of electromagnetics and the physics behind it. Without his patient support, I would never have been able to finish my task and produce meaningful results in my research.

For their time and helpful research advice, I would like to thank the members of "Team Neikirk," including Dr. Praveen Pasupathy, Ye Chen, Tanuj Trivedi, along with former members Dr. Sheng Zhang, Dr. Jong Yeon Park, and Dr. Joo-Yun Jung. I would especially like to thank Dr. Sangwook Han for his framework in our group research, which led me to the resources that helped formulate my idea. I wish to thank the members of my committee, including Dr. Andrea Alù, Dr. Mikhail A. Belkin, Dr. Zheng Wang, and Dr. Li Shi for the inspirational suggestions they offered from their respective fields. In addition, I thank my previous advisors Dr. Wee Sang Park, Dr. Young-Soo Kim, and Dr. Hyo-Tae Kim at Pohang University of Science and Technology (POSTECH) in Pohang, South Korea, for the advice and support they gave me from the time I entered to when I graduated.

There are unforgettable friends who have encouraged me through the difficulties of Ph.D. life. First, I would like to thank Nancy Ko for having supported me and my family both spiritually and financially since 2002, along with my brothers in Christ, Stephen Ko and Jiksoo Ko, for their constant friendship and encouragement. I thank

Hyunchae Kim and Minhyuk Lee for being the kind of friends with whom I could share my heart. I also thank Jeane Noh for helping edit my writings.

For four-and-a-half years, the Hyde Park Baptist Church was my spiritual family; they provided support to my family when we were struggling. I thank Pastor Hangil Kim and his wife Miyeon Kim, our spiritual leaders and supporters. I also appreciate all the kindness, encouragement, and financial support the Hyde Park English ministry provided to my wife and me when we were going through financial hardship. I must also mention Mark Josephus and InSon, who have consistently shown their love and compassion for us from the beginning. I have deeply appreciated Mark's consistent greetings and prayers for me even while I studied and worked away in California.

I would like to thank my late father, Moonil Kim, for his invaluable life lessons and love. He loved our family deeply, sacrificing many things to take care of us as he pursued his Ph.D. I thank my mother, Gapjo Bae, for her abiding support and dedication to my sister and me, and now my wife and kids. Her constant prayers have made me stronger and more secure in God. I am truly grateful for her unconditional love and service. I would also like to thank Bee, my lovely younger sister and best friend, whose curiosity inspires me continually.

I would like to thank my parents-in-law, Kwangsoo Kim and Gumja Shin, who have always cherished their youngest son-in-law. My father-in-law's eager anticipation of my arrival home in glory has been encouraging. I also send deep thanks to all my cousins who have loved me and cheered me on.

I thank my son and daughter, Bon and Hyang, for blessing me in more ways than I can count. Finally, I thank my wise and lovely wife, the helper who is more qualified than the woman of Proverbs 31, Seon Young Kim, for walking with me on this journey and for her faith, hope, and love.

HOO KIM
December 2013

PATTERNED RESISTIVE SHEETS

FOR POTENTIAL USE IN 3D STACKED MULTISPECTRAL

REDUCED THERMAL MASS MICROBOLOMETER

Hoo Kim, Ph.D.

The University of Texas at Austin, 2013

Supervisor: Dean P. Neikirk

Patterned resistive sheets (PRS) are resistive sheets with periodic patterns which provide further advantages to the functionality of the microbolometer. This study examines the potential of both single- and double-layer designs to achieve spectral selectivity in both broadband and narrowband absorption in the microbolometer application. First, important design parameters, including rules and processes, are established. These include descriptions of sheet resistance, air gap, material refractive index, thicknesses of dielectric and bolometric layers, mirror, pattern shape and size, and unit cell period. Moreover, interactions among these elements are examined. Second, single-layer designs using dipole and slot PRS are introduced as initial designs for the reduced thermal mass design. Applying holes without changing spectral selectivity are investigated for narrowband application. Moreover, the method to tune the change of spectral selectivity is introduced. Third, newly stacked two-color design is suggested. The out-of-band

transmission and reflection characteristics of the dipole and slot PRS are investigated to increase the absorption of each layer. Additionally, different pattern shapes, such as the circular patch and square patch, are investigated for easier fabrication.

Table of Contents

List of Tables

List of Figures

Chapter 1 Introduction to the use of the microbolometer for infrared detection

Let there be light. The phenomenon of light has been observed and studied for centuries by countless scientists and engineers, who have helped define its modern conception as an electromagnetic radiation [1, 2], of which infrared radiation is a specific component. With its wavelength (λ) measured between 0.3 and 300 μm, infrared radiation lies below (i.e., *infra* the Latin prefix meaning 'below') [3] light's visible spectral region. In 1800, Sir William Herschel discovered and concluded that the energy of light beyond the color red can be shown by temperature measurement using a thermometer [4, 5]. He stated that this energy comprised "calorific rays," derived from the Latin word for heat [5]. The investigations of Kirchhoff (Kirchhoff's law, 1859), Wilhelm Wien (Wien's displacement law, 1893), Stefan and Boltzmann, (Stefan-Boltzmann law, 1897), and Plank (Plank's radiation law, 1900) developed an understanding of infrared radiation further.

Every object emits infrared electromagnetic radiation, which the infrared detector is able to detect. While the invention of man-made infrared detectors have ensued from the discovery of infrared light in 1800, God-made, or natural, infrared detectors have long existed in some living creatures. The pit hole of the snake and the skin of humans are examples of infrared detectors occurring in nature. Figure 1.1 shows the snake and the thermal profiles that the snake detects using its pit hole.

Figure 1.1 Snake's thermal detector and its thermal profile [6, 7].

Two types of infrared detectors can be categorized according to their absorption mechanism: the photon detector and the thermal detector. Photon detectors absorb photons and generate free electrons and holes directly from those photons, whereas thermal detectors absorb photons and generate a temperature change [8, 9]. In manufacturing, thermal detectors can be made to be more compact, use less power, and cost less compared to photon detectors, which require a cryogenic system [8-11]. However, a disadvantage of the thermal detector is its slower response time caused by slowed temperature change owing to the thermal mass of the absorbing structure [9, 10].

Depending on its application and purpose, the design of the infrared detector considers the following aspects in general. First is the target wavelength region of the infrared detector. Infrared detection on the Earth has limited infrared band due to the atmospheric window: the molecules in the atmosphere absorb the infrared radiation, and the infrared energy converts into the vibration of the molecules so that the infrared energy cannot transmit in the certain bands. Therefore, the target wavelength region is also limited to the infrared detector. Figure 1.2 shows atmospheric transmission window in the infrared spectral regions.

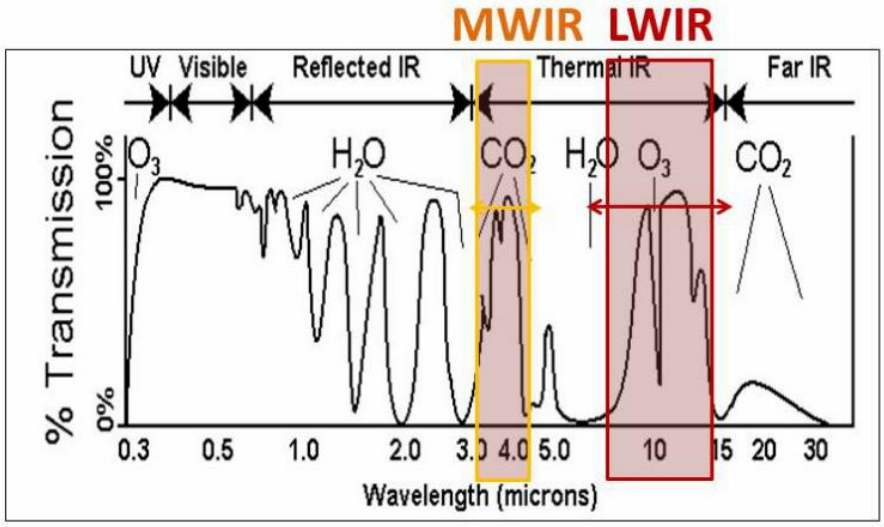

Figure 1.2 Infrared atmospheric window [8].

Due to the existence of the transmission window, the infrared measuring system considers the atmosphere between the radiation source and the infrared detector. The infrared radiation scatters as it propagates through the atmosphere by particles and absorption by gases as well. Figure 1.3 represents the infrared measuring system briefly.

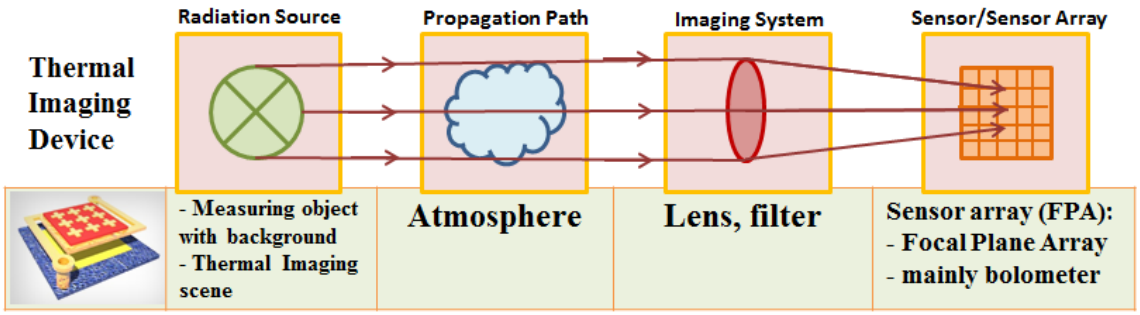

Figure 1.3 Typical structure of Infrared sensors measuring system [8].

There are mainly three infrared spectral regions. First, the short-wavelength infrared region (SWIR) measures 0.35 to 2.5 μm spectral region, which corresponds to a

band of light atmospheric transmission and peak solar illumination, yielding detectors with the best clarity and resolution among the three bands: short-, mid-, and long-wavelength infrared region. Without moonlight or artificial illumination, however, SWIR imagers provide poor or no imagery of objects at 300 K. The mid-wave infrared band (MIR or MWIR: 3 to 5 μm spectral region) can be almost transmitted with the added background noise, lower, ambient benefits. The long wavelength infrared band (LWIR: 8 to 12 μm spectral region) can be nearly transmitted, and it also offers excellent visibility regarding to terrestrial objects. Usually, living objects have a peak emission in the LWIR. Therefore, the LWIR is adequate for applications such as night vision, which acquires more infrared signals from the living object, whereas the MWIR is adequate for applications that detect higher peak emission, such as detectors of engine exhaustion. Therefore, adequate wavelength needs to be considered for the infrared detector design. Table 1.1 shows the infrared region with detail.

Region (abbreviation)	Wavelength Range (μm)
Near Infared (NIR)	0.78-1
Short Wavelength IR(SWIR)	1-3
Medium wavelength IR (MWIR)	3-6
Long wavelength IR (LWIR)	6-15
Very long wavelength IR (VLWIR)	15-30
Far infrared (FIR)	30-100
Submillimeter (subMM)	100-1000

Table 1.1 Division of infrared radiation [8].

There are two types of infrared detectors: one with its own infrared source (active IR system) and another without an infrared source (passive infrared system). The active

infrared detector illuminates the IR source and then captures the reflected infrared signal from the target. Generally, in so doing, the active infrared detector increases the signal-to-noise ratio. However, as a disadvantage, the illumination source can be detected, and this degrades the signal from the target. Another disadvantage is that the system requires more power to generate the source signal; moreover, the system is usually more bulky and complex, whereas the passive infrared detector simply detects IR radiation which is emitted from the target. Although it is less sensitive than the active infrared detector, it provides a simpler, smaller, and a more cost-effective system. Figure 1.4 shows the brief system of both active and passive infrared detectors.

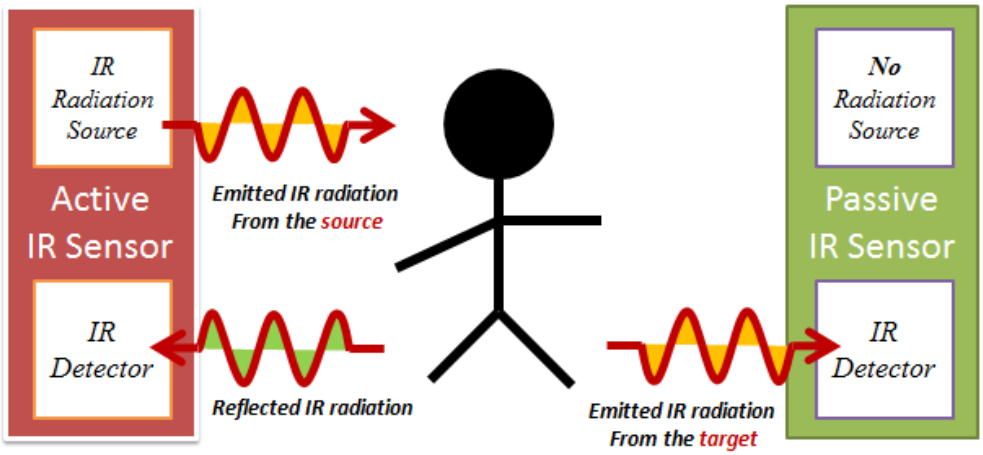

Figure 1.4 Active and passive infrared system.

The infrared detector may or may not contain a cooling system. A cooled detector uses the cryogenic system while usually a photon detector uses the cooling system. As we use the cooling system, it lessens the thermally induced noise; however, it requires the replacement of the cryogenic system every 8,000–10,000 hours, and moreover, the extra cryogenic system causes the detector to be bulky and complex [9, 10]. On the contrary,

the uncooled detector without the cryogenic system, usually thermal detectors, has the advantage of a compact and simpler design as well as longer lifespan. However, this has a lower signal-to-noise ratio and a lower resolution compared to the detector with cooling system. Figure 1.5 shows the schematic of each system.

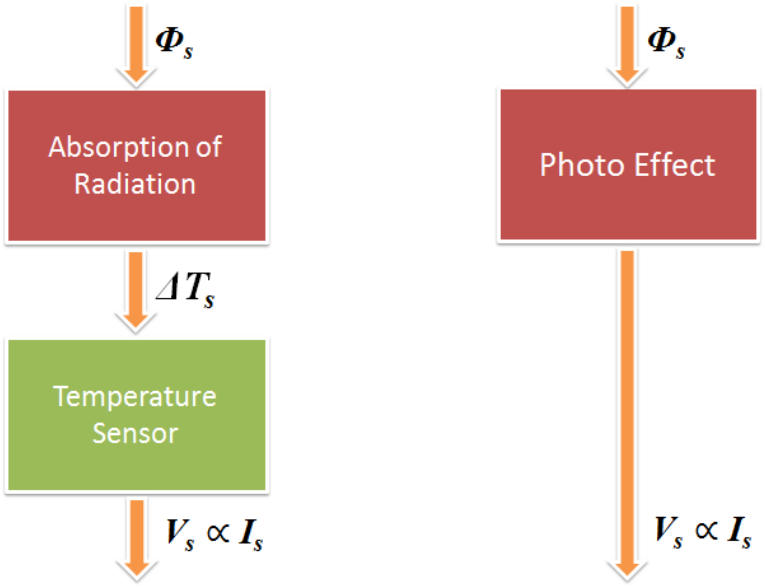

Figure 1.5 System of uncooled (left) and cooled (right) thermal detector [8].

Among many detectors, this study focuses on the thermal detector with the advantage compared to the photon detector; moreover, bolometer, actually, now we call microbolometer due to the size reduction, is one of the most popular and sensitive thermal detectors. The designation "bolometer" partially derives from the ancient Greek word *bole*, meaning "stroke" or "beam of light" (from the verb *ballein*, meaning "to throw") for something thrown, as with a ray of light. Since Samuel P. Langley made the first bolometer using resistive material (i.e., platinum strips) in a Wheatstone bridge, many bolometers are studied for its material and structure [9, 12]. There are several types of bolometers using different material: metal bolometer, thermistor, semiconductor

bolometer, composite bolometer, silicon bolometer, and superconducting bolometer. Among these, the silicon bolometer introduces the *Si* substrate using a narrow *Si* leg, although the early silicon bolometer does not exhibit good performance [9]. However, later in 1983, Honeywell Inc. developed a thermal detector that works in room temperature, which has uncooled imaging arrays that use silicon micromachining technology [11]. Honeywell applied freestanding bridges, which eliminate thermal cross talk between pixels, does not require hybrid bump-bonding of the detector array to an ROIC. In light of this fact, the manufacturing process obtains a better yield and lower cost. Figure 1.6 shows the industrial configuration of uncooled infrared detector manufacturing in the United States. Presently, there are many manufacturers and vendors in worldwide.

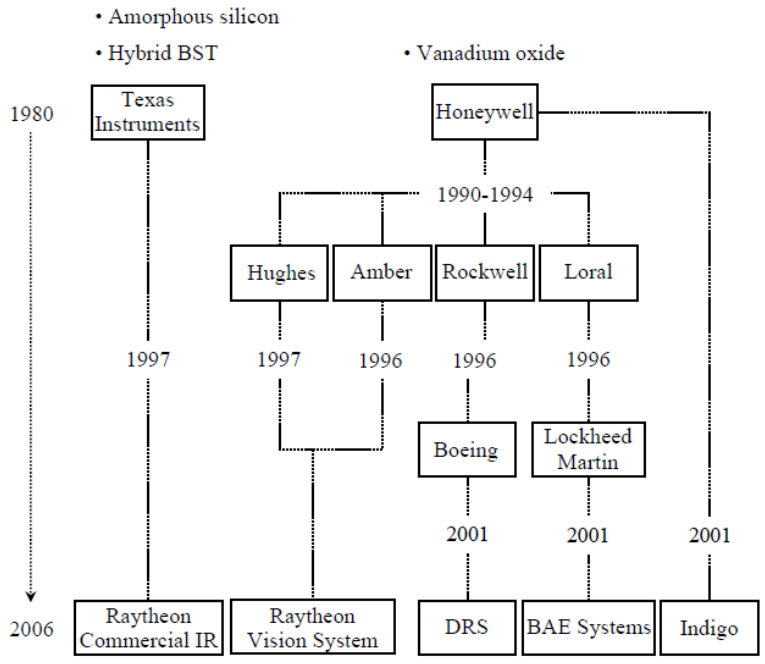

Figure 1.6 Industrial configuration of uncooled infrared detector manufacturer in the U.S.A. [13].

1.1 BASIC PRINCIPLE OF MICROBOLOMETER

A bolometer is essentially a temperature-sensitive resistor. As a typical thermal detector, temperature rises due to the absorption of the incident infrared radiation. The original definition of the microbolometer referred to a bolometer that was much smaller than the wavelength [14]; however, the definition of the microbolometer has become more generalized, and physically small bolometers, even when larger than the wavelength, are also called microbolometers [11, 14]. Like other thermal detectors, a microbolometer, in general, can often lead to an imager that is more compact, requires less power, and is lower in cost compared to photon detectors, which require a cryogenic system [9-11]. However, microbolometers typically have slower response times because of the thermal mass of the absorbing structure which induces slow temperature change [10, 11].

Conventional microbolometers have a bolometric layer with a mirror to increase absorption called the "Salisbury screen." The Salisbury screen was introduced as an electromagnetic absorber during World War II. Salisbury screens use a quarter-wavelength ($\lambda/4$) air gap to maximize wave absorption [15]. In Figure 1.7 (a), a typical microbolometer consists of a resistive absorber, an air gap structure for thermal isolation, and a heat sink, which also functions as a mirror. Figure 1.7 (b) shows the Salisbury screen using a $\lambda/4$ air gap for the target wavelength peak absorption.

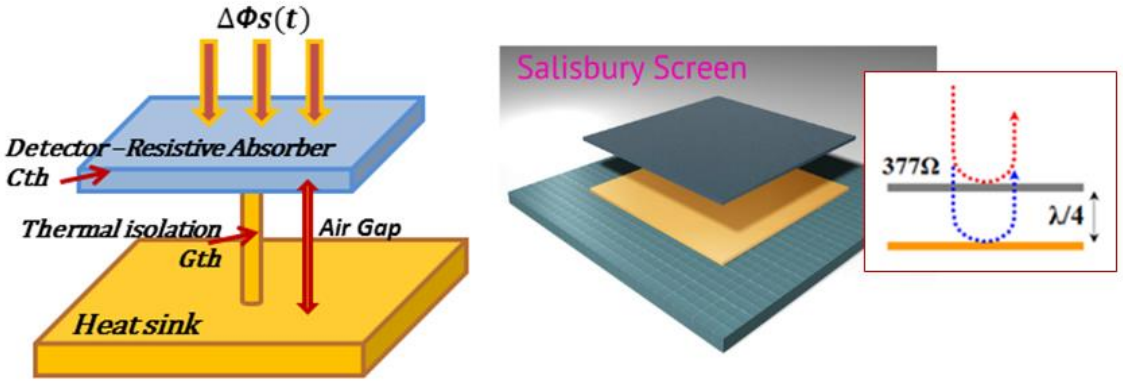

(a) (b)

Figure 1.7 (a) Schematic of microbolometer [11], (b) Salisbury screen.

Resistive absorbers absorb the incident infrared radiation (Φs). Absorbed radiation changes temperature, and temperature changes resistance. The microbolometer then measures changed current and voltage due to the change of resistance. Thermal capacitance (*Cth*) and thermal conductance (*Gth*) are important factors which affect the response speed and the responsivity in the microbolometer. The air gap usually has a λ/4 distance from the Salisbury screen for constructive interference which enhances absorption. Typical design features thus include sheet resistance of the resistive absorber, air gap, and thickness of the dielectric layer. Figure 1.8 shows the power-absorption efficiency of the 10 μm target wavelength. Moreover, absorptions in both the LWIR and MWIR can be seen due to the second mode of the resonance of the Salisbury screen. The 377 Ω sheet resistances (*Rs*) can be achieved using a metal layer.

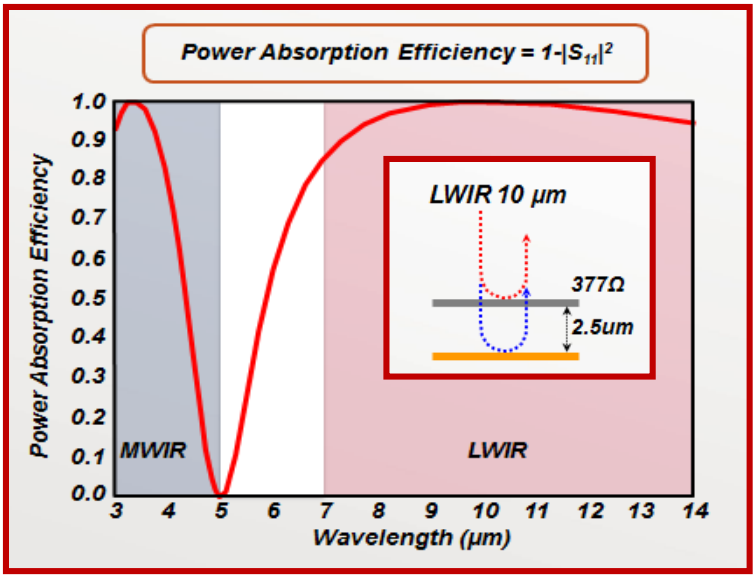

Figure 1.8 Power-absorption efficiency at the target wavelength 10 μm.

The Salisbury screen is an ideal freestanding structure, demonstrating that a realistic microbolometer structure requires a supporting layer. Figure 1.9 (a) shows the conventional microbolometer with supporting layer. Figure 1.9 (b) shows the real microbolometer using this conventional microbolometer structure.

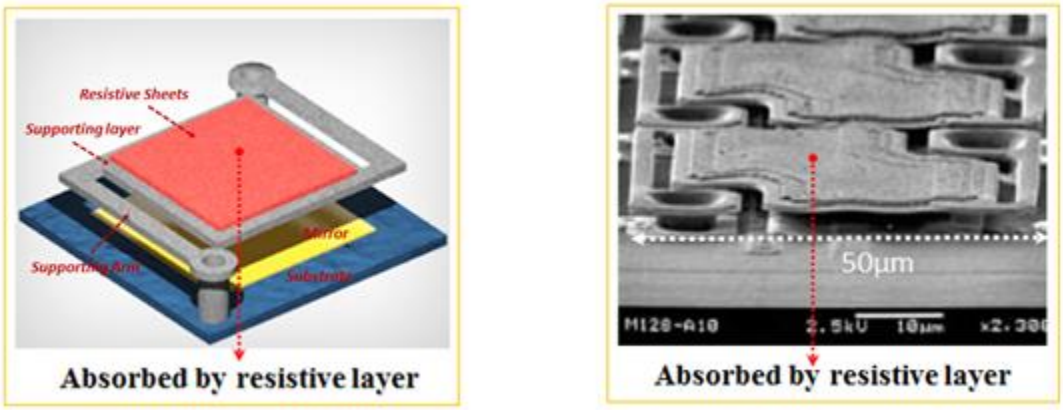

Figure 1.9 Typical microbolometer structure [16].

1.2 MULTISPECTRAL MICROBOLOMETER

Multispectral imaging uses more than two signal bands for target detection. Signals from the different bands contain corresponding unique target signatures; therefore, multispectral imaging provides more spectral information than single-band detection. Figure 1.10 shows the schematics of the multispectral imaging. Multispectral imaging uses the discrete spectral bandwidth ($\Delta\lambda_{BW}$) with spectral gaps ($\Delta\lambda_{Gap}$), allowing it to detect different pixel signals from the different wavelengths.

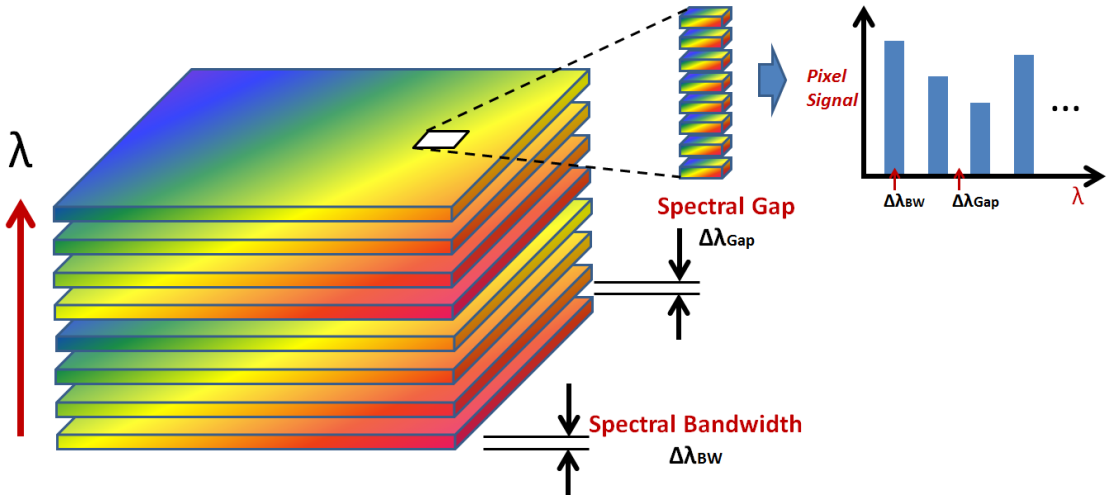

Figure 1.10 Schematics of multispectral imaging.

The following are key advantages of using multispectral sensing. First, multispectral sensing allows rapid and efficient understanding of the scene in a variety ways. Second, multispectral sensing discriminates both absolute temperature and unique spectral signatures of the objects. Lastly, multispectral sensing extracts the objects of interest by subtracting the spurious information. A roadmap of the third-generation microbolometer proposes the multispectral sensing as a key feature in both thermal and

photon detectors [17-20]. There are many implications for using various types of sensors for multispectral image processing in space, military, and commercial applications. Figure 1.11 shows the thermal images using multispectral sensing. Signals from the MWIR and LWIR better extract the signature of the target; the combined feature shows more target information. The LWIR and MWIR bands are especially desirable for infrared multispectral signals because each band contains information about the different temperature emissions from the target. The bands are not limited to infrared multi-bands, and the fusion includes different bands such as visible light.

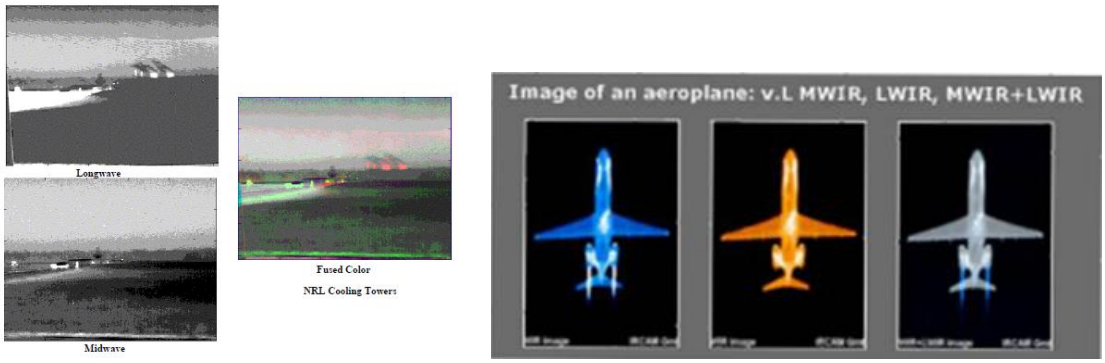

Figure 1.11 Multispectral image using multispectral microbolometer [21].

For multispectral infrared detectors, many papers suggest the use of parallel or cascade focal array structures with two or more unit cells to implement different spectrum absorptions [22-24]. Each pixel targeting the different wavelength absorption is located in cascade. However, there are disadvantages in the integration and fabrication. For one thing, the detector resolution can be degraded due to the area which needs to locate different pixels. Fabrication of the air gap with a different thickness is not feasible in parallel or cascade focal array structures. Therefore, the stacked-layer structure is suggested to achieve multiband absorption using two or three bolometric layers [25-29].

In addition, patterned resistive sheets (PRS), sometimes called frequency selective surfaces (FSS) with resistive patterns, achieve the narrower-band absorption [15]; moreover, they provide robustness of peak absorption wavelength in the fabrication process and reduction of thermal mass. One research group sought to demonstrate micro-actuated mirror which changes the air gap for dual-band absorption [30, 31]. However, it appears that the degradation of the actuated mirror was inevitable [26]. In practice, the stacked structure comprising more than three layers is difficult to fabricate in cases without patterns and with patterns on the layers. Moreover, the structure degrades the performance of the microbolometer—specifically, its absorption efficiency and sensitivity. In addition, other references explain the layer's absorption using periodic structures, such as metamaterial and plasmonic phenomena [32-35]. However, they explain a single-layer structure, and not a multilayer structure. Two-layer or multilayer analyses are conducted in the microwave region for antenna application [36-38]. However, the structure is fundamentally different from two-layer absorptions in the microbolometer based on the metal-conductivity layer.

1.3 REDUCED THERMAL MASS FOR NARROWBAND ABSORPTION

The only way to increase the response speed in the microbolometer is to reduce the thermal mass. The thickness of the dielectric-support layer is the only factor to change the thermal mass in the microbolometer structure. However, the thickness of the dielectric layers is limited due to the minimum mechanical strength necessary to sustain the structure. Some researchers including our group, applied holes in the supporting layers to reduce thermal mass, resulting in a fairly good broadband absorption rate in the LWIR band [39, 40]. These studies focused only on broadband absorption, not

narrowband absorption; therefore, in multispectral microbolometer application, holes cannot be applied directly because they may change spectral selectivity and absorption rates in certain bands.

1.4 PREVIOUS WORK DONE BY ELECTROMAGNETIC DEVICE GROUP

The microbolometer design and fabrication were done by previous members in our group, with Dean Neikirk introducing the microbolometer using an antenna and air gap [41]. This initial design has been the bottom line for both planar mode detector using metal-resistive sheet and the PRS detector.

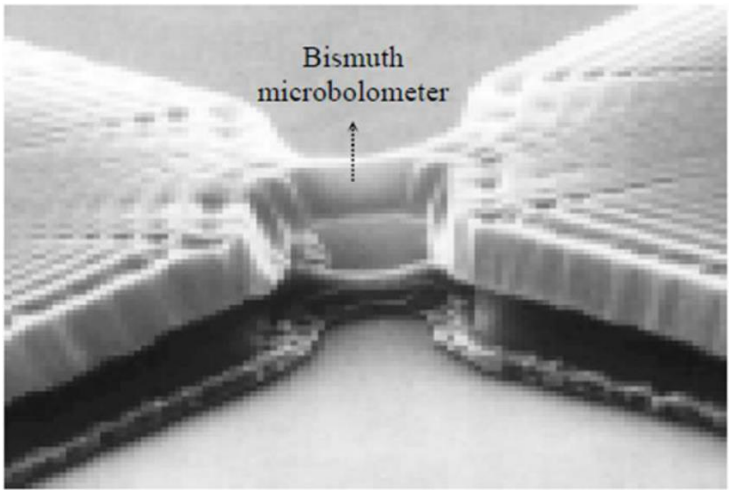

Figure 1.12 Antenna coupled microbolometer using air gap.

Sangwook Han designed the microbolometer using the basic Salisbury screen, and, moreover, the three-color microbolometer with both parallel and stacked structures for the multispectral application [26, 27]. He also introduced the PRS to improve absorption rate to the specific wavelength [42]. Our group suggested converting this broadband absorption into a wavelength selectivity absorber using a dielectric-coated

Salisbury screen (DSS) [27]. Figure 1.13 shows the structure of the dielectric Salisbury screen.

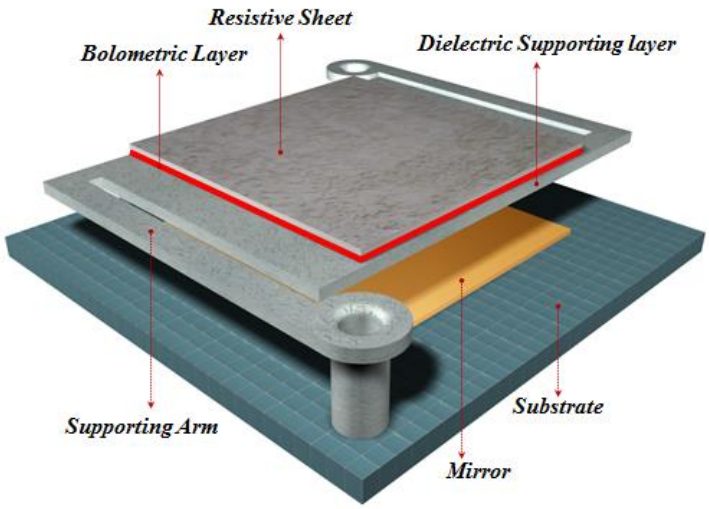

Figure 1.13 Dielectric-coated Salisbury screen.

With DSS microbolometers, our group applied the dielectric layers both on the bottom and top of the metal absorber. The bottom dielectric layer is required for supporting the bolometric layer and metal absorber. The top dielectric layer is coated on top of the metal absorber. However, the top layer can be removed to reduce the thermal mass with the appropriate thicknesses for peak absorption at the targeted wavelength. Figure 1.14 shows the DSS design and its peak absorption using only the bottom dielectric supporting layer. The thickness of the air gap should be a half-wavelength, and the optical thickness of the dielectric support layer should be a quarter-wavelength. A low-loss dielectric, such as *Ge*, is used instead of the typically more lossy and dispersive *SiNx*. In this specific example, the thicknesses of the dielectric layers and the air gap are tuned to adjust the peak absorption at the 10 μm wavelength.

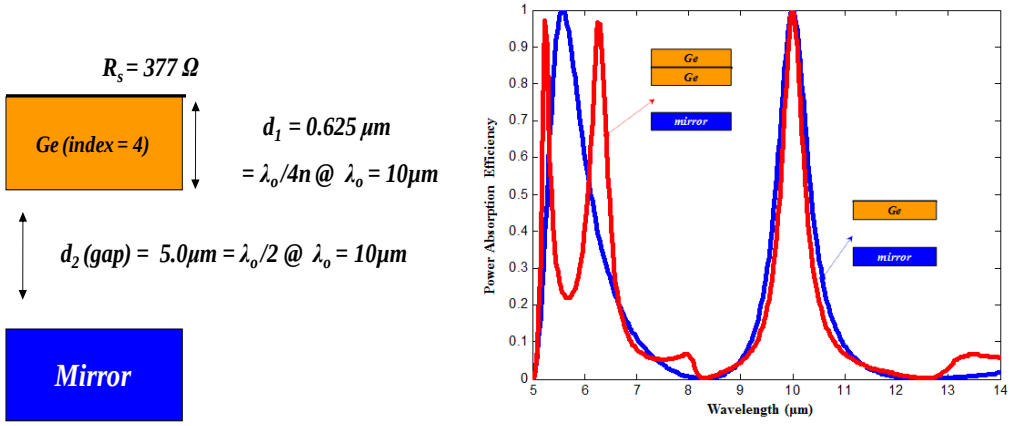

Figure 1.14 Example design of Dielectric Salisbury screen (DSS) and its plane wave calculation for the LWIR [39].

Figure 1.15 shows the fabrication of DSS applying a 2.5 μm air gap and a dielectric supporting layer. Polymide, PI-2610 and -2611, are used, and the patterning is done by plasma dry-etching. By the oxygen plasma ashing process, an air gap in excess of 5 μm can be fabricated.

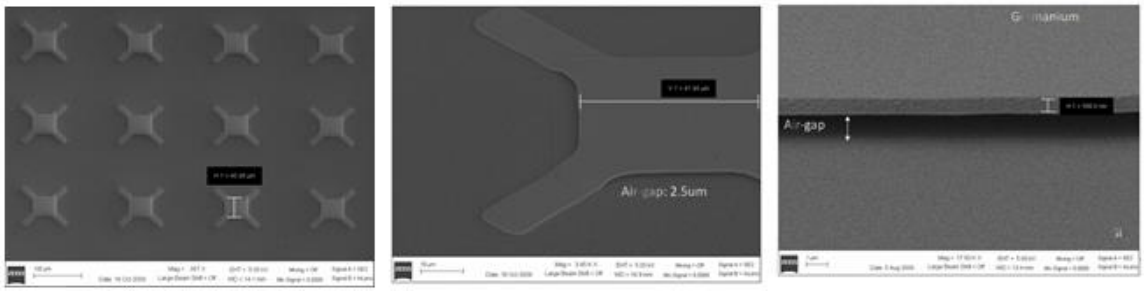

Figure 1.15 Pixel fabrication for DSS with air gap [39].

For the purpose of multispectral sensing, more than two color absorptions are required. Salisbury screens can be designed to use in a three-color-tiled pixels side-by-side on a focal plane array. Each pixel absorbs in a different peak absorption wavelength in the LWIR. Figure 1.16 shows the pixel profile with different tuning parameters such as

air gap, sheet resistance, and a *Ge* layer thickness of top and bottom layers to implement different peak absorption. In the LWIR, the 8, 10, 12 μm peak absorptions are achieved with a relatively narrowband. It is difficult to find the optimal parameters with general rules; therefore, our research group has also applied a genetic algorithm to optimize these design parameters.

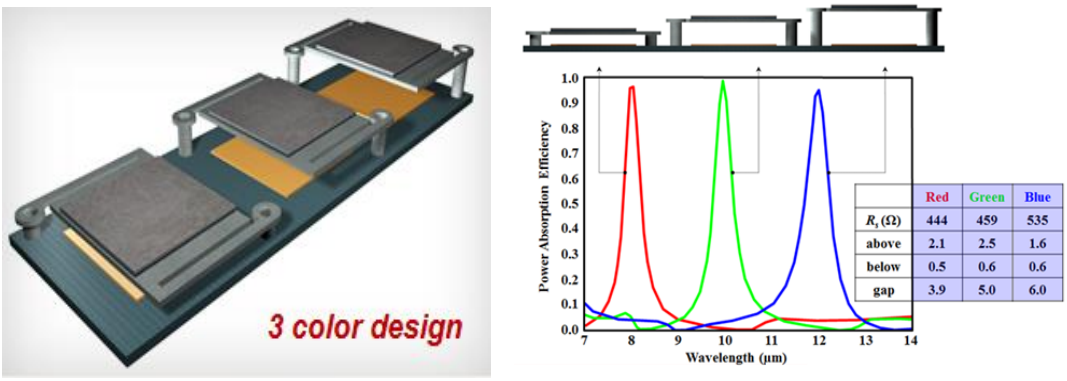

Figure 1.16 Three color pixel design at 8 μm, 10 μm, and 12 μm wavelength peaks [26].

There are some drawbacks of the DSS. First, the Salisbury screen has relatively thick dielectric layers for obtaining wavelength selectivity. Therefore, it has a higher thermal capacitance which lowers speed. Second, different thicknesses of sacrificial layers would involve complex fabrication processes with potentially higher cost. Our research group suggested planar mode detector using both metal and resistive sheets to overcome the drawbacks of DSS. Figure 1.17 shows the structure of the planar multimode detectors and patterned resistive sheets.

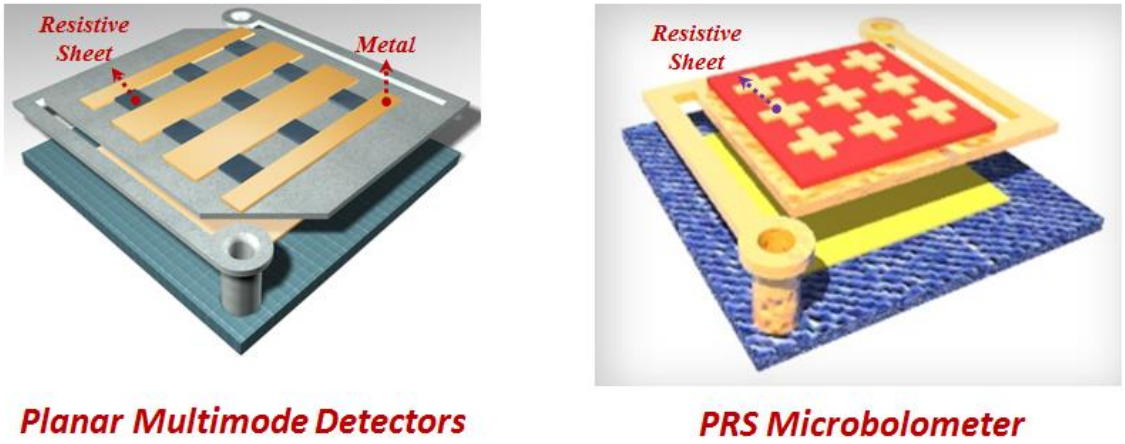

Figure 1.17 Planar multimode detector and patterned resistive sheets microbolometer.

A planar multimode detector consists of metal grids functioning as antennas, an absorbing resistive sheet, and a mirror. Therefore, spectral selectivity is achieved by optimizing the parameters of the metal grids. These metal and resistive sheets in the planar multimode detector can all be resistive sheets. The patterned resistive sheets use only periodic metal patterns on top of a bolometric layer. These planar mode detector and PRS structures have more design freedom compared to the Salisbury screen. This allows us to tailor spectral responses and provide diverse bandwidths by not only changing air gap but also pattern size. Spectral selectivity is more influenced by changing the pattern size than by changing the air gap. For the patterned resistive sheet design, we needed to find the dimensions of the patterns, which change the bandpass characteristics of the incident infrared signal. Moreover, we needed to optimize the sheet resistance and the air gap to yield maximum power absorption at the resonance wavelength. Our group has also discussed the behavior of a cross pattern to produce a polarization-independent frequency-selective absorber and examined the impact of the dielectric loading effect on cross PRS with a low-loss and non-dispersive dielectric layer. The peak absorption

moves according to the refractive index of the dielectric support layer; however, Joo-Yun Jung applied the slot-shaped hole so that the wavelength of peak absorption remained. Moreover, these holes improved the thermal response by reducing the thermal capacitance. Figure 1.18 shows the comparison of the peak absorptions between the with- and without-undercut cases of the dielectric under the pattern.

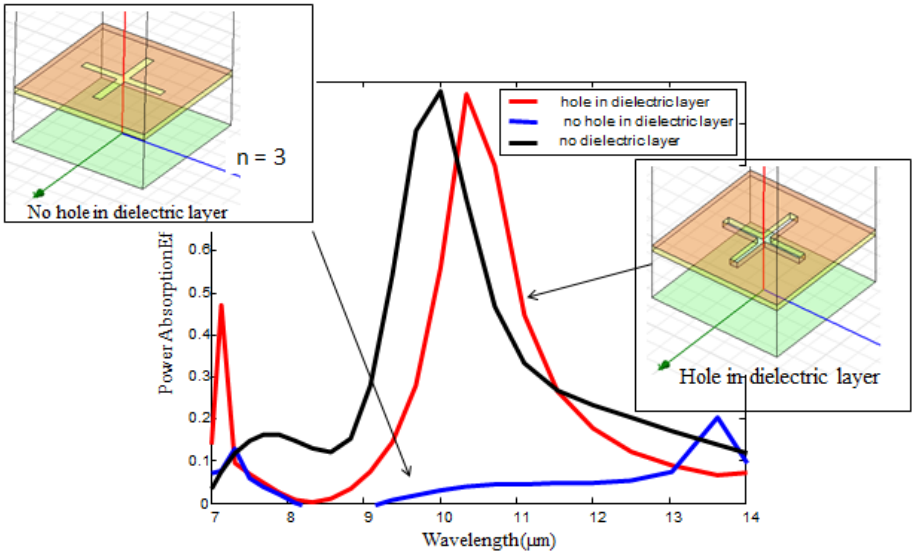

Figure 1.18 Cross PRS with low loss and non-dispersive dielectric layer [39].

Figure 1.19 shows the pixel fabrication of the PRS using holes. The *Ge* layer is deposited by e-beam evaporator, and the plasma dry-etching is used. Two thicknesses of 3000 Å and 6250 Å are fabricated with the deposition rate of 1.2 Å/sec.

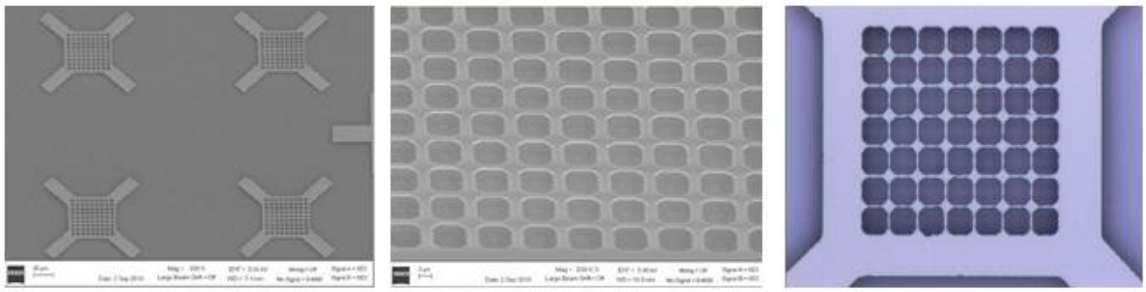

Figure 1.19 Pixel fabrication for PRS using holes [39].

Figure 1.20 (a) shows the DSS using the planar self-aligned process which provides a low deformation membrane with a uniform air gap. Figure 1.20 (b) shows the surface profile measured by the Veeco-Wyko NT 9100 optical profiler.

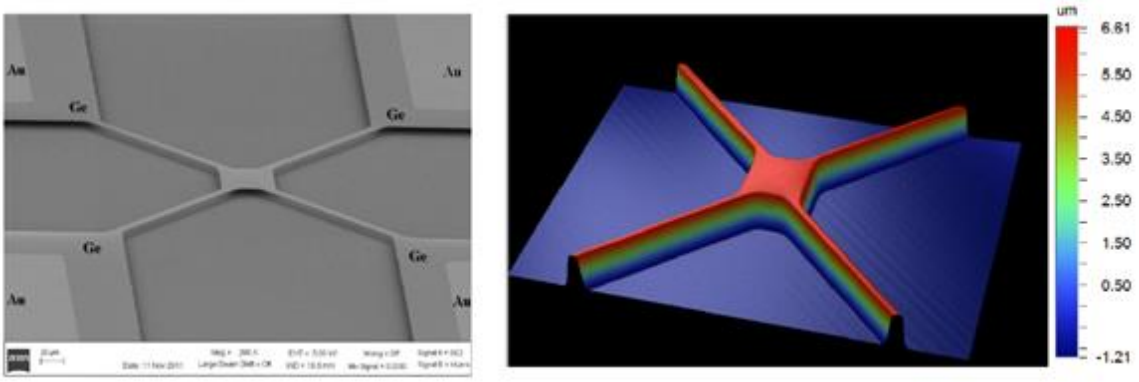

Figure 1.20 (a) Pixel fabrication using planar self-aligned process and (b) surface profile using 3D optical profiler [43].

Our group also measured spectral selectivity using FTIR measurement. Figure 1.21 shows the calculated and measured power-absorption efficiency. In this specific example, 0.6 μm *Ge* supporting layer is applied, and a 5.0 μm air gap is examined. The metal absorber *Cr* is used 400 Ω /□ sheet resistance.

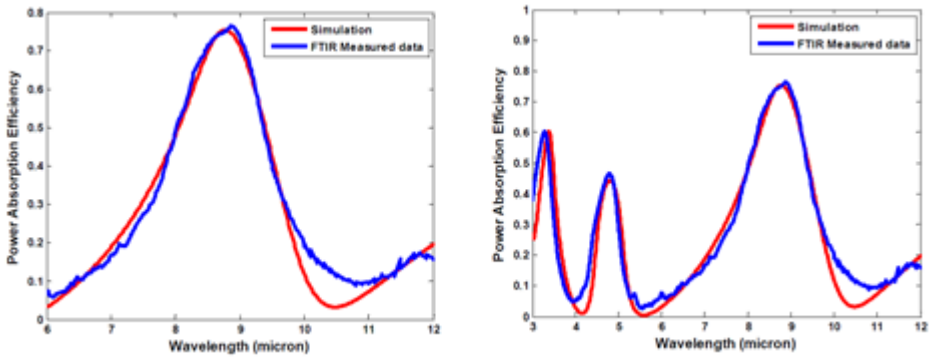

Figure 1.21 FTIR measurement of the pixel fabricated using planar self-aligned process [43].

For real metal layers, the skin effect produces the complex surface impedance that can be quite large in the LWIR band. Figure 1.22 (a) shows the effect of skin depth in the case of real metals. The table introduces the electrical DC conductivity, skin depth at a wavelength of 10 μm, and the complex surface impedance for copper (*Cu*), aluminum (*Al*), and chromium (*Cr*). The calculated power-absorption efficiency of cross PRS is chosen to show the responses of one-skin-depth thickness of real metals as the absorber layer. The metal layers using the thickness between one and three skin depths can act as the absorber layers, and the thick metal layers can still produce excellent absorption in the LWIR. In Figure 1.22 (b), one-skin-depth thickness (333 Å) of chromium absorbs less power and produces a broader bandwidth because the surface impedance for chromium is larger than the desired sheet resistance of $Rs = 1\ \Omega/\square$. Since surface impedances for both copper and aluminum are close to a sheet resistance of $Rs = 1\ \Omega/\square$, they still produce excellent narrow bandwidth absorption in the LWIR.

	Cu	Al	Cr
Electrical conductivity (Ω m)	5.8e7	3.8e7	7.6e6
Skin depth at 10μm	120.6Å	149Å	333Å
When R_S= 1Ω/□, thickness	172.4Å	263Å	1315Å
Z_{surf} (t>>δ)	1.43+1.43j	1.766+1.766j	3.95+3.95j

(a)

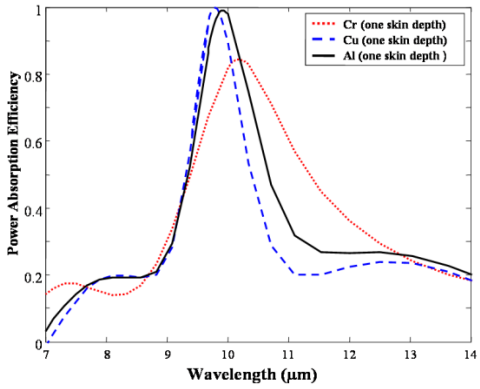

(b)

Figure 1.22 Skin-depth effect of real metals (*Cu, Al, Cr*) [39].

For the thermal-mass–reduced design, the only way to increase the response speed for the microbolometer is to reduce the thermal mass. A finite thickness of the dielectric support layer is required for the mechanical support. This limits the reduction of the thickness for the thermal mass in the microbolometer design. We applied holes in the dielectric support layer to reduce the thermal mass without compromising spectral selectivity. Figure 1.23 shows the design using square holes for broadband application. The added holes with adjusted sheet resistance achieve the broadband absorption compared to the Salisbury screen. In this specific case, a 4 μm by 4 μm hole is applied in the period of 7 μm by 7 μm, and only 67 percent of the temperature sensitive area can produce nearly the same broadband absorption as the 100 percent temperature sensitive area of the one lacking holes.

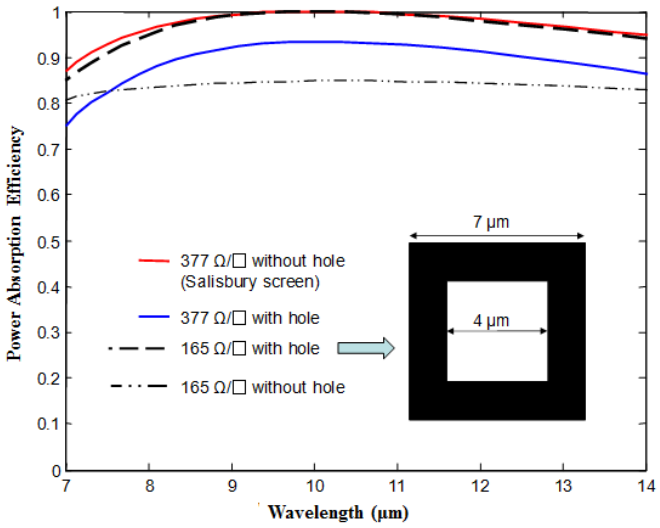

Figure 1.23 Reduced thermal mass design for broadband application [39].

Our group also introduced the stacked multispectral devices, building on its previous research of the vertically stacked two-color Jaumann absorber. A true two-color–stacked microbolometer produces a separate signal for each band in the LWIR. We also demonstrated the wavelength-selective, three-color–stacked Jaumann absorber in Figure 1.24.

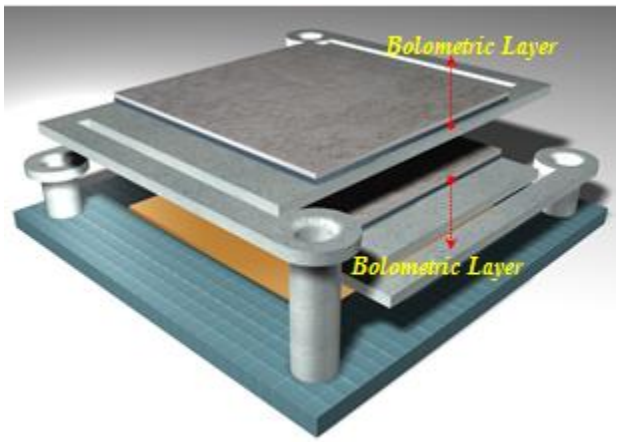

Figure 1.24 Two-color–stacked pixel design using Jaumann absorbers.

The stacked dielectric-coated Jaumann absorber could be used as a vertically integrated pixel with three-color wavelength selectivity. However, both the second peak and the third peak absorb less compared to single layer design. We can expand this stacked design to multicolor microbolometer using the narrowband Salisbury screen and the Jaumann absorber combined with optimized dielectric coating layers. This multicolor stacked design can produce wavelength selectivity in the LWIR band. However, the number of stacked layers is limited because more layers worsen the wavelength selectivity and the power-absorption efficiency. Therefore, placing more than three separate absorbing layers in a stack actually reduces wavelength selectivity and does not produce useful color wavelength selectivity. Figure 1.25 shows both two-color and three-color pixel design using the Jaumann absorber with the optimized parameters.

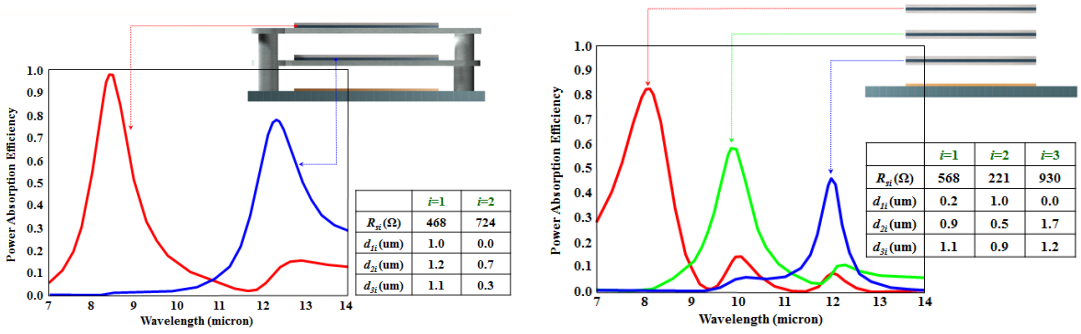

Figure 1.25 Wavelength-selective, two-color (left) and three-color (right) Jaumann absorber [26].

Figure 1.26 shows the fabrication of the two-color–stacked pixel design using the Jaumann absorber.

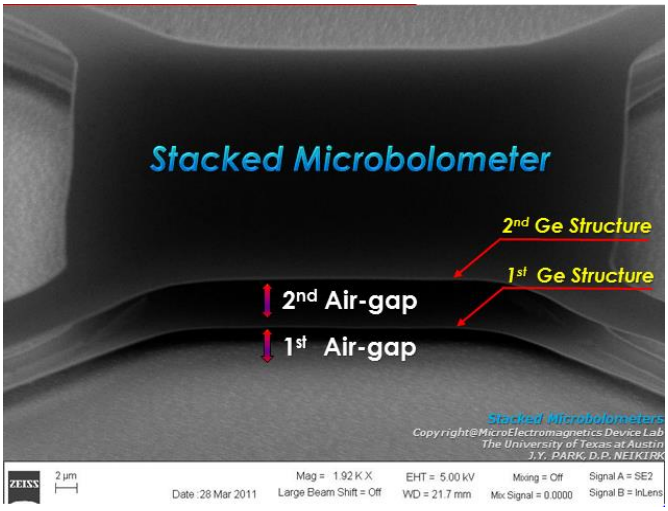

Figure 1.26 Two-color–stacked pixel design using the Jaumann absorber [43].

Figure 1.27 is the flowchart that shows the previous work of our group; moreover, it shows the current and future trajectories of this study. In chapter two, the study introduces the material selection and the design verification. In chapter three, it applies the design rules and shows the reduced thermal design. In chapter four, the two-color microbolometer using dipole and slot-patterned resistive sheets is introduced.

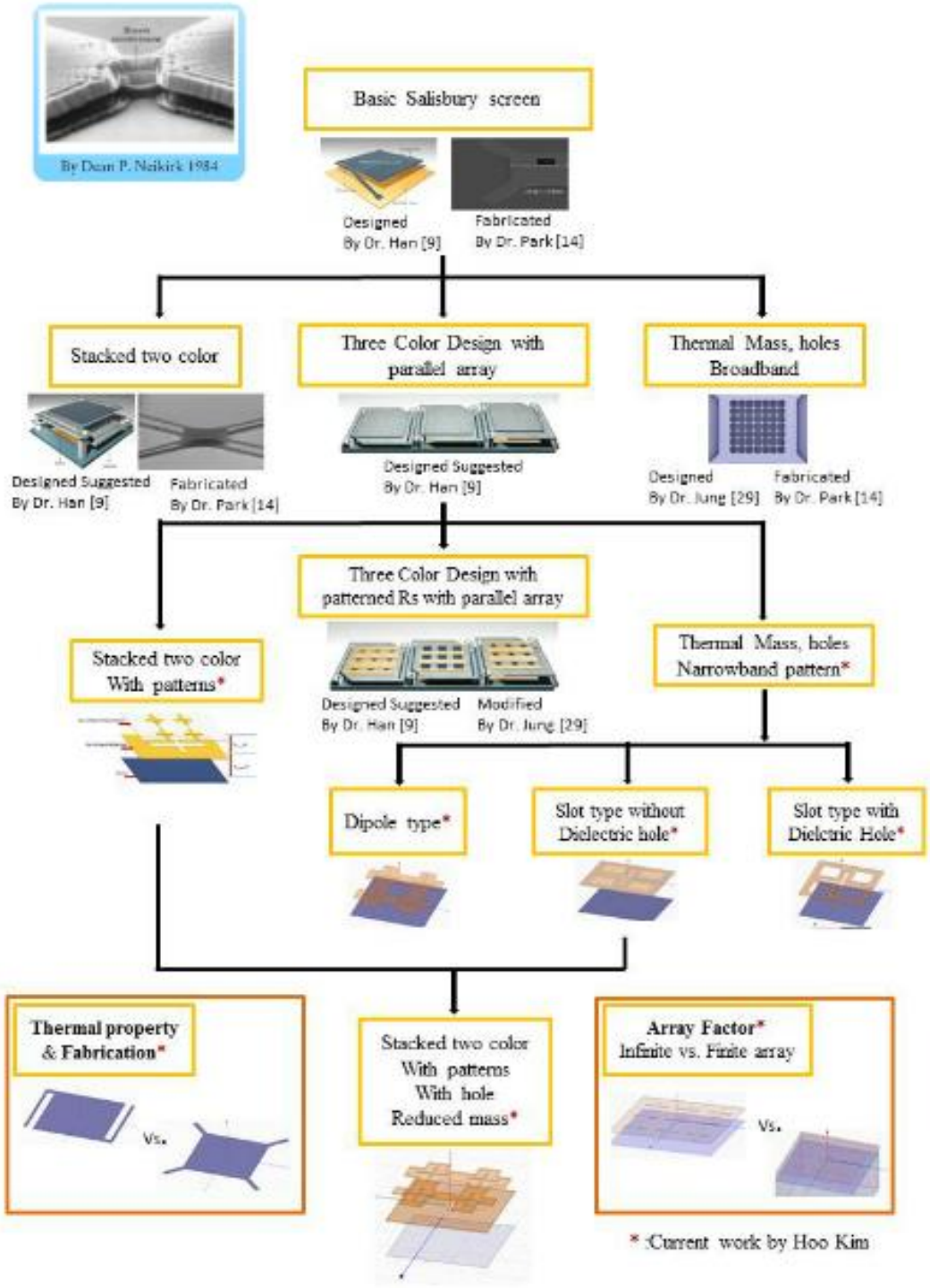

Figure 1.27 Microbolometer design flow.

Chapter 2 Methods: Material Selection and Design Verification

In this chapter, materials for each layer in the microbolometer are introduced and considered; moreover, basic design rules and important parameters are established using patterned resistive sheets.

2.1 MATERIAL SELECTION

This section identifies the principle materials for the microbolometer design. The microbolometer typically comprises four components: a bolometric layer, a supporting layer, a metal absorber, and a mirror. Figure 2.1 shows the typical profile.

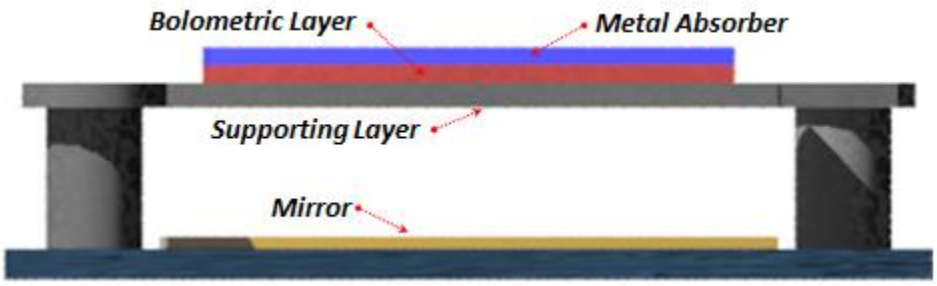

Figure 2.1 Microbolometer layer profile.

2.1.1 Bolometric layer

The bolometric layer uses thermally sensitive resistive sheets to detect heat change, and the material requires a very high temperature coefficient of resistance (TCR) [11]. The bolometric layer is a thin film which measures usually less than 1 μm, deposited upon the supporting layer [9]. When we consider the materials used for the layers of the silicon bolometer, there is a wide range of bolometric materials [11]. For the efficient performance of the signal processing in the infrared focal plane array, the layer of the

thermal sensing has to be built on the CMOS ROIC. Therefore, compatibility with CMOS technology is critical for any thermal sensitive layer of bolometric detectors [9-11]. This study focuses on the two most popular resistive materials which are vanadium oxide and amorphous silicon for the thin films. Table 2.1 shows the commercial state-of-the-art R&D uncooled infrared microbolometer focal plane arrays (FPAs). Moreover, this shows that the *VOx* is the most frequently used material for the bolometric layer in the microbolometer. The *a-Si* is the second most used material that manufacturers use. It is difficult to compare two materials directly due to the different processes implemented by different manufacturers. This study highlights the typical characteristics of the two materials and provides the information based on the limited references.

Vanadium is a metal with a variable valence forming a large number of oxides. Therefore, it is very difficult to maintain the narrowness of the stability range of any oxide such as V_2O_3 and VO_2. This shows that *VOx* can be a complex mixture of different vanadium oxides. However, *VOx* provides a high TCR, which is adequate as a sensitive bolometric layer. Although *VOx* is the most dominant player commercially for the bolometric material, amorphous silicon (*a-Si*) is another good candidate because of its unique characteristics. Unlike *VOx*, the amorphous silicon is made of a single material and therefore presents many advantages. It does not show much variation in its composition, which provides high spatial uniformity at the pixel level [44]. It also appears to have a predictable temperature behavior which allows relatively easy operation as the ambient temperature changes. Moreover, amorphous silicon is believed to have a low power-consumption focal-plane arrays which is adequate for the portable infrared sensor application. Lastly, the thermal time constant of amorphous silicon at least 30 to 40 percent lower in amorphous silicon (10 ms) than in vanadium oxide, thus providing faster response times with the higher frame rates of the microbolometer. Table

2.2 summarizes the advantages and disadvantages of both *VOx* and *a-Si* from the selected references.

Company	Bolometer Type	Array Format	Pixel pitch [µm]	Detector NETD [mk] (f/1, 20-60Hz)
FLIR (USA)	VOx	160x120-640x480	25	35
L-3 (USA)	VOx	320x240	37.5	50
	α-Si	160x120-640x480	30	50
	α-Si/α-SiGe	320x240-1024x768	R&D:17	30-50
BAE (USA)	VOx	320x240-640x480	28	30-50
	VOx (Standard design)	160x120-640x480	17	50
	VOx (Standard design)	1024x768	R&D:17	
DRS (USA)	VOx (umbrella design)	320x240	25	35
	VOx (Standard design)	320x240	17	50
	VOx (umbrella design)	640x480	R&D:17	
Raytheon (USA)	VOx	320x240-640x480	25	30-40
	VOx (umbrella design)	320x240-640x480	17	50
	VOx (umbrella design)	640X480,1024X768	R&D:17	
ULIS (France)	α-Si	160x120-640x480	25-50	35-80
	α-Si	1024x768	R&D:17	
Mitsubishi (Japan)	Si diode	320x240-640x480	25	50
SCD (Israel)	VOx	384x288	25	50
	VOx	640x480	25	50
NEC (JAPAN)	VOx	320x240	23.5	75

Table 2.1 Commercial and state-of-the-art R&D uncooled infrared microbolometer focal plane arrays (FPA) [17].

Bolometer Material	Advantage	Disadvantage
VOx [12]	▪ High TCR of about 2~3 percent/K (5-10 times better than the TCR of most of metal films) ▪ Suitable pixel resistance for CMOS readout circuits at room temperature	▪ NOT a standard material in IC fabrication ▪ Requires expensive equipment to prevent contamination of the CMOS line ▪ Large 1/f noise due to its non-crystalline structure ▪ Narrow stability range [45].
a-Si [46]	▪ High TCR of 2.5 percent/K ▪ High spatial uniformity ▪ Predictable temperature behavior low-power-consumption focal-plane arrays ▪ Thermal time constant 30 percent to 40 percent lower in amorphous silicon (10 ms) than in vanadium oxide sensors [44]	▪ Requires high temperature annealing to reduce their residual stress, which is not suitable for post-CMOS processing for monolithic integration. ▪ Higher 1/f noise than *VOx* due to their non-crystalline structures.

Table 2.2 Summary of the advantages and disadvantages of both *VOx* and *a-Si*.

From the previous comparison, both *VOx* and *a-Si* are not the infrared absorber in my design consideration; the bolometric material using *VOx* and *a-Si* is considered the dielectric material with very weakly absorption in the desired infrared band. This study focuses on the use of *a-Si* for the bolometric layer simply because of the availability of the material's information such as refractive index, which is an important factor to consider for spectral response. The refractive index (n) of *a-Si* is around 3.72 at the wavelength region from 3 μm to 15 μm [47].

2.1.2 Supporting layer

Manufacturer Honeywell employs this membrane type of monolithic bolometer array [9], using Silicon nitride (Si_3N_4) as a supporting layer which is deposited above the *Si* substrate. Silicon nitride (Si_3N_4) is a popular material for MEMs device because of its mechanical property and compatible fabrication. The membrane is supported by the supporting arms. In my design, however, a low loss dielectric, such as *Ge*, is used instead of *SiNx*, which is more lossy and dispersive compared to *Ge*. The extinction coefficient, k, of *Ge* in long wave infrared (LWIR) is almost zero, which indicates lossless. In an application where spectral response is important, *Ge* supporting layer is especially desirable.

2.1.3 Metal Absorber

The metal absorber is the heat absorbing layer. The bolometric layer rarely absorbs the infrared radiation; therefore, this layer works to absorb heat and deliver it to the bolometric layer. Several metals are used for the absorbing layer. In a previous study, our group used and tested the absorption performance of the following materials: *Al*, *Cu*, *Cr*, *Ti*, *TiN*, and *TaN*. This metal layer is designed as an infinitely thin resistive sheet because it reduces the simulation time significantly and makes the design easier. Figure 2.2 shows the profile of the microbolometer design using infinitely thin resistive sheets.

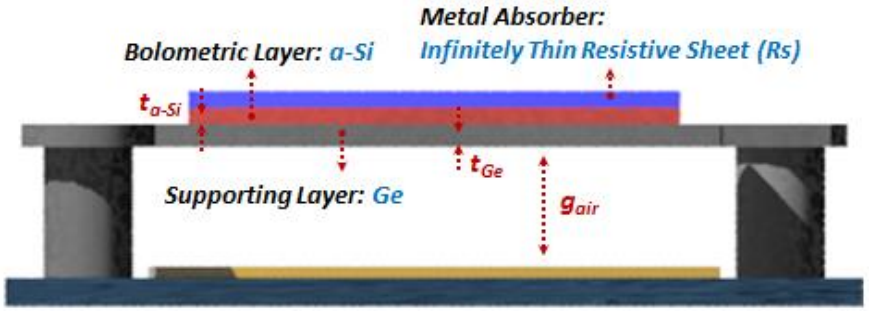

Figure 2.2 Microbolometer layer profile using an infinitely thin resistive sheet.

In this approach, infinitely thin resistive sheets are thought to be comparable to the real metal absorber, which has a finite thickness. However, the sheet resistances of the metals are applied, and later a real metal layer with a finite thickness are applied for a more realistic model.

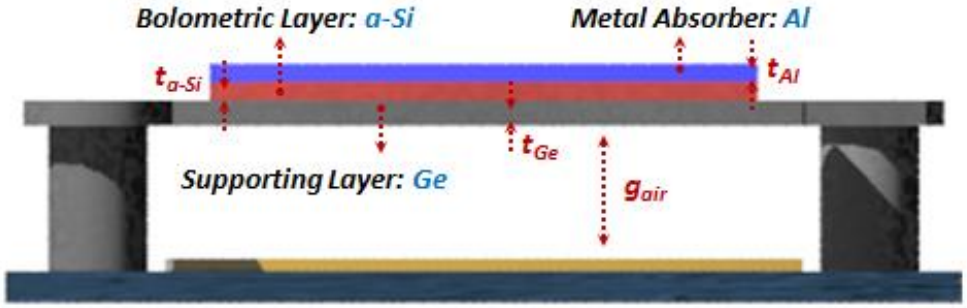

Figure 2.3 Microbolometer layer profile using finite-thickness metal layer.

Skin depth is believed to have adequate sheet resistance. Usually, this happens when we have very low sheet resistance which is comparable to thicker film layer in real metal design. The design study shows that the patterned absorber layer requires a lossy sheet with a sheet resistance close to 1 Ω/□. Moreover, for realistic metal layers, the skin effect produces complex surface impedance if the thickness of the layer is comparable to the skin depth. This skin effect can be simulated in a design using HFSS^{TM}.

2.1.4 Mirror

The mirror layer is used for reflecting the incident infrared radiation and increasing the absorption. The microbolometer pixel structure is built on the Si wafers, into which is deposited a metal layer working as a mirror. Our group fabricated aluminum mirror on the silicon dioxide, SiO_2, layer to implement real mirror and substrate layers.

2.2 DESIGN VERIFICATION

For a more realistic model, the design should reflect the real material characteristics and possible fabrication conditions. This chapter shows the design verification in the use of the materials and introduces reasonable assumptions in the design process. Finally, this study describes the design process and factors which the rules evince.

2.2.1 Simulation: Plane calculation and 3D full wave simulation – HFSS™

This study observes two design tools. One is the plane wave calculation using the transmission line concept. Figure 2.4 shows the plane wave calculation using ABCD matrices. Admittance Y can be the analytic or empirical model for the layer. For the simple resistive sheets, this represents the impedance of the layer.

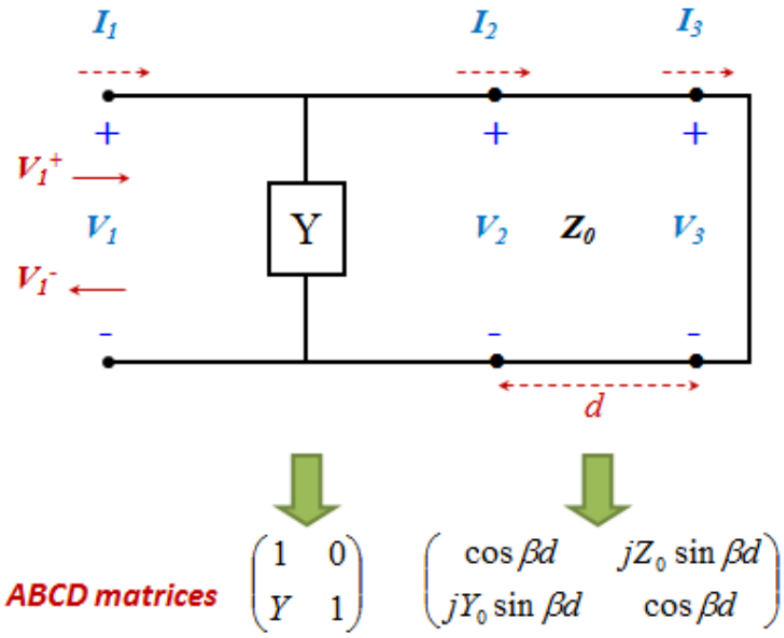

Figure 2.4 Plane-wave calculation using the ABCD matrix.

The transmission line model using the ABCD matrix allows easier power absorption for each layer. For the simple Salisbury screen design including DSS, the plane wave calculation coded by MATLAB is faster and easier. However, it is limited to simpler structure, and the plane wave calculation requires optimization tools such as genetic algorithm to find the optimal design parameters [27]. Another tool is 3D full wave simulation to use commercial software HFSS™. Although plane wave calculation is limited to simpler structures, HFSS™ provides full wave simulation for the various 3D objects. Therefore, HFSS™ has more capability to analyze more sophisticated structures such as patterned resistive sheets on the microbolometer pixel design. However, 3D full wave simulation, including HFSS™, generally exhibits longer simulation time. In HFSS™, this author used the Floquet mode which was shown to provide a fast solution of the periodic structures, such as frequency selective surface (FSS). Figure 2.5 (a) shows the unit cell structure for the basic Salisbury screen in HFSS™, and Figure 2.5 (b) shows

the simulation result using both plane wave calculation and HFSS^{TM} for the tool verification for the further complicated design. The target peak absorption is 10 μm in the LWIR region; moreover, 377 Ω of sheet resistance and 2.5 μm air gap is used for the basic Salisbury screen. Results from two different approaches align well.

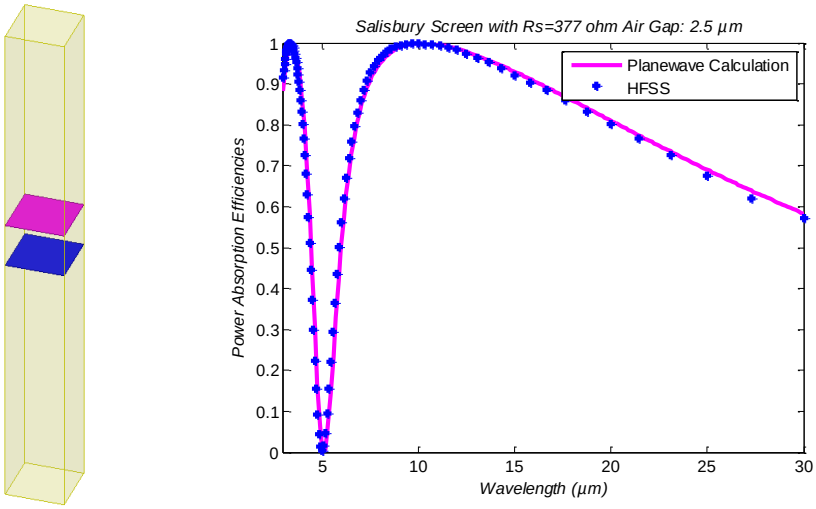

(a) (b)

Figure 2.5 (a) Unit cell structure of Salisbury screen (b) 10 μm peak absorption with *Rs* 377 Ω resistive sheets and 2.5 μm air gap.

The ideal Salisbury screen is a freestanding structure with resistive sheets; however, in real application, the support layer to sustain the resistive sheets is necessary. Figure 2.6 shows the structure with 0.1 μm *Ge* dielectric layer. Due to the dielectric loading, the peak absorption shifts toward the longer wavelength to near 15 μm. Again, the two approaches for the dielectric Salisbury screen exhibit good agreement.

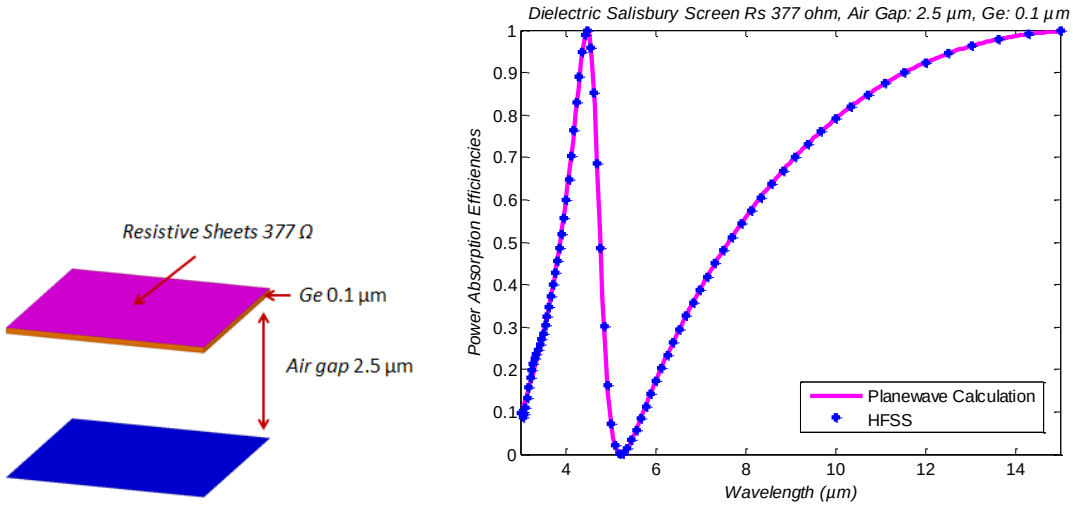

Figure 2.6 Dielectric loading effect with *Ge* 0.1 µm layer.

These two examples in Figure 2.5 and 2.6 confirm that the plane calculation is an efficient way to simulate the simpler structure. Later, this study uses plane wave calculation as a primary tool to find the adequate air gap size and the thickness of the supporting layer.

2.2.2 *a-Si* refractive index

This study found that materials from different fabrications exhibit different properties. The material information of *a-Si* is taken from the reference [47]. Thickness can be varied. A 1000 Å thickness is used in the reference [9], and a thickness exceeding 1000 Å may be possible for the specific structure. In this study, the 1000 Å bolometric layer is considered for the fabrication conditions in the reference. However, it is possible to change the design requirements as it relates to thickness for the specific application while tuning the air gap and other parameters. The refractive index (n) of the *a-Si* from the reference lies between 3.71 to 3.85 in a range of 3 µm to 15 µm [47]. Figure 2.7 (a) shows the plane calculation after adding the 1000 Å *a-Si* layer with the minimum and

maximum refractive index being 3.71 and 3.85 respectively within the range. Figure 2.7 (b) shows the plane wave calculation which uses the average (3.76) of the minimum and maximum values. The results show that the maximum error is 1.43 percent in the extreme selection of the index values at 15 μm. Therefore, for the simpler simulation, this study suggests using the average value 3.76 as the refractive index of *a-Si* whose error is 0.93 percent at 15 μm wavelength as a maximum. If a more accurate model requires, the measured value can be applied to the design; however, in this study, using the average in the given wavelength regions is reasonable.

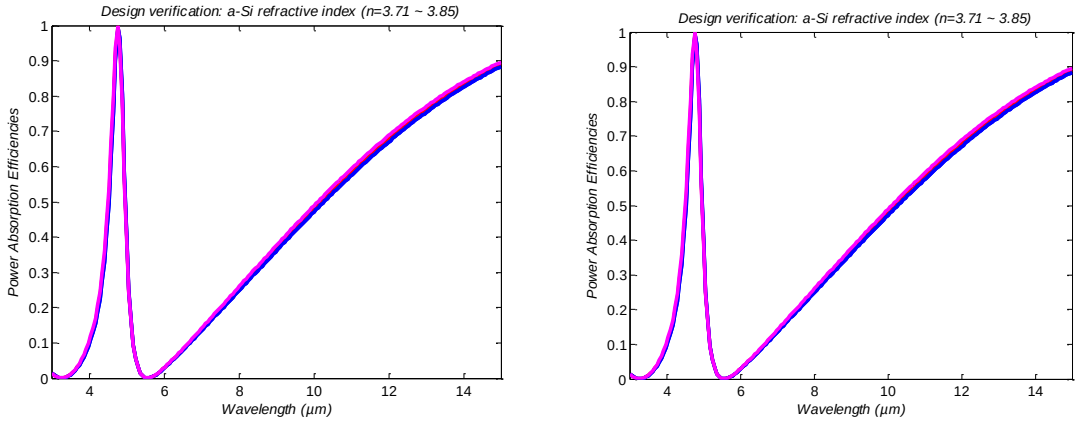

(a) (b)

Figure 2.7 (a) *a-Si* refractive index variation and spectral response (b) using the average.

2.2.3 Dielectric loading effect

A freestanding structure is not eligible for the real microbolometer because the metal absorber and bolometric layer cannot be sustained without the supporting layer. Typically, Si_3N_4 is used for the MEMS structure because of its mechanical properties.

Si_3N_4 is used for the microbolometer by Honeywell. However, Si_3N_4 is dispersive in the LWIR region. Therefore, our group uses Ge, instead of Si_3N_4, which is almost lossless in the LWIR region. Figure 2.8 shows the plane calculation which uses the 1000 Å Germanium layer of basic Salisbury screen with *Rs* = 377 Ω. Germanium has a refractive index n=4.0~4.2 [47]. At 10 μm, the error between n=4.0 and n=4.2 is 4.4 percent. Later, a more accurate refractive index can be utilized for more accurate design. However, in this study, n=4.0 is used.

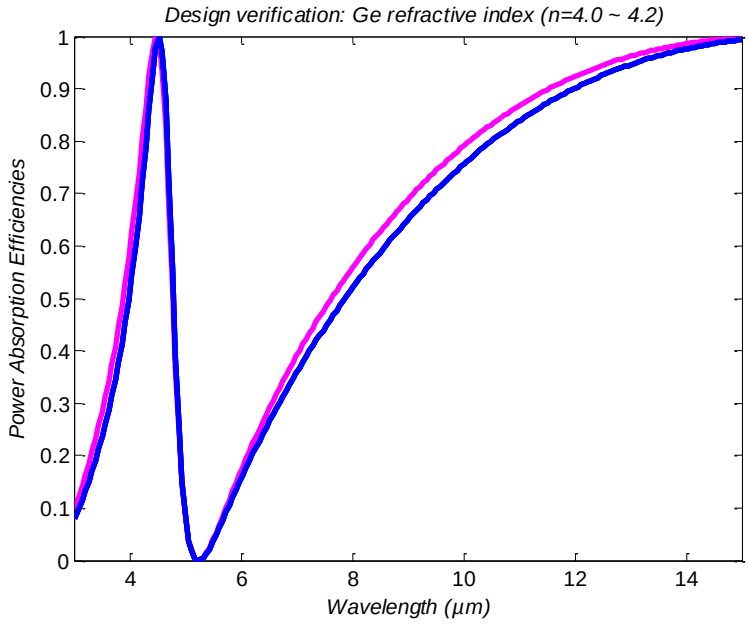

Figure 2.8 Plane calculation which uses 1000 Å Germanium layer of basic Salisbury screen with *Rs* = 377 Ω, Refractive index variation of *Ge*.

For the conventional microbolometer, air gap is one of the critical considerations for design parameters. As air gap is reduced, we can compensate for the shift of peak absorption toward the longer wavelength. In the full microbolometer design, there is a bolometric layer with a finite thickness. Therefore, the thicknesses of the supporting layer

and bolometric layer should be carefully selected for the maximum peak absorption; moreover, the thicknesses of the different layers are limited because of the peak shift of the thicker layer. Figure 2.9 shows the increase of the dielectric loading effect caused by adding both the bolometric layer and supporting layer. The 0.1 μm *a-Si* (n=3.75) is selected for the thin bolometric layer; moreover, 377 Ω and the 2.5 μm air gap is maintained. The peak absorption shifts more in the case of using both *a-Si* and *Ge* compared to the dielectric loading effect only with *Ge*. The peak absorption shifts out of the 15 μm layer with both *a-Si* and *Ge*.

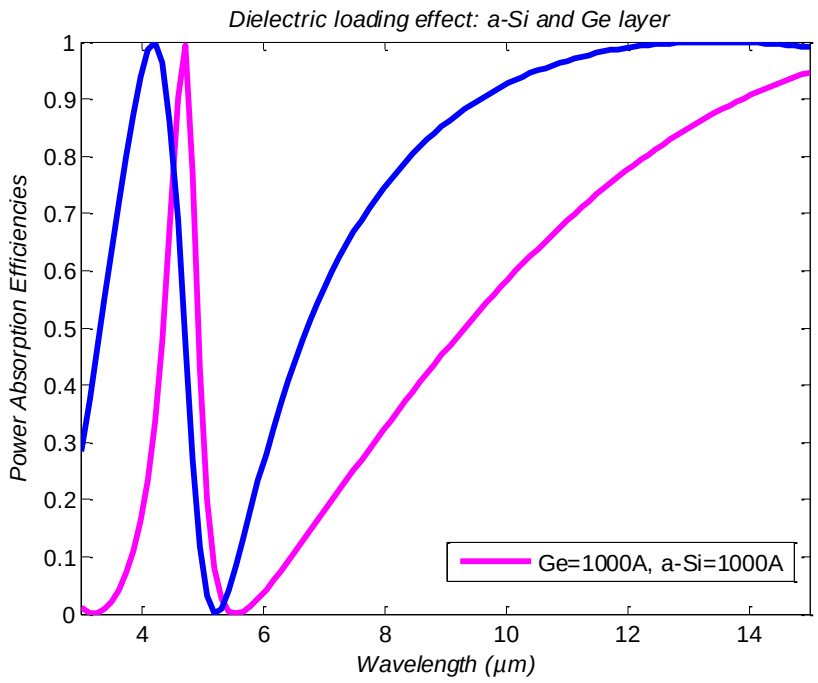

Figure 2.9 Loading effect after adding *a-Si* and *Ge* layers.

2.2.4 Tuning the peak absorption using air gap and layer thickness

In the Salisbury screen, there are mainly two design factors to tune the peak absorption. The first is the air gap, and the other is the supporting and bolometric layer thicknesses.

2.2.4.1 Tuning with only air gap

Using air gap is a simple way to tune the peak absorption, although it is limited by fabrication capabilities to change the gap. *Ge* and *a-Si* with 0.1 μm thickness are used as a thin film in the following examples. Figure 2.10 shows the dielectric effect after loading only 0.1 μm of *Ge* supporting layer. The peak absorption is shifted to the longer wavelength after loading the dielectric layer. The 0.1 μm is a comparably thin layer, just 1/100 of the target wavelength, 10 μm. Therefore, when adding a dielectric layer, one must be aware of the shift of the peak absorption. After reducing the air gap from 2.5 μm to 1.25 μm, the shifted peak absorption is compensated for.

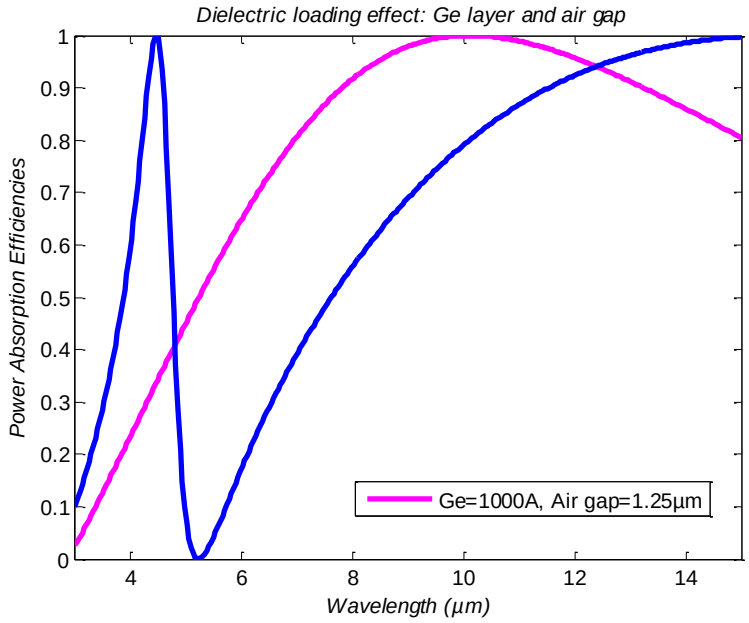

Figure 2.10 Peak absorption tuning with air gap 1.25 μm for *Ge* 0.1 μm loading effect.

Figure 2.11 shows the use the dielectric effect after loading the *Ge* supporting layer and the *a-Si* bolometric layer with 0.1 μm thickness respectively. The shift of the peak absorption is larger than the case of the only 0.1 μm thick *Ge* layer. Therefore, the smaller air gap is required to tune back the peak absorption. The air gap with 0.72 μm provides the 10 μm peak absorption. Although the change of air gap gives more tuning ability, the air gap cannot be close to zero for the thermal isolation aspect; moreover, a narrow air gap of less than 1 μm may be not easy to fabricate for the purpose of compensating the higher loading effect.

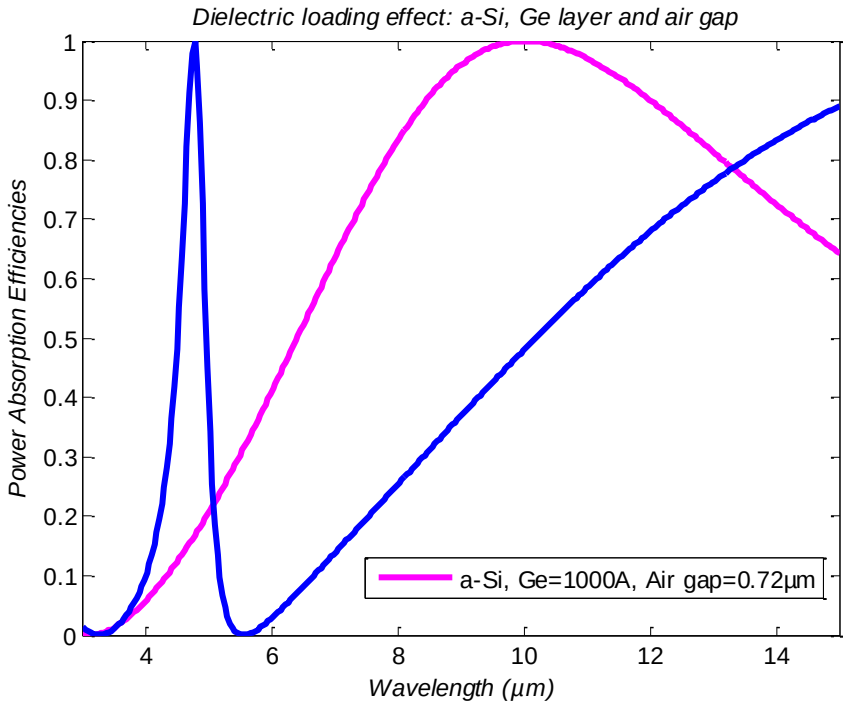

Figure 2.11 Peak absorption tuning with air gap 0.72 μm for *Ge*, *a-Si* 0.1 μm loading effect.

2.2.4.2 Tuning with air gap and other layer thicknesses

The thickness of the air gap and other layers can be designed as a quarter-wave transformer, to tune the peak absorption. This method simply applies the constructive interference to increase the absorption. One study in our group's previous research used one dielectric supporting layer with a mirror. We applied a half-wavelength thickness for the air gap, along with a quarter-wavelength thickness for the *Ge* dielectric layer. Figure 2.12 shows the case with a 0.625 μm *Ge* layer and a 5 μm air gap for the 10 μm peak absorption.

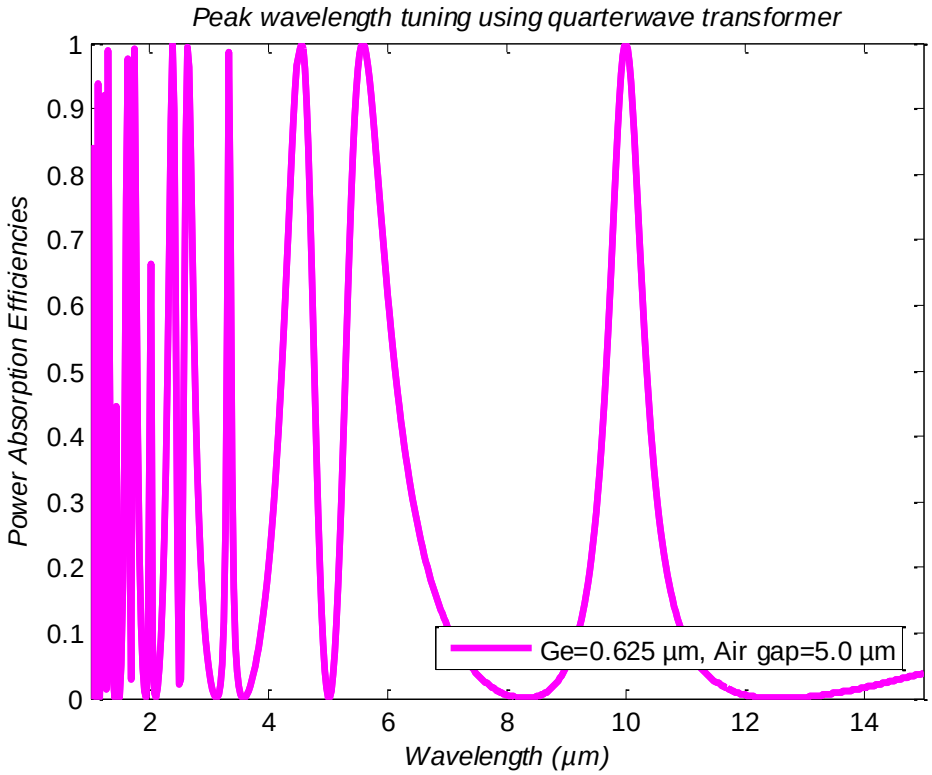

Figure 2.12 10 μm peak absorption using 0.625 μm *Ge* and 5 μm air gap.

Moreover, if the constructive interference is applied, another combination such as 1.25 μm *Ge* and 2.5 μm air gap also works for the 10 μm peak absorption. Figure 2.13 shows the tuned 10 μm peak absorption using a 1.25 μm *Ge* and a 2.5 μm air gap. From the two previous examples, if we have a thinner *Ge* layer, we have narrow bandwidth at the 10 μm wavelength. However, a thinner *Ge* layer generates the second and other resonances below 10 μm more frequently.

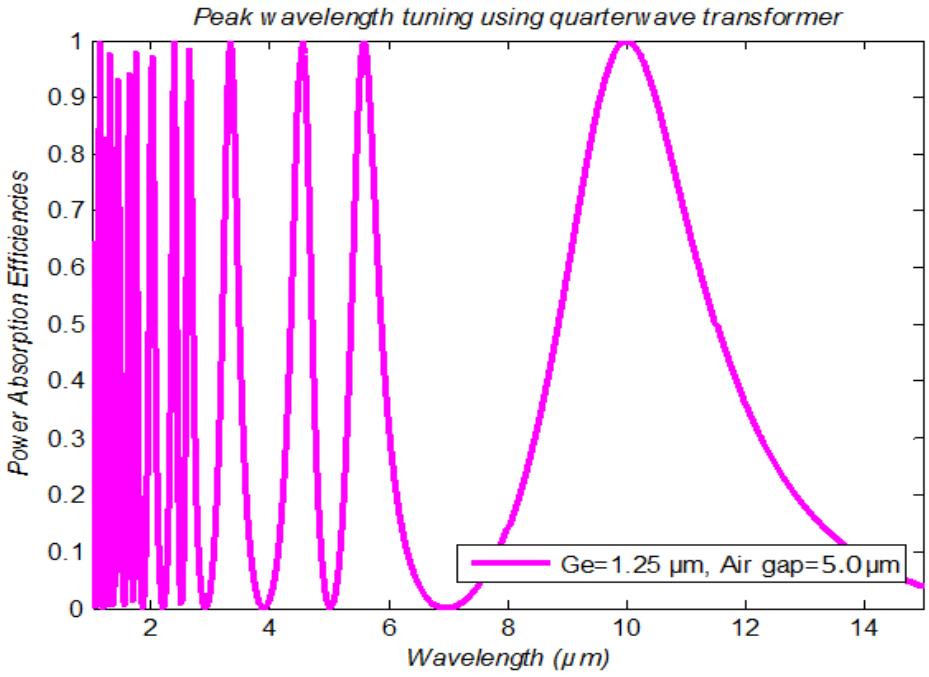

Figure 2.13 10 μm peak absorption using 0.625 μm *Ge* and 5 μm air gap.

However, this study applied two dielectric layers for the bolometric layer and the supporting layer with mirror. The combination of these three layers obtained constructive interference at the resistive sheet layer. In this specific case, the study applied quarter-wavelength thickness for the mirror and found that the other two layers of quarter-wavelength thickness demonstrated maximization of constructive interference at the

resistive sheet layer, thus obtaining peak absorption. Figure 2.14 shows the 0.625 μm and 0.672 μm *Ge* and *a-Si* layer respectively, and the 2.5 μm air gap thickness for the 10 μm wavelength peak absorption.

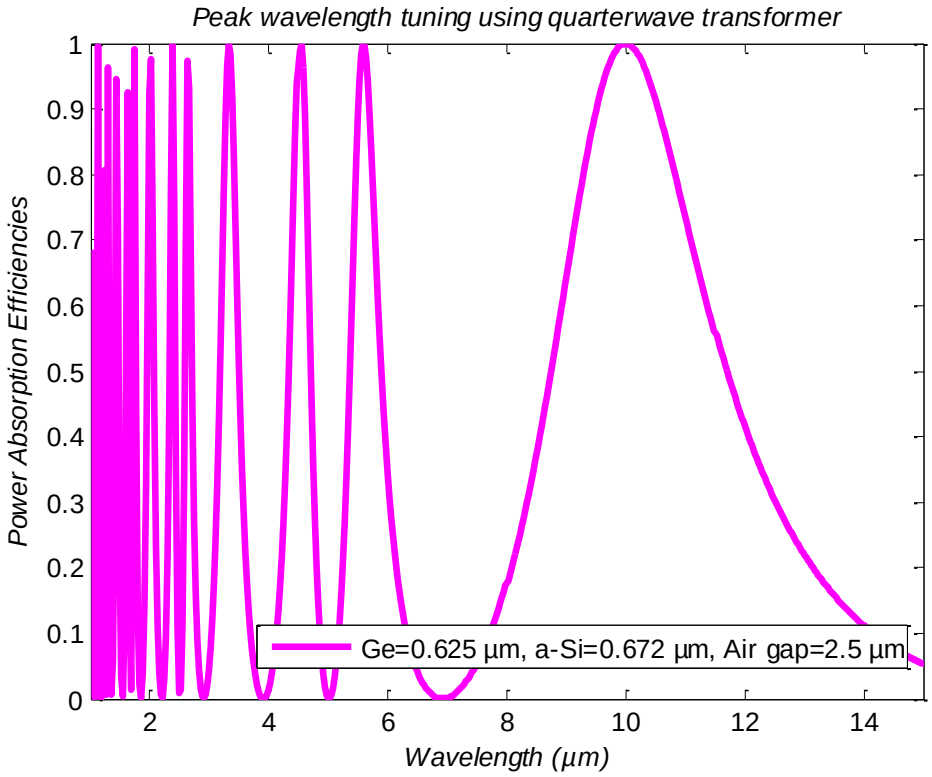

Figure 2.14 10 μm peak absorption using 0.625 μm *Ge*, 0.672 μm *a-Si* and 2.5 μm air gap.

Although changing the layer thickness is a possible way to tune, this method will inevitably utilize a thicker layer for the tuning which degrades the thermal property of the microbolometer. Moreover, more resonances below the target wavelength are not desirable for controlling and obtaining spectral selectivity.

2.2.4.3 Dielectric loading effect in Patterned Resistive Sheets (PRS)

The previous chapter briefly discussed design flexibility using PRS. This section shows the basic PRS design with different types of patterns and how PRS offers more design advantages. Dipole and slot are the two types of patterns for implementing spectral selectivity. In the study of the frequency selective surface (FSS), dipole and slot pattern filters are introduced as a complementary shape for the same wavelength selection [15]. The dipole array case excites electric current, whereas the slot case elicits magnetic current. Although dipole and slot designs are complementary, it is limited to a layer less than 1/1000-wavelength thickness. If the layer is thicker than the limit, the dipole case will have a larger bandwidth, and the slot case will have a narrower bandwidth [15]. When we consider the reflection and transmission coefficient, the dipole pattern shows an out-of-transmission characteristic, and the slot pattern has an out-of-reflection characteristic. However, the PRS is lossy metal with a finite thickness greater than 1/1000; therefore, FSS cannot be directly applied to the microbolometer.

First, we simply start with a PRS with freestanding structure, followed by the supporting layer with a dielectric loading effect. Figure 2.15 shows the dipole PRS freestanding structure and the structures with 0.1 μm thickness of *Ge* and *Ge*, *a-Si* respectively. For the 10 μm peak absorption, a dipole length of 4 μm and width of 0.4 μm are used with a 6.4 μm unit cell size; moreover, 10 Ω is used for the 10 μm peak absorption.

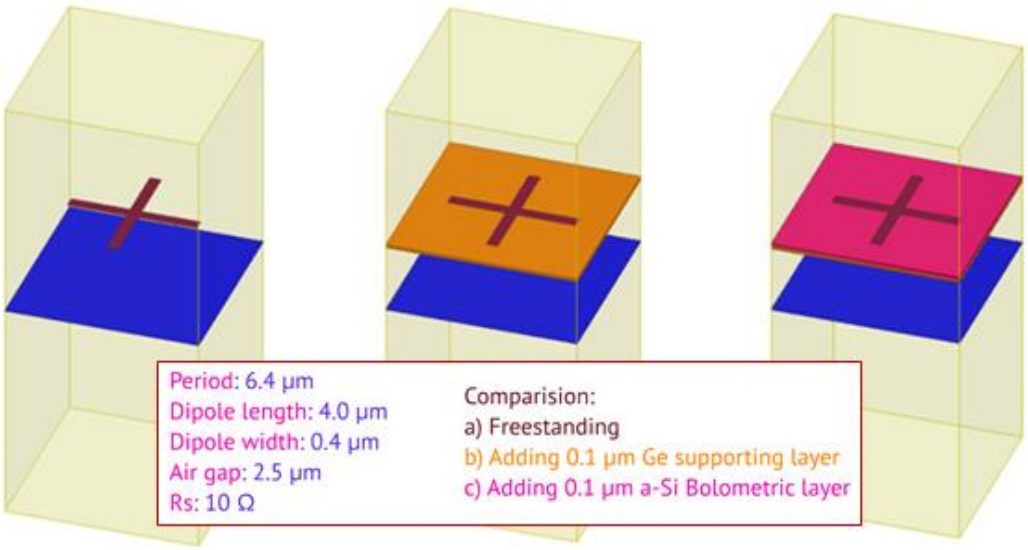

(a) (b) (c)

Figure 2.15 Dipole PRS freestanding and dielectric loading of length 4 μm, width 0.4 μm, period 6.4 μm, *Rs* 10 Ω, air gap 2.5 μm.

Figure 2.16 shows the shift of the peak absorption as the dielectric layer is added in the dipole PRS case. All parameters, such as air gap and PRS, are fixed. As the *Ge* layer and *a-Si* and *Ge* layers are added, the peak absorption is shifted to a longer wavelength region. In addition, the bandwidth is increased.

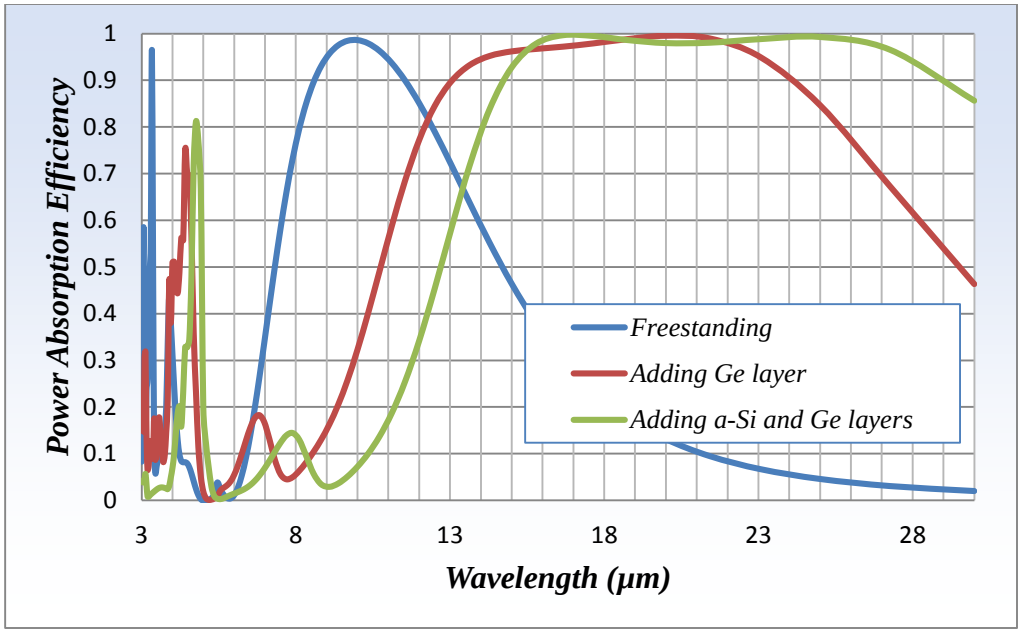

Figure 2.16 Peak absorption change in the dipole PRS structure with dielectric loading effect.

For the slot case, the same PRS size of the dipole case cannot be used. Although the same pattern produces similar peak absorption near 10 μm wavelength, the wavelength of the peak absorption is tilted; moreover, it cannot produce 100 percent peak absorption efficiency. The PRS with dielectric layers are not the ideal metal sheets in the case of FSS; as such, complementary design between the dipole and slot patterns does not work either. The PRS size in the slot case are applied with the following dimensions instead; 4.8 μm length, 0.4 μm width, 6.4 μm period used with *Rs* 1.5 Ω for the freestanding structure is applied for the 10 μm peak absorption. Figure 2.17 shows the dielectric added structures for the slot PRS case.

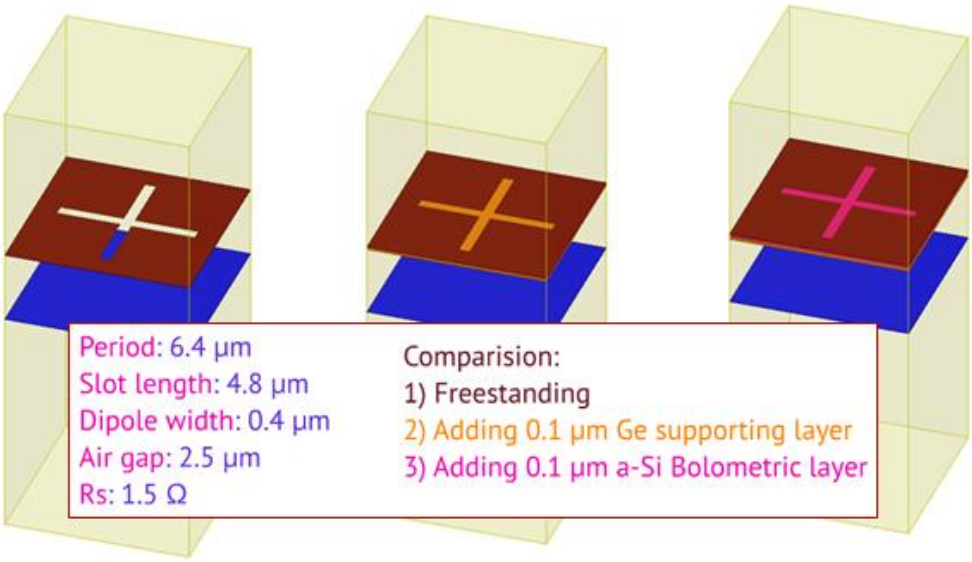

(a) (b) (c)

Figure 2.17 Slot PRS structures with dielectric loading.

Figure 2.18 shows the shift of the peak absorption the dielectric layer is added in the slot PRS case. The peak absorption shifts to the longer wavelength. Moreover, the absorption-power efficiency decreases as the dielectric layers are added.

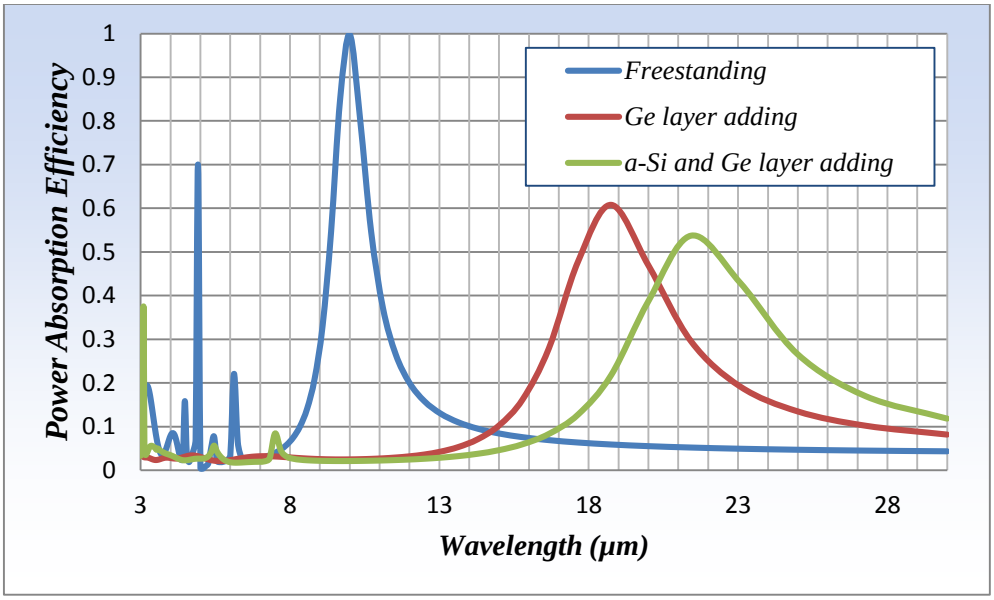

Figure 2.18 Peak absorption of slot PRS structures with dielectric loading.

The slot PRS with undercut structures is examined here. Figure 2.19 shows the slot PRS with undercut, with and without dielectric layers. With the same slot PRS structures, only the undercut is applied.

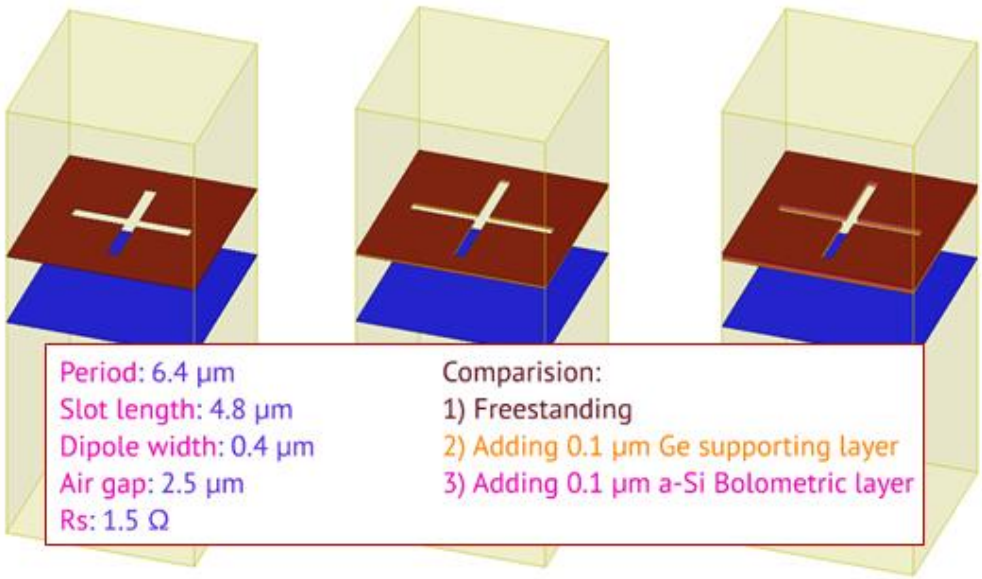

Figure 2.19 Slot PRS with undercut structures with dielectric loading.

In the case of the slot PRS with undercut, the peak absorption with the dielectric loading does not change significantly. The pattern without the dielectric layer moves the peak absorption, unlike the cases of the dipole and slot PRS with dielectric loading. Figure 2.20 shows the smaller shifts of the peak absorption in the slot PRS with undercut structures.

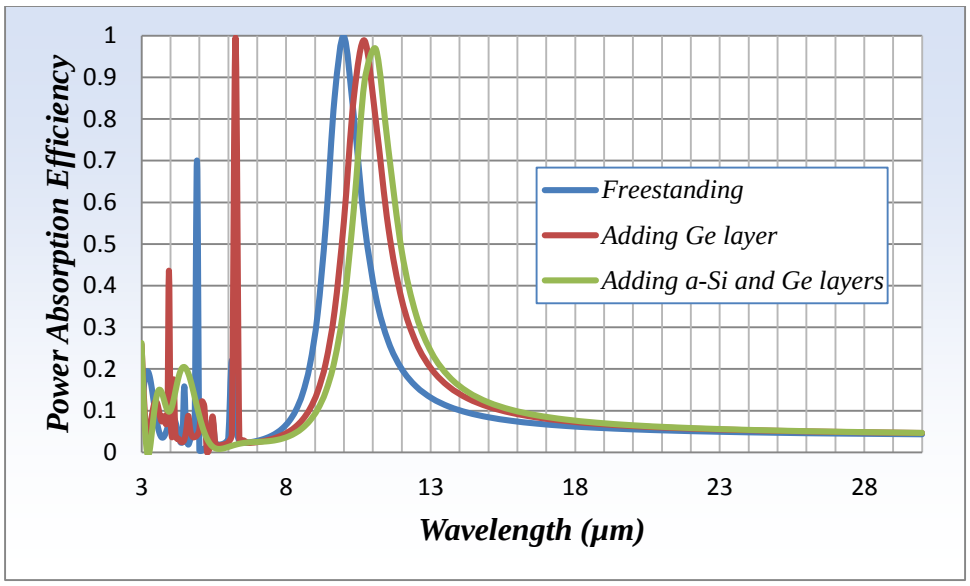

Figure 2.20 Peak absorption of slot PRS with undercut structures with dielectric loading.

As demonstrated in the previous section, the peak absorption can be recovered back to 10 μm as the air gap is reduced. For the case with both dielectric layers, 0.72 μm is the air gap which achieves the 10 μm peak absorption. Therefore, the air gap, 0.72 μm, is reduced under the assumption that doing so can compensate the shift from the dielectric loading effect. For each of the cases of dipole PRS, slot PRS, and slot PRS with undercut, the air gap was changed from 2.5 μm to 0.72 μm. Figure 2.21 shows the result after applying the air gap with 0.72 μm. The peak absorption shifted to the wavelength of

10 μm; however, the power-absorption efficiency was degraded to 0.5. The change of the air gap did not recover to the 10 μm peak absorption.

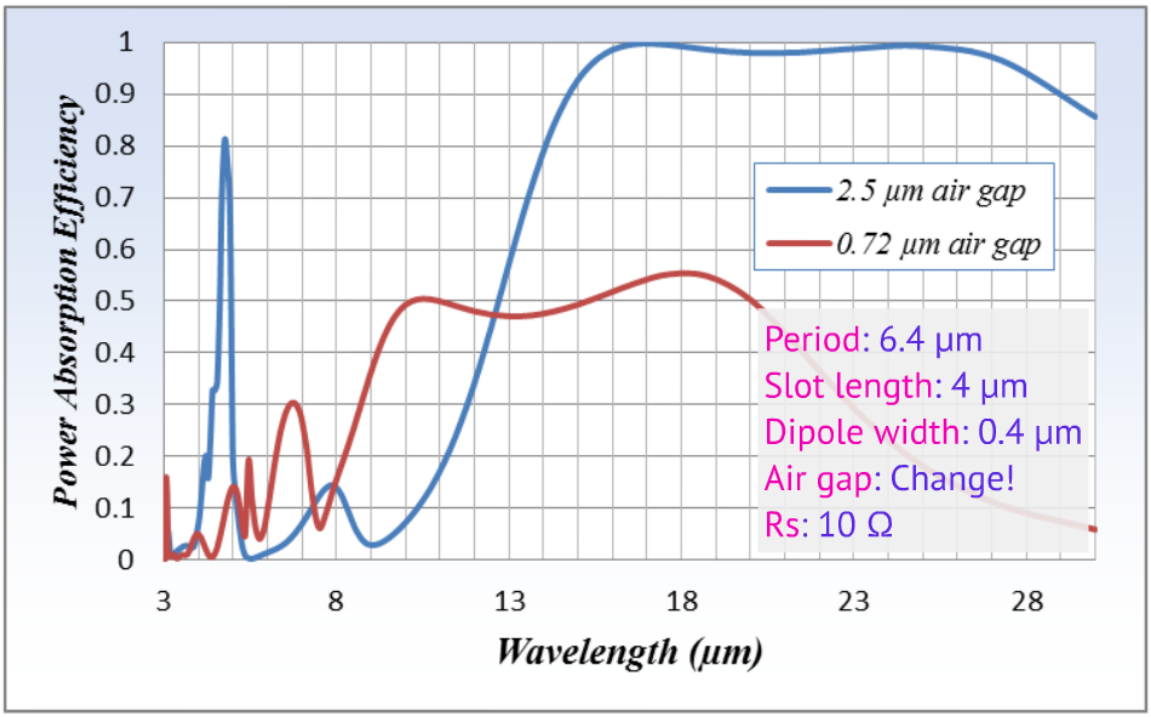

Figure 2.21 Dipole PRS with 2.5 μm and 0.72 μm air gap.

Figure 2.22 shows the result of the case of the slot PRS applying the 0.72 μm air gap. The change of air gap does not move the peak absorption; moreover, the peak absorption remains similar to the case of the 2.5 μm air gap. From this, the dipole PRS is more sensitive for changing the air gap as compared to the slot PRS case.

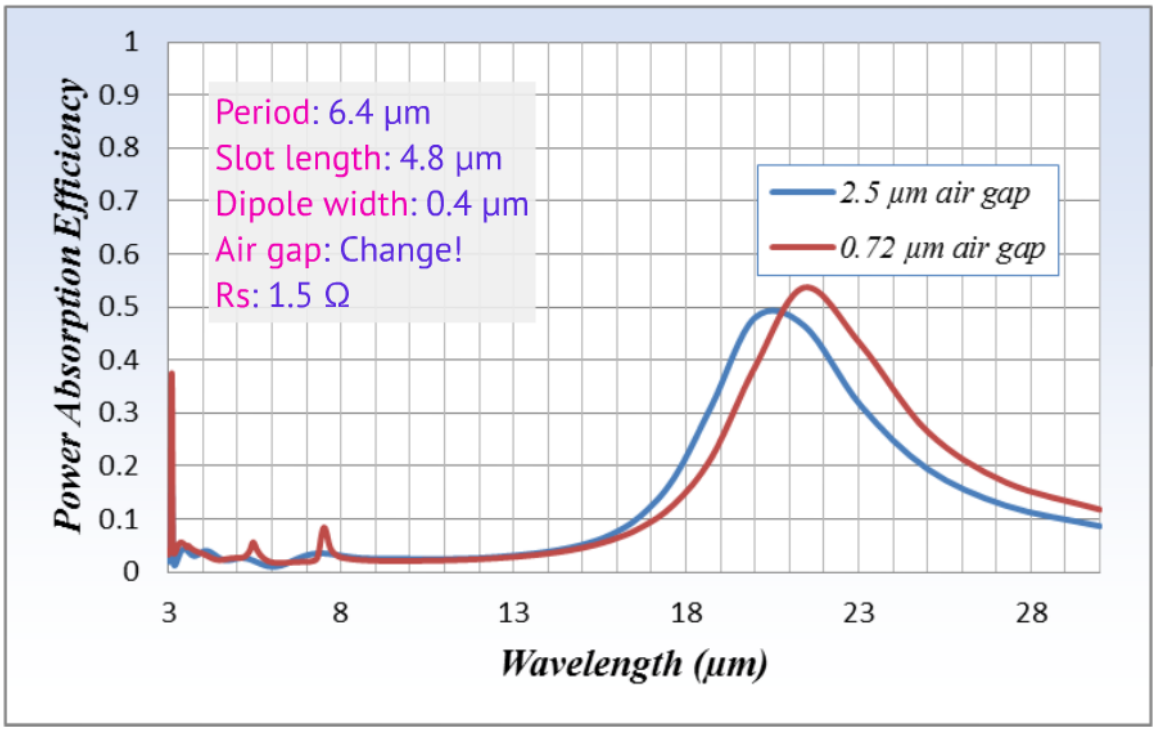

Figure 2.22 slot PRS with 2.5 μm and 0.72 μm air gap.

Figure 2.23 shows the slot PRS with undercut. The peak absorption shows weak shifts for two different air gaps which worked well in the Salisbury screen for wavelength tuning. As a result, the case of PRS with undercut was very weakly affected by changing both dielectric layer and air gap. This may signal the dominance of the PRS to decide peak absorption, which would indicate some freedom to select other parameters for the design. However, this also can be a limitation: the tuning is difficult if the PRS dimension is limited in the given structure. In the design process, it is important to know the possible parameters we can handle and apply so that we may estimate the range of tuning.

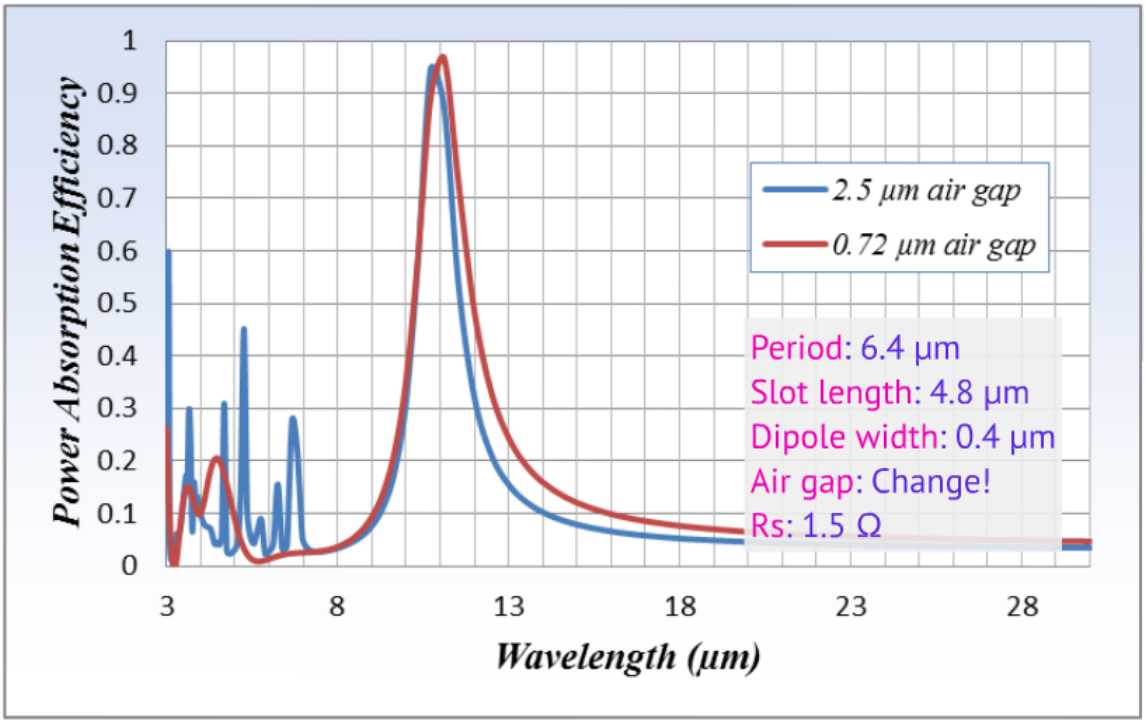

Figure 2.23 slot PRS with undercut with 2.5 μm and 0.72 μm air gap.

2.2.5 Tuning the peak absorption using the PRS pattern size

In this section, the PRS shape and resistive sheet value were studied for the tuning of the 10 μm peak absorption. Beginning with the freestanding structure using the PRS, the test applied the dielectric loading which showed the shift to the longer wavelength region in the peak absorption. The peak absorption, however, was shown unable to be tuned by changing the air gap, which worked in the Salisbury screen case. This represents that the PRS pattern is also affected by the dielectric loading. The dipole PRS and slot PRS without undercut are more influenced by adding the dielectric layer compared to the slot PRS with undercut. In this section, I consider the PRS shape and the value of the resistive sheet as possible parameters for the tuning of the peak absorption.

2.2.5.1 Dipole PRS pattern size study

First, with the same resistive sheet value, 10 Ω, the size of the dipole PRS pattern was reduced because the smaller pattern generates shorter wavelength resonance in its absorption. *Ge* and *a-Si* has a refractive index of around 4 and 3.72 respectively. The study applied the $\lambda_n = \lambda/\sqrt{n}$ relation for the resonance to make a half-wavelength. The length of 2.0 μm and width of 0.2 μm are applied with a 3.2 μm period, which are approximately half the size of the freestanding case. Figure 2.24 shows the air gap change after reducing the pattern size in the dipole PRS structure.

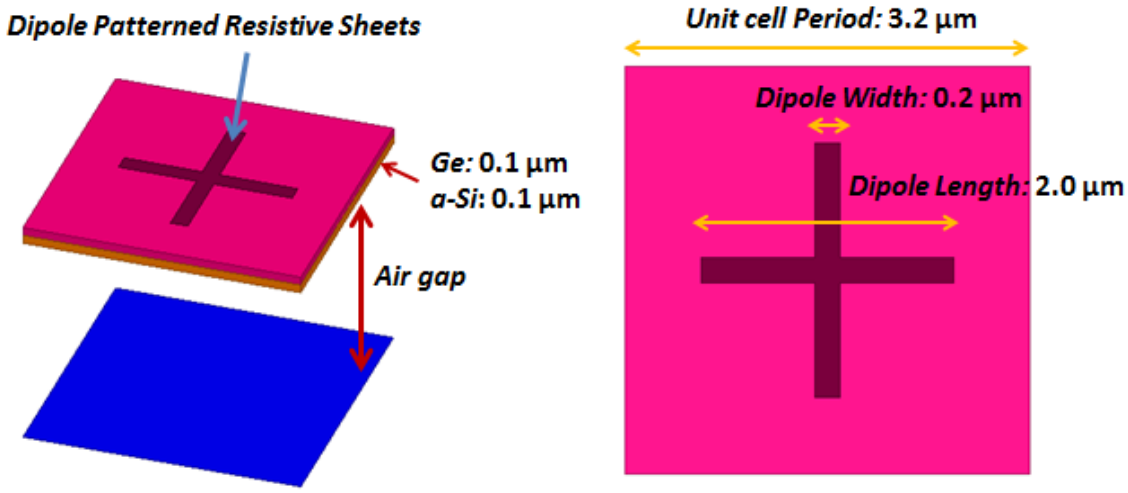

Figure 2.24 Dipole PRS structure with three different air gaps.

The air gap of 2.3 μm is the thickness that excludes measurement of the dielectric layers and is compared to the quarter-wavelength required for peak absorption. The 2.3 μm air gap assumes that the dielectric layers are thin enough not to consider their refractive index and its optical wavelength. *Ge* 0.1 μm and *a-Si* 0.1 μm layers are used for the supporting and bolometric layers respectively

Comparatively, the 0.72 μm air gap is used for tuning the dielectric loading effect for the Salisbury screen. The air gap change causes the impedance change of the

structure; therefore, the value of the resistive sheet should be adjusted for the desirable peak absorption. In the frequency selective surface model, the equivalent model with capacitance and inductance can be used as a simplified form to tune the spectral response [15]. In the PRS, the surface is not comprised of an ideal metal; therefore, finite resistance can be applied instead of conducting wire, which represents a metal that is the ideal conductor [32]. Based on this general idea, it follows that resistive sheets should be less than the values of the Salisbury screen because the resistance of a narrower area increases the resistivity. Therefore, for maintaining same sheet resistance (*Rs*), the sheet resistance (*Rs*) of the pattern should be smaller. This can be analytically modeled; however, in this study, simple observation of full-wave simulation results, instead of finding an equivalent model, was conducted, and optimal values of resistive sheets for the dipole PRS were obtained.

Figure 2.25 shows the dipole PRS structure with a 2.5 μm air gap. *Rs* with the following values were changed: *Rs* 1, 1.5, 10, 50, 100 Ω. For higher *Rs* values such as 50 and 100 Ω, the PRS works more like a resistive sheet with broader-band absorption. The optimal value at 10 μm peak absorption is *Rs* 1 or 1.5 Ω. In addition, this selection has a narrower bandwidth compared to the freestanding PRS.

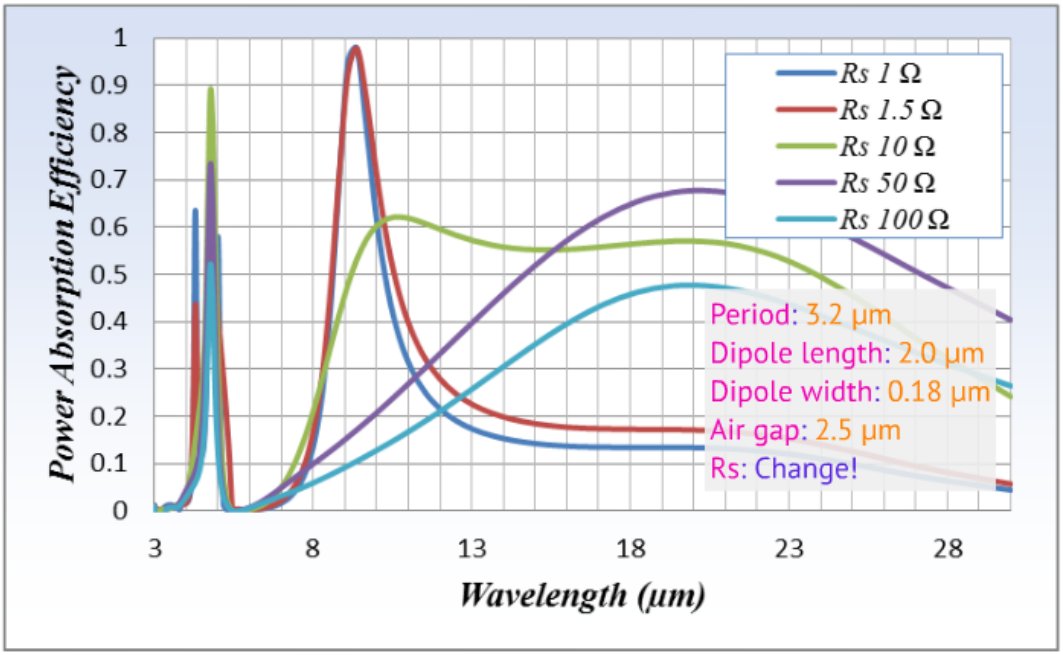

Figure 2.25 Dipole PRS changing resistive sheets: *Rs* 1.5 Ω optimal.

Next, a 0.72 μm air gap was applied, recovering the peak absorption compensating for the dielectric loading effect in Salisbury screen. Figure 2.26 shows the power-absorption efficiency with a 0.72 μm air gap applying different sheet resistance. The optimal value of resistive sheet is still 10 Ω, which is the same value as the freestanding dipole PRS. However the 1.5 Ω sheet resistance shows two separate peaks with degraded power-absorption efficiency of around 0.7. The optimal case using 10 Ω has wider bandwidth in the LWIR compared to the case using a 1.5 Ω with a 2.5 μm air gap. This shows that the optimal sheet resistance can be different for the different air gaps. Moreover, the bandwidth in spectral selectivity can be also changed.

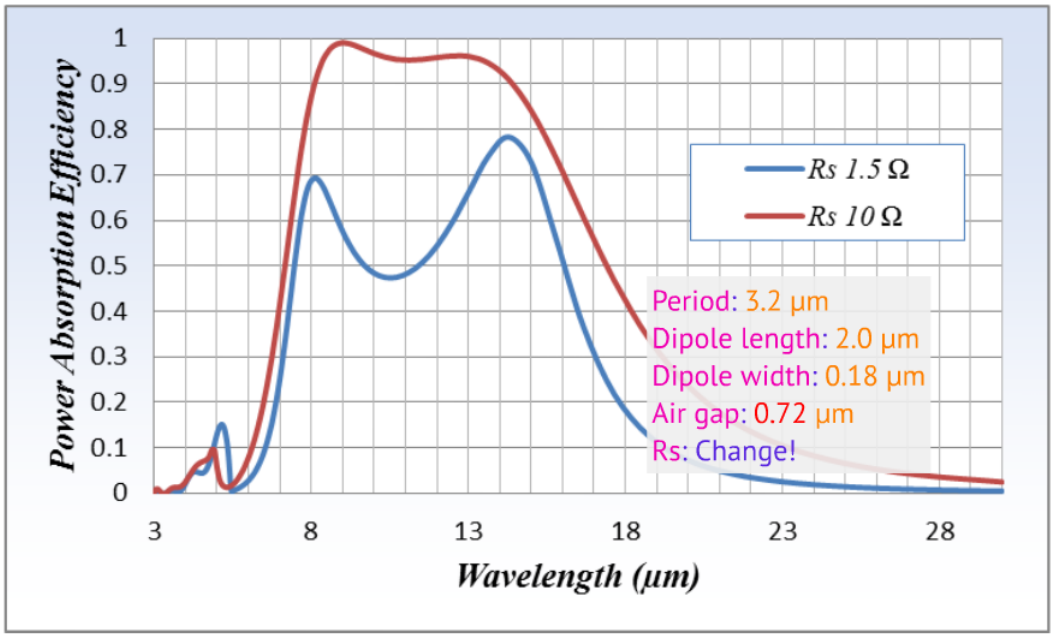

Figure 2.26 Air gap 0.72 μm with *Rs* 1.5, 10 Ω: 10 Ω for optimal peak absorption.

Figure 2.27 and 2.28 shows the case of different air gaps of 2.3 μm and 2.5 μm. Both cases show the peak absorption with the narrower bandwidth using *Rs* 1.5 Ω.

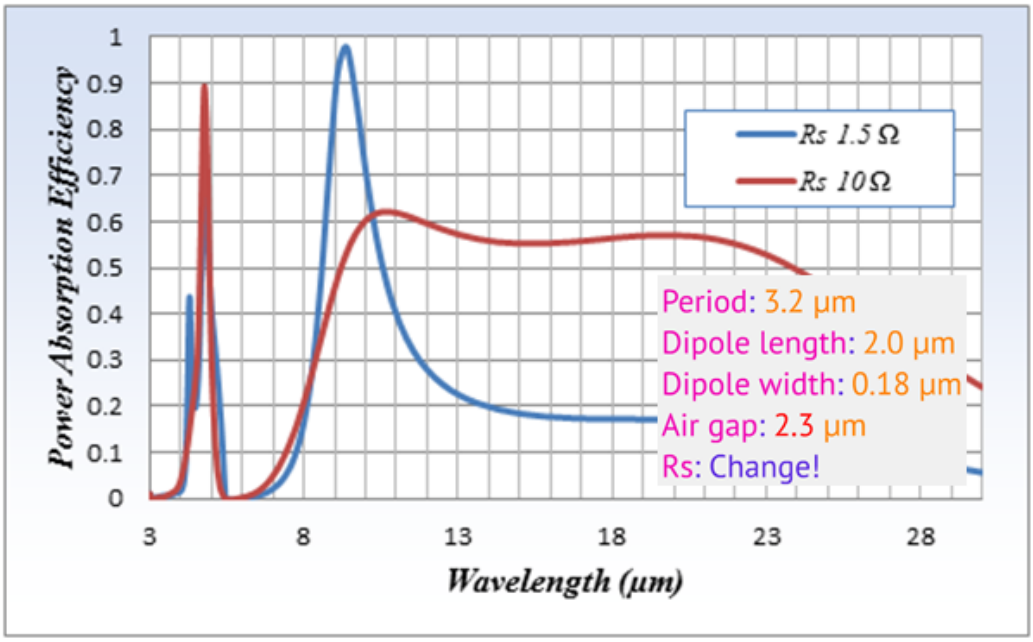

Figure 2.27 Air gap 2.5 μm with *Rs* 1.5, 10 Ω: 1.5 Ω for optimal peak absorption.

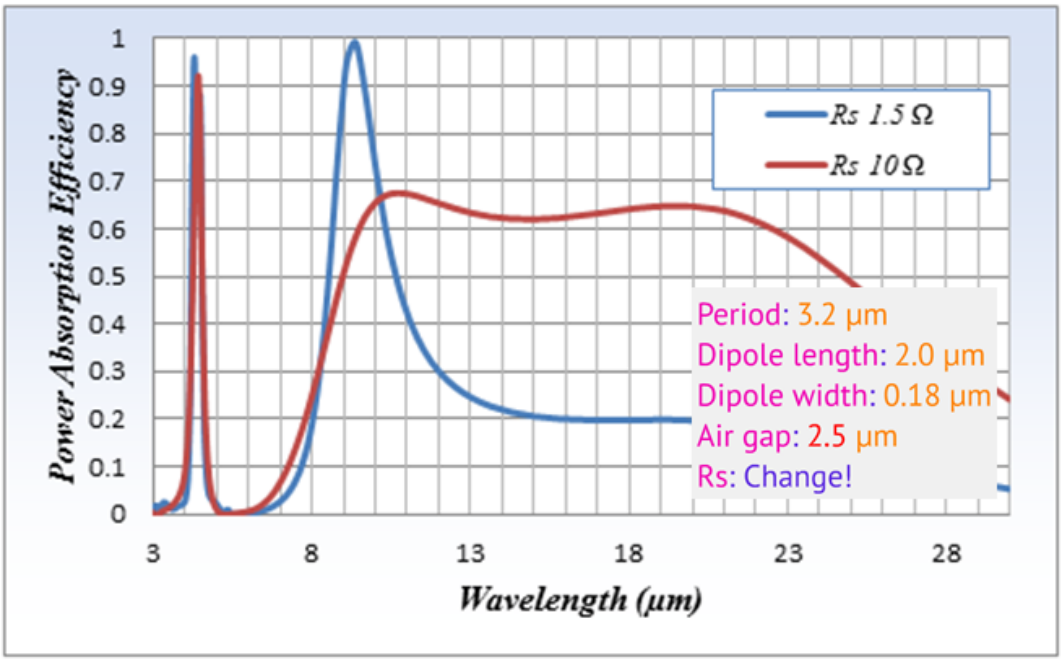

Figure 2.28 Air gap 2.3 μm with *Rs* 1.5, 10 Ω: 1.5 Ω for optimal peak absorption.

Dipole PRS with different air gap and corresponding resistive sheets can obtain 100 percent peak absorption at the 10 μm wavelength. This also can show that pattern size, air gap, and resistive sheet give us more possibility to tune the peak absorption.

2.2.5.2 Slot PRS shape study

Slot PRS is a complementary design of the dipole PRS. Although the slot PRS has an out-of-band reflection characteristic, it also offers resonance at the desired wavelength when fitting size, such as the length and width of the slot. The slot PRS spectral characteristics are compared both with and without undercut. Like the dipole PRS, I apply several different air gaps and different sheet resistance for tuning 10 μm peak absorption. Figure 2.29 shows the unit cell of slot PRS with different air gaps.

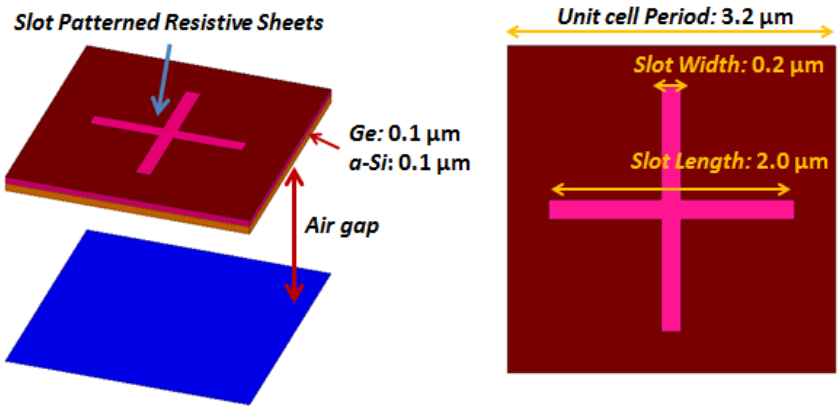

Figure 2.29 Unit cell of slot PRS with different air gaps.

The slot size is exactly the same as the dipole size in this case, with 2 μm length, 0.2 μm width, and 3.2 μm period. However, the optimal resistive sheet is not 10 Ω or 1.5 Ω. Figure 2.30 shows the peak absorption using 2.5 μm air gap with different sheet resistances. *Rs* 0.2 Ω has maximum peak absorption as a new optimal sheet resistance.

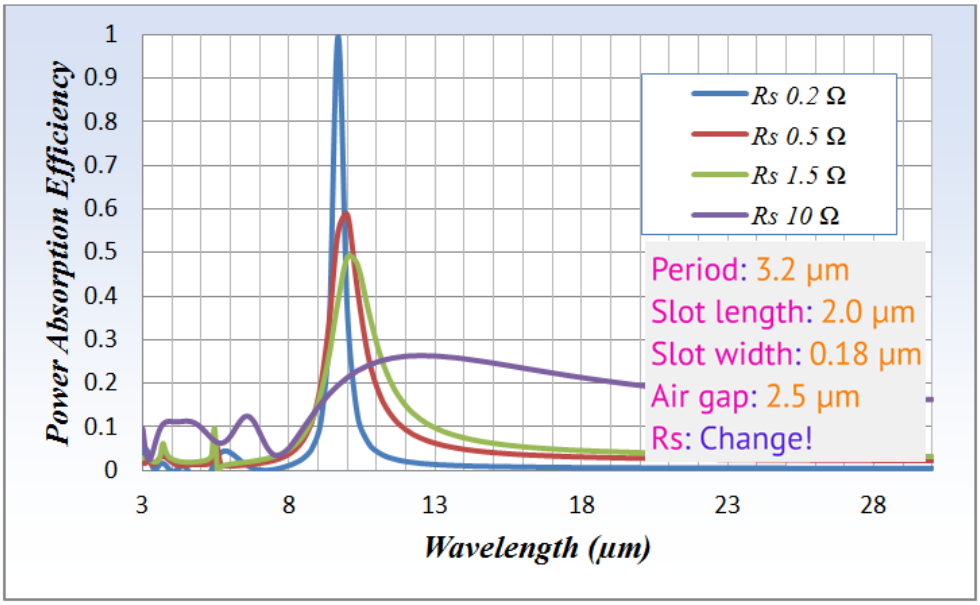

Figure 2.30 2.5 μm air gap: *Rs* 0.2, 0.5, 1, 1.5, 10 Ω; 0.2 Ω optimal.

Figure 2.31 shows the peak absorption using a 2.3 μm air gap with different sheet resistances. *Rs* 0.33 Ω exhibits maximum peak absorption.

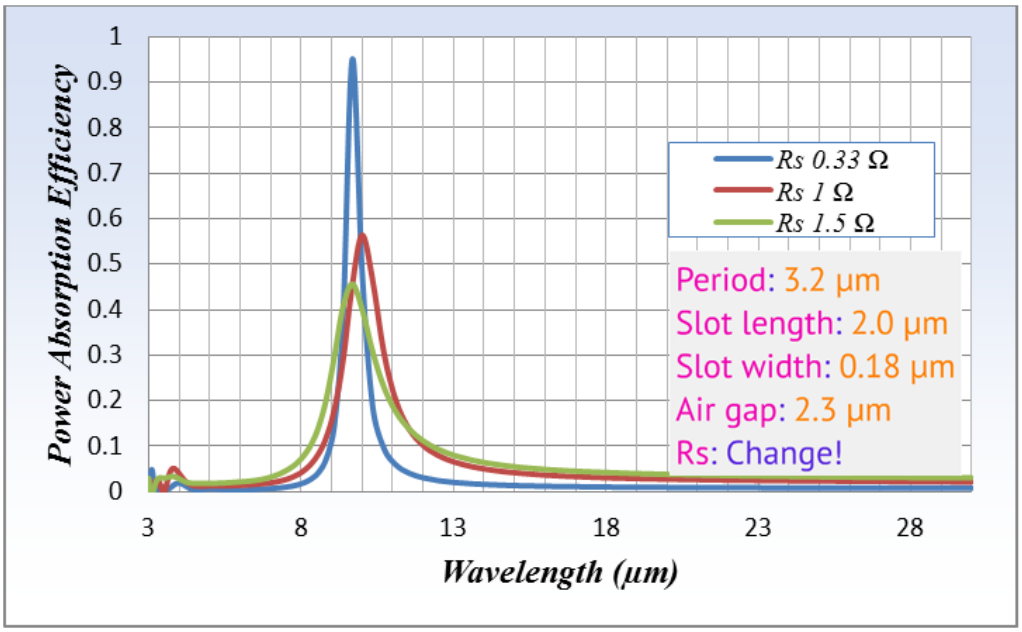

Figure 2.31 2.3 μm air gap: *Rs* 0.33, 1, 1.5 Ω; 0.33 Ω optimal, similar with 2.5 μm air case.

Figure 2.32 shows the air gap with 0.72 μm with *Rs* 0.2 Ω for maximum peak at 10 μm wavelength.

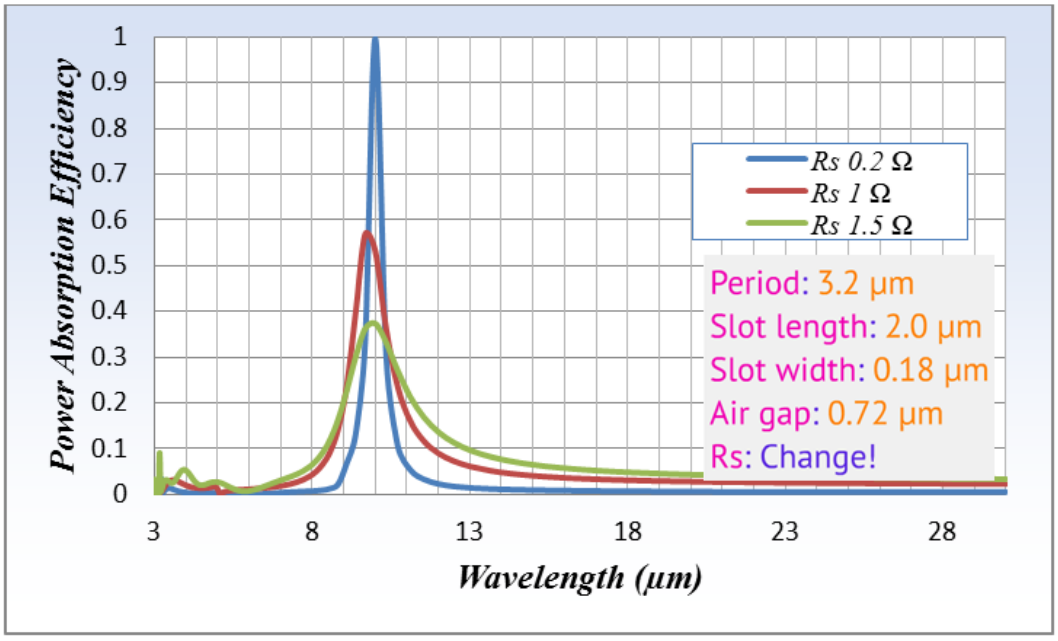

Figure 2.32 0.72 μm air gap: *Rs* 0.33, 0.5, 1.5 Ω; 0.33 Ω optimal.

The slot PRS has a narrower bandwidth compared to the dipole PRS in general; moreover, this narrowband absorption is better for spectral selectivity. However, the low sheet resistance values of 0.2 Ω and 0.3 Ω are very difficult to achieve when we consider real metal fabrication as the lower resistive sheets require a thicker metal layer. Therefore, skin depth and fabrication issues are important factors to consider in cases that have less than *Rs* 1 Ω.

2.2.5.3 Slot PRS with Undercut

In the case of the slot PRS, the undercut is applied (see Figure 2.33). This undercut provided mainly two advantages: First, with the mask used in the fabrication process, we added a hole and reduce the thermal mass of our pixel. Second, we reduced the dielectric loading effect compared to the slot without undercut.

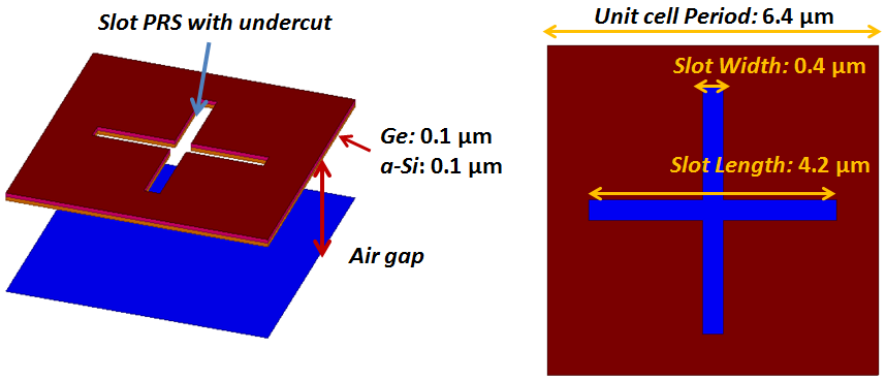

Figure 2.33 Slot PRS with undercut.

Figure 2.34 shows tuning for the maximum absorption at 10 µm wavelength. Instead of using the length of 2 µm and the width of 0.2 µm, which is the reduced size for compensating dielectric loading effect, the slot PRS with undercut did not shift the peak absorption strongly; therefore, the same pattern size is used in the case of the freestanding structure. In this specific case, the following sizes were used: 4.2 µm length, 0.4 µm width, 6.4 µm period, and different *Rs* values. *Rs* 1.5 Ω is the optimal value. Moreover, this value is considerable when the finite thickness of the real metal is used.

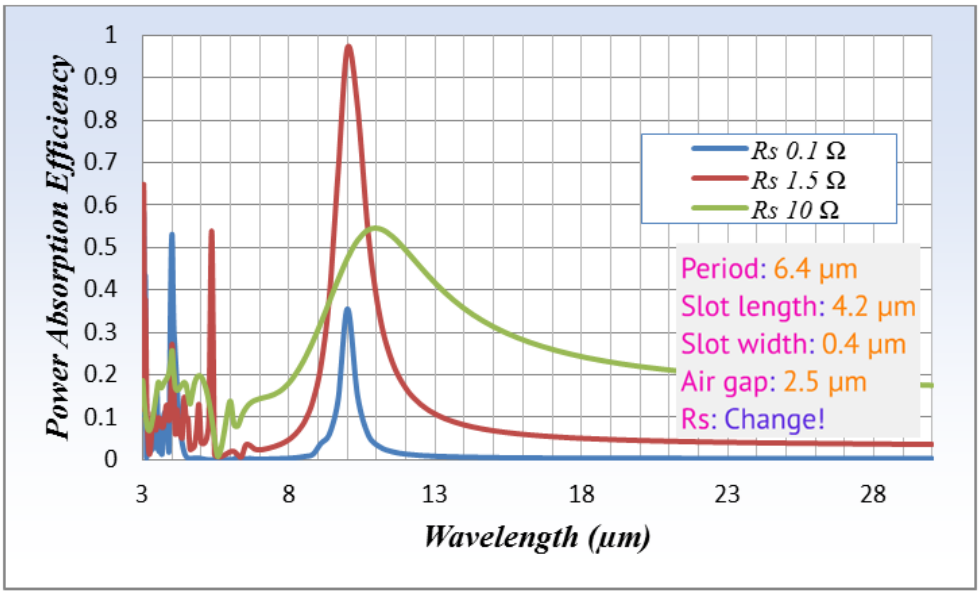

Figure 2.34 Air gap 2.5 μm with 4.2 μm length, 0.4 μm width, 6.4 μm period: *Rs* 0.1, 1.5, 10 Ω; 1.5 Ω optimal.

Figure 2.35 shows the case of a 2.3 μm air gap with different sheet resistance. The optimal sheet resistance is around 1.5 Ω. Figure 2.36 shows the case of a 0.72 μm air gap with different sheet resistance. The optimal sheet resistance is also 1.5 Ω. The results of the different air gaps show that the slot PRS with undercut is affected weakly by the change of the air gap. Therefore, the optimal sheet resistance is similar—around 1.5 Ω for the peak absorption.

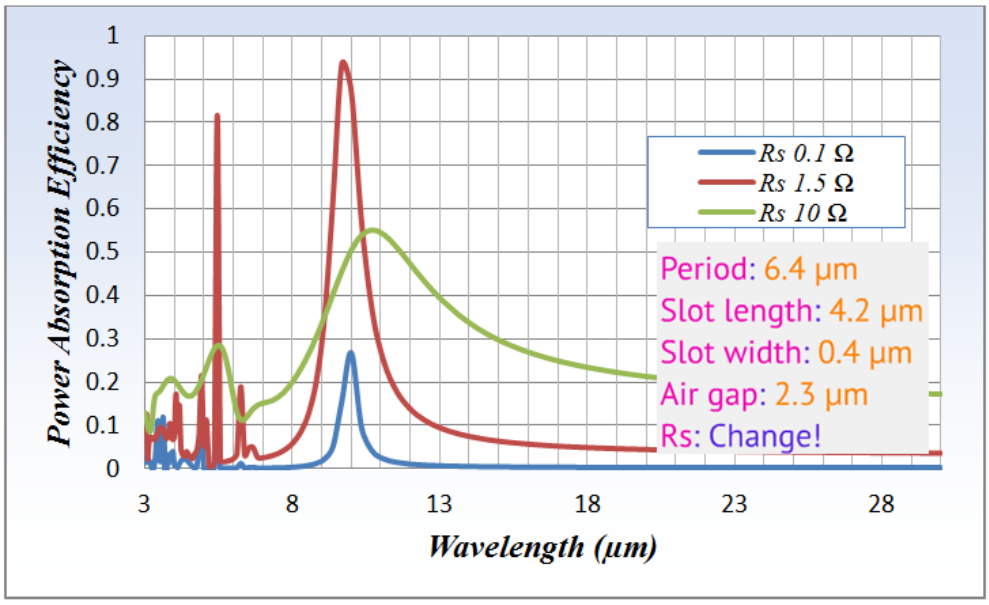

Figure 2.35 2.3 μm air gap: *Rs* 0.1, 1.5, 10 Ω: 1.5 Ω optimal.

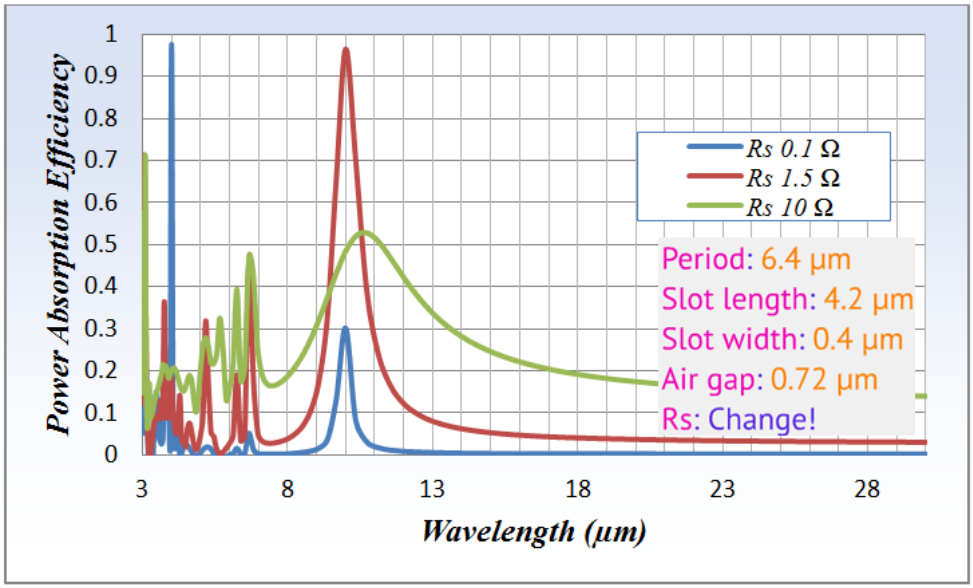

Figure 2.36 air gap 0.72 μm with 4.2 μm length, 0.4 μm width, 6.4 μm period: *Rs* 0.1, 1.5, 10 Ω; 1.5 Ω optimal.

Based on the study of the dipole PRS, slot PRS, and slot PRS with undercut, peak absorption can be tuned with the change of the dipole and slot PRS size and its sheet resistance. Both dipole and slot PRS patterns are influenced by adding dielectric layers; therefore, in order to compensate for the peak absorption, the size of each pattern should be reduced to the corresponding size which considers the refractive index of the dielectric layer. Moreover, sheet resistance smaller than 1 Ω can be selected. However, small sheet resistance can make the design process more difficult; AC conductivity and skin-depth effect should be considered as the thickness of metal layer is increased.

2.3 PRS and metal layer

In the PRS design, the DC sheet resistance can be estimated because of the general property of resistance. For the unit cell, *Rs* 377 Ω is used for the Salisbury screen for the impedance matching the air medium; however, when the patterned resistive sheet is used, the area of the resistive sheet is reduced. Therefore, *Rs* is higher than the one without pattern due to the dimension. In general, smaller *Rs* appear required as they correspond to area reduction due to the PRS. However, due to the PRS, the equivalent model is not just a resistive sheet: it includes capacitance and inductance for the pattern. This also changes the spectral response. The value of PRS can thus be estimated with the simple resistance property. As we shorten the width of the resistor or resistive bar, resistance increases proportionally to the inverse of width. For example, 1/3 of a width obtains three times the resistance. If the width is reduced to achieve the same resistance, we only need one inverse of the ratio which the width decreases. However, this is a rough estimation. For accurate values, we need to use a more complicated model or an explicit search to find the corresponding resistive sheet values. Therefore, for the pattern, we should have a

much less resistive sheet value compared to the value for the whole sheet. This resistive sheet can be considered a real metal with a finite thickness. Conductivity and resistive sheet has the following relation:

$$\sigma = R_s \times t$$

Therefore, as we increase *Rs*, we have a thinner thickness of the metal as we assume that the conductivity does not change much with respect to the frequency and the DC conductivity. Moreover, sheet resistance less than 1 Ω is not feasible in the both design and fabrication because it requires a thick metal layer which makes the fabrication more difficult and the design more complex, considering the skin effect. If the *Rs* is too small, the metal layer gets thicker; therefore, we need to consider the skin depth and AC conductivity rather than the DC conductivity in both design and fabrication.

Table 2.3 shows the candidate metals and its conductivity and skin depth. In addition, the thickness of the corresponding resistive sheet is calculated for each metal.

	Cu	Al	Cr	Ti
Electrical Conductivity (Siemens. S)	5.800E+07	3.800E+07	7.600E+06	1.798E+06
Skin depth at 10 μm (nm)	1.207E+02	1.491E+02	3.335E+02	6.856E+02
Skin depth at 5 μm (nm)	8.536E+01	1.055E+02	2.358E+02	4.848E+02
Rs=10, thickness (nm)	1.724E+01	2.632E+01	1.316E+02	5.562E+02
Rs=1, thickness (nm)	1.724E+02	2.632E+02	1.316E+03	5.562E+03
Rs=0.5, thickness (nm)	3.448E+02	5.264E+02	2.632E+03	1.112E+04
Rs=0.1, thickness (nm)	1.724E+03	2.632E+03	1.316E+04	5.562E+04

Table 2.3 Candidate metal and its property [47].

For the smaller resistive sheets measuring less than 1 Ω, all the metal is thicker than skin depth. Therefore, we need to consider the skin-depth effect and AC conductivity for accuracy in design. In order to avoid the difficulty of using AC conductivity and fabrication issues in the design process, measurements of less than 1 Ω

resistance should not be thought to effect easier design process and fabrication. Henceforth, aluminum (*Al*) as a metal example will be used to verify the adequacy of using real metal instead of resistive sheets. This process also verifies that using resistive sheets can reduce the simulation time in the design process compared to using real metal. Figure 2.37 shows the dipole PRS freestanding case with different thicknesses using *Al*. Figure 2.38 shows the same freestanding case using infinitely thin resistive sheets. The 2.6 nm (26 Å) is corresponding thickness for *Rs* 10 Ω, and it exhibits good agreement when real metals are substituted for resistive sheets.

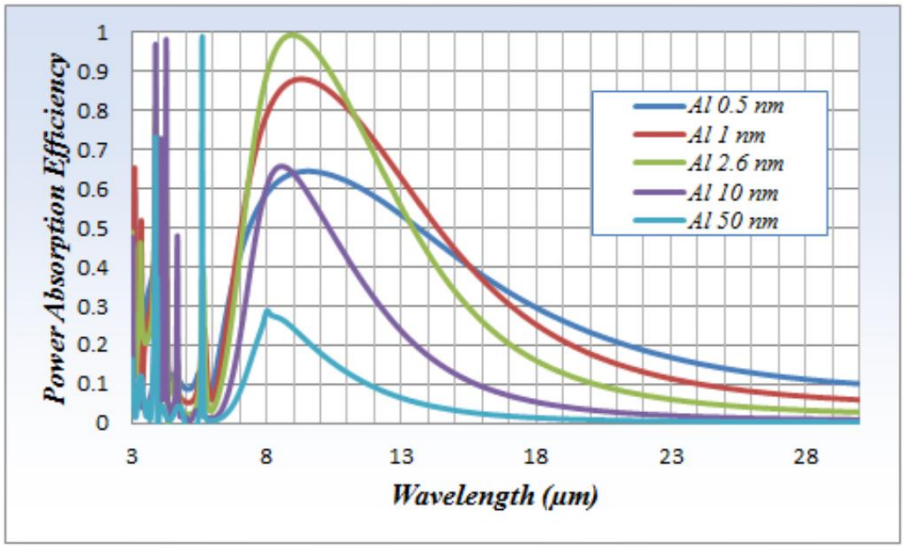

Figure 2.37 Freestanding with *Al* metal: 0.5, 1, 2.6, 10, 50 nm: 2.6 nm optimal (corresponding value to *Rs* 10 Ω).

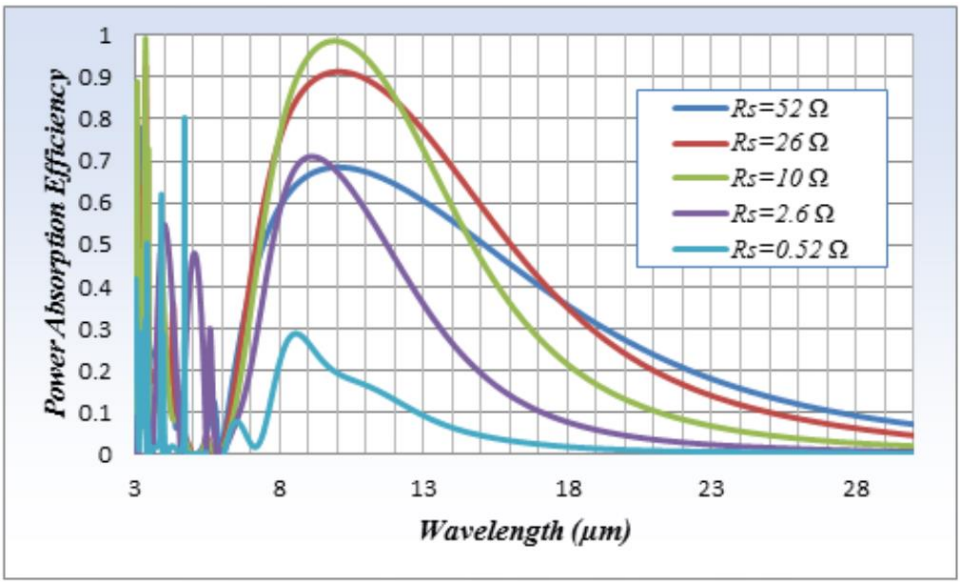

Figure 2.38 Freestanding with sheet resistance: 52, 26, 10, 2.6, 0.52 Ω: *Rs* 10 Ω optimal (corresponding value with *Al* metal 2.6 nm).

Figure 2.39 shows the *Al* metal with *a-Si* and *Ge* layers. The 2.6 nm *Al* is used with a 0.72 μm gap. Moreover, Figure 2.40 shows the 2.5 μm air gap case with a 17.5 nm *Al*, the thickness of which corresponds to the optimal thickness of *Rs* 1.5 Ω.

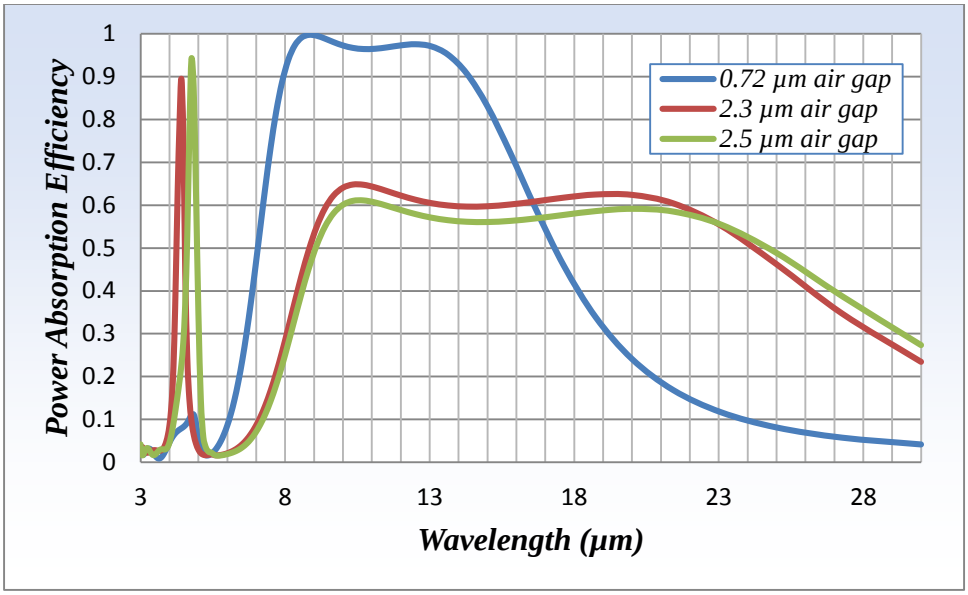

Figure 2.39 *Al* metal with *a-Si* and *Ge* layers using 2.6 nm (*Rs* 10 Ω).

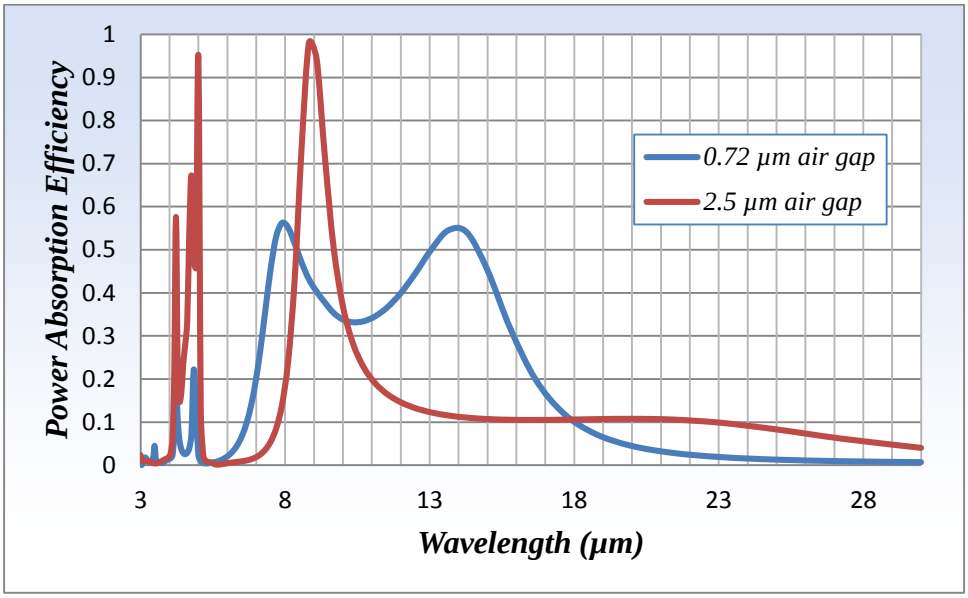

Figure 2.40 *Al* metal with *a-Si* and *Ge* layers using 17.5 nm (*Rs* 1.5 Ω).

As the advantages of using PRS has been shown, the thickness of 50 nm is fixed, and the pattern is changed to 2.2 µm and 0.6 µm length and width respectively. Figure

2.41 shows the design using *Al* with a fixed 50 nm thickness. Figure 2.42 shows that we can achieve the peak absorption at 10 µm wavelength using fixed metal thickness.

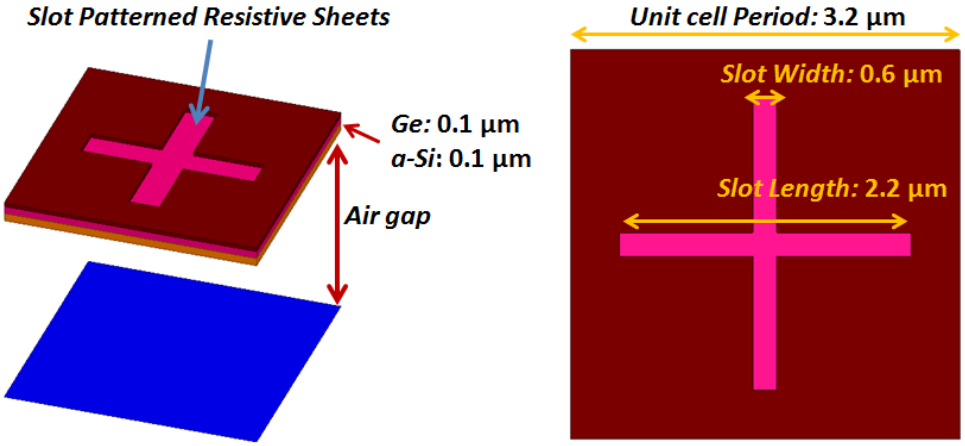

Figure 2.41 Slot PRS design using *Al* 50 nm fixed thickness.

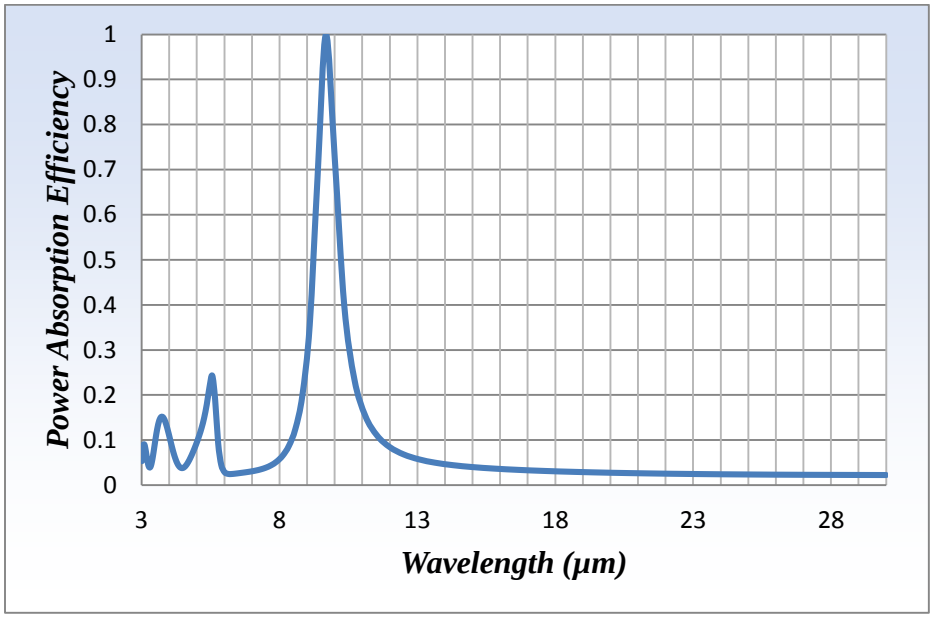

Figure 2.42 Metal *Al* 50 nm absorber tuned with PRS to achieve maximum absorption at 10 µm wavelength.

As we use PRS, we have pattern size and metal thickness (*Rs*) to optimize the absorption including air gap adjustments.

2.4 PEC verification

In the real microbolometer pixel design, the bottom layer comprises SiO_2 with a mirror. Our group used SiO_2 for the substrate, aluminum for the mirror. Compared below are PEC and real substrate with mirror in HFSS™ simulation. Figure 2.43 shows the ideal PEC and real substrate layer with mirror.

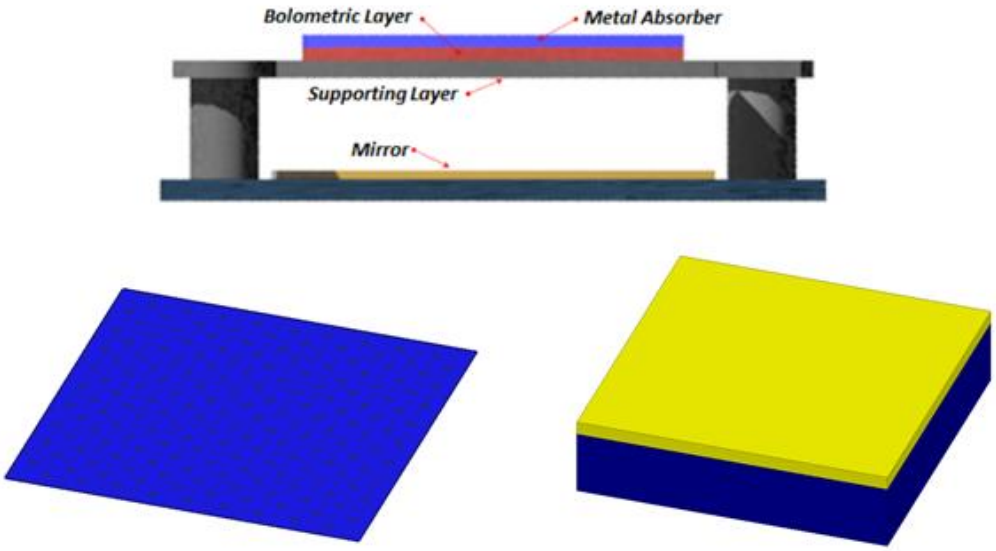

Figure 2.43 Ideal PEC and real substrate layer with mirror.

Figure 2.44 shows a good agreement between the ideal PEC and real substrate with mirror

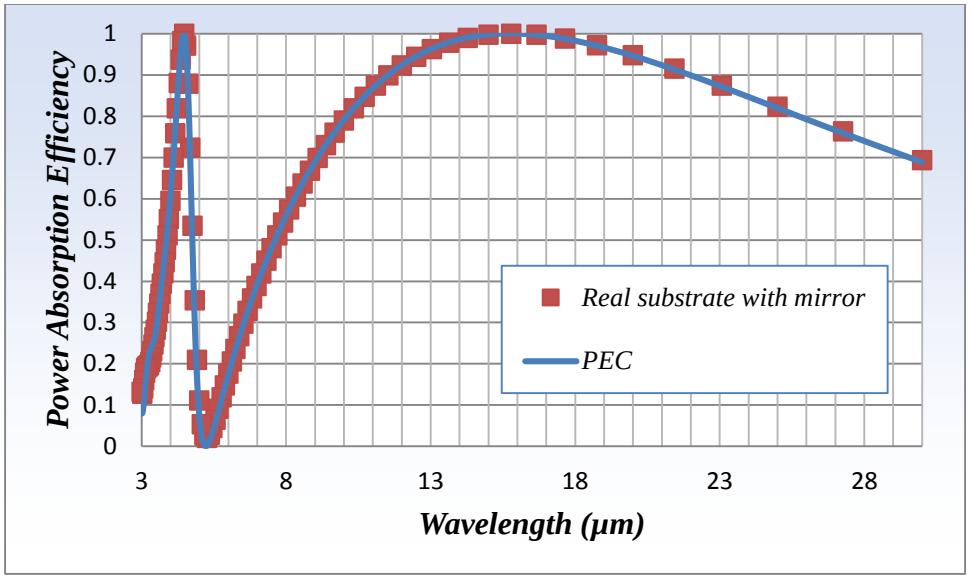

Figure 2.44 Salisbury screen between ideal PEC and real substrate with mirror.

Therefore, we can use the ideal PEC for our unit cell simulation without losing the significant accuracy. In this chapter, key features for the pixel design are verified, along with a process to reasonably apply realistic values for simulation.

Chapter 3 Reduced thermal design with spectral selectivity in microbolometer

Thermal detectors, such as microbolometers, have slower response because the thermal mass of the absorbing structure induces slow temperature change [8, 17, 18]. As such, the best way to increase the speed of response is to reduce the thermal mass [39]. The thickness of the dielectric support layer is the only factor that can change the thermal mass in the conventional microbolometer structure. However, reducing the thickness of the dielectric layer is limited by the minimum amount of mechanical strength needed to sustain the structure. Some researchers, including members of our group, added perforations in the supporting layers to obtain broadband absorption with a reduced thermal mass. The results show fairly good broadband absorptions in the LWIR band [39, 40]. These studies focused on broadband absorption and did not consider narrowband absorption. The test could not apply perforations directly in the multispectral microbolometer application because these perforations would have likely changed spectral selectivity and degraded the narrowband absorption in certain bands.

This chapter introduces a new microbolometer pixel design which reduces the thermal mass without changing spectral selectivity for broadband and narrowband absorption in PRS microbolometer. This design adds square perforations for both designs using dipole and slot-patterned resistive sheets. The proposed design has PRS on the perforated germanium support layer and the amorphous silicon bolometric layer. These layers are thermally isolated from the bottom mirror layer, using the air gap. The concept also shows how to tune the peak absorption by changing the air gap. It compares the absorption rate of the layer with perforations to that without and studies the optimal

perforation size with optimized dipole and slot-patterned resistive sheets for 10 μm peak absorption. In optimal cases, the perforations considerably reduce the thermal mass. The design also presents interference between patterned resistive sheets and perforation size, which causes significant changes to the peak absorption rate when the perforation area is increased beyond the optimal size.

3.1 Design parameters about the reduced thermal mass

We consider the design parameters of the microbolometer that include the resistive absorber, air gap, and thermal mass. The microbolometer requires higher sensitivity and faster response in its performance. Equation 3.1 and equation 3.2 are the governing equations for the thermal mass in the microbolometer:

$$R_v = \alpha \cdot R_0 \cdot I_{bias} \cdot \frac{\Delta T}{\Delta P_{abs}}$$

$$= \alpha \cdot R_0 \cdot I_{bias} \cdot \eta_{abs} \cdot \frac{1}{G_{th}\sqrt{1+\omega^2\tau^2}} \qquad (3.1)$$

$$\tau = \frac{C_{th}}{G_{th}} \qquad (3.2)$$

To achieve higher sensitivity, thermal conductance, *Gth*, must be decreased or the thermal resistance, *Rth*, increased. On the other hand, for the faster response, thermal conductance must be increased or the thermal resistance decreased. Moreover, it is possible to achieve faster response by reducing the thermal capacitance, *Cth*. In the given equations, larger thermal conductance (or thermal resistance) degrades the sensitivity but provides faster response time. Using thermal conductance as a design parameter cannot

achieve both higher sensitivity and faster response. Therefore, we focus on reducing the thermal capacitance of the microbolometer for faster response. Equation 3.1 shows that responsivity is inversely proportional to the heat capacity of the microbolometer; moreover, heat capacity is proportional to the mass of the structure. Therefore, adding square holes can remove the mass in the layers and, consequently, reduce thermal mass and obtain faster response. Applying hole does not change and degrade the fill factor of the Focal Plane Array (FPA). Figure 3.1 shows the fill factor of an FPA and the fill factor applying holes of an FPA. As the holes are added, the sensitive area of the IR absorber layer decreases; however, the fill factor does not change. It has the same effective area in the IR absorption.

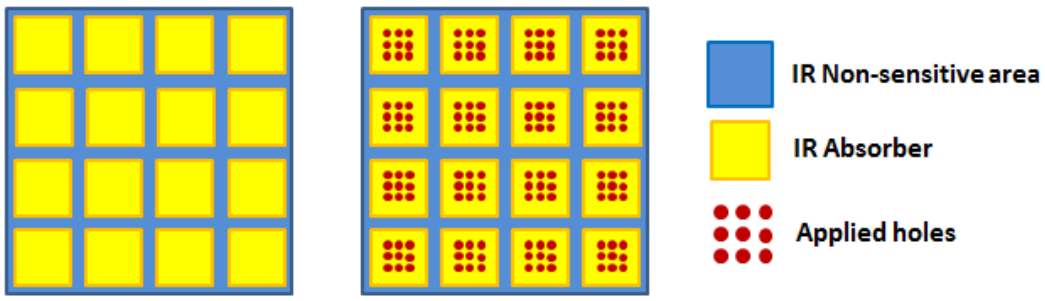

Figure 3.1 Fill factor between the cases of non-applying and applying holes in FPA.

In other previous research, it was shown that adding square holes provides broadband absorption in the same way as not adding square holes [39]. The current research (as shown in this dissertation) shows that adding square holes to the structure with the PRS in the dielectric layers provides narrowband absorption and maintains spectral selectivity [15, 48]. Both dipole and slot-type PRS with square holes were designed. Figure 3.2 shows the dipole PRS (a) and slot PRS (b) structures.

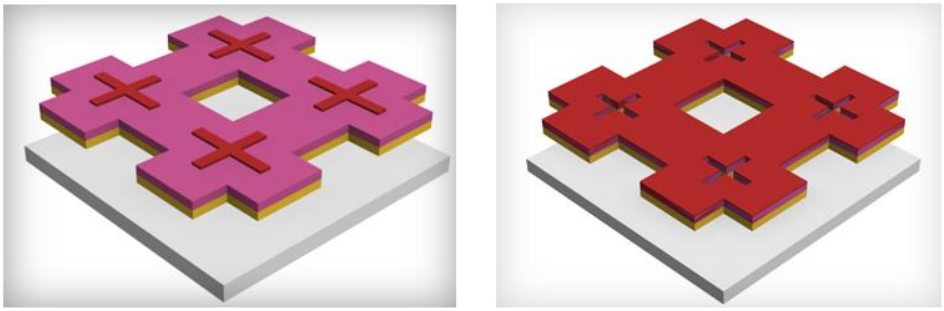

(a) (b)

Figure 3.2 Dipole PRS and slot PRS structure.

3.2 Reduced thermal mass pixel design

The reduced thermal mass design follows three individual processes: The first step is to find the initial pattern for the narrowband absorption using the dipole and the slot PRS respectively. The second step is to apply square holes in the dielectric layers and observe their effect on spectral selectivity. The last step is to tune the parameters of the patterns and holes to achieve the reduced thermal mass without significant changing spectral selectivity. Figure 3.2 shows two individual processes to apply the holes in the dipole PRS design for the thermal mass reduction. In the case of the dipole PRS, the metal absorber layer is separate with the dielectric layers. Therefore, adding holes in the dielectric does not change the metal absorber layer. Not like metal absorber, the other layers are lossless dielectric layers which do not absorb the infrared energy. Therefore, if there is no patterned resistive sheet, there is no absorption in the structure according to the refractive index of *Ge* and *a-Si* which are lossless in the LWIR region. Therefore, the main design factor in the dipole PRS using holes is the interference between PRS and holes.

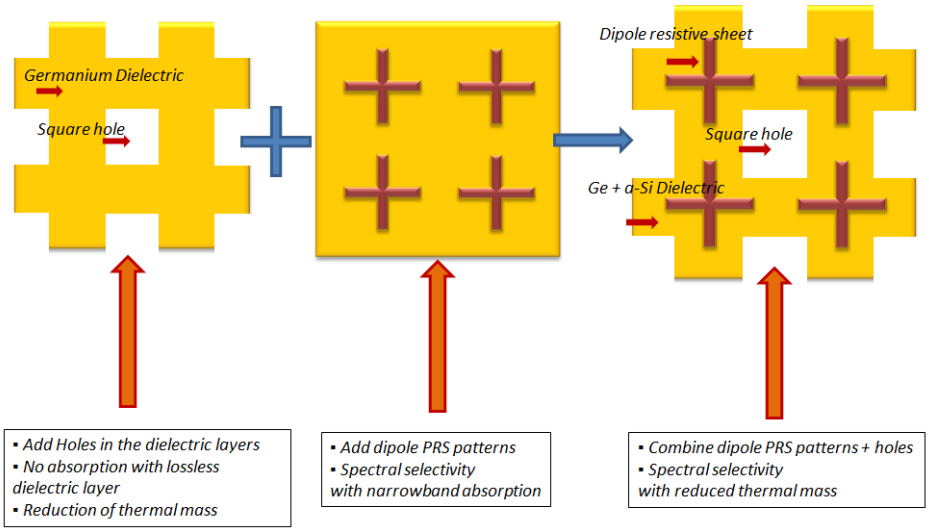

Figure 3.2 Design process of the broadband reduced thermal using perforation and the narrowband using dipole patterned resistive sheet.

On the other hand, the slot PRS case is different with the case of the dipole PRS. The metal absorber is also removed as we add the holes; therefore, the current distribution related with the power absorption can be influenced in the corresponding wavelength absorption by holes. Square holes can work as another slot PRS separately with the cross-slot PRS. Therefore, the square-hole size and the interference between hole and cross pattern can be more considerable. Figure 3.3 shows the design process of the slot PRS with holes for the reduced thermal mass.

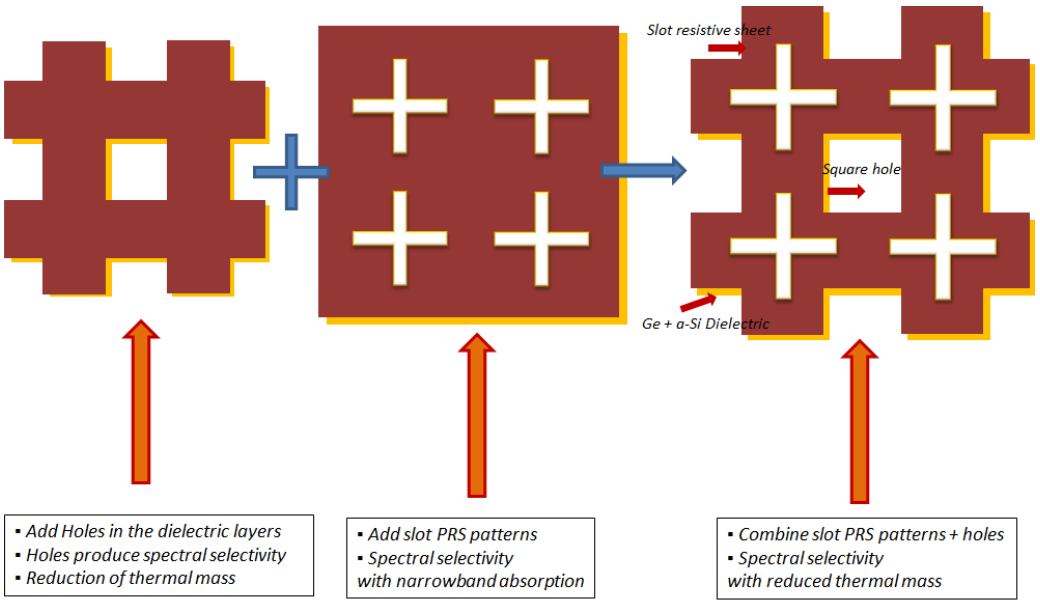

Figure 3.3 Design process of the broadband reduced thermal using perforation and the narrowband using slot PRS.

3.2.1 Dipole PRS thermal mass reduced design

First, the dipole PRS is considered for the reduced thermal design. Figure 3.4 shows the schematic of the pixel design of the dipole PRS structure. The unit cell size for the simulation is 3.2 μm by 3.2 μm. The unit cell has *Ge* and *a-Si* dielectric layers whose thicknesses are 0.1 μm respectively. *Al* metal of the thickness with 17.5 Å, which is comparable with *Rs* 1.5 Ω, is used for the metal absorber, and 0.72 μm is used for air gap. The width of a cross pattern is 0.2 μm, and the length of a cross pattern is 2.0 μm which are designed for the narrowband absorption at the 10 μm wavelength. The pattern size is considerably selected as the half contour of the cross pattern, and the contour is almost half-wavelength of the 10 μm. Moreover, *Ge* and *a-Si* dielectric effect is considered so that we apply smaller contour size of cross pattern, 2.2 μm, than the case without dielectric whose cross length is around 5 μm. The holes are added, and the maximum size

of each hole is limited to the size which has the support for the patterns after removing dielectric layers.

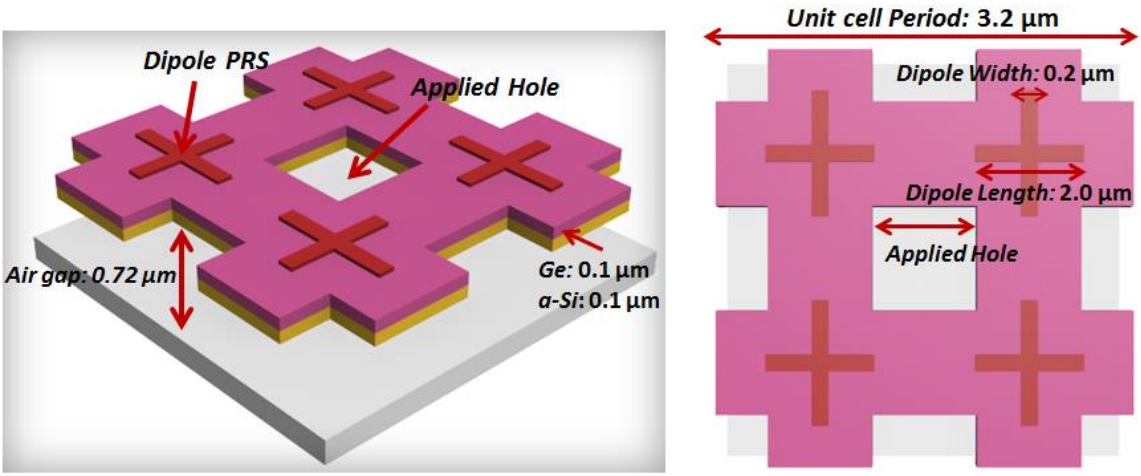

Figure 3.4 Suggested dipole-patterned microbolometer design for reduced thermal mass.

Figure 3.5 shows spectral selectivity with varying hole sizes. As the hole size is increased, the peak shifts to the lower wavelength. From no hole to a hole exhibiting the maximum size of 1.4 µm by 1.4 µm, the peak absorption is reduced, and the peak wavelength decreases from 10 µm to 7 µm. This can be explained by the fact that the dielectric loading effect is reduced with the larger hole size. Therefore, the greater degree of removal of the dielectric layer around the patterns affects the similar condition of having less dielectric layer around or under the PRS.

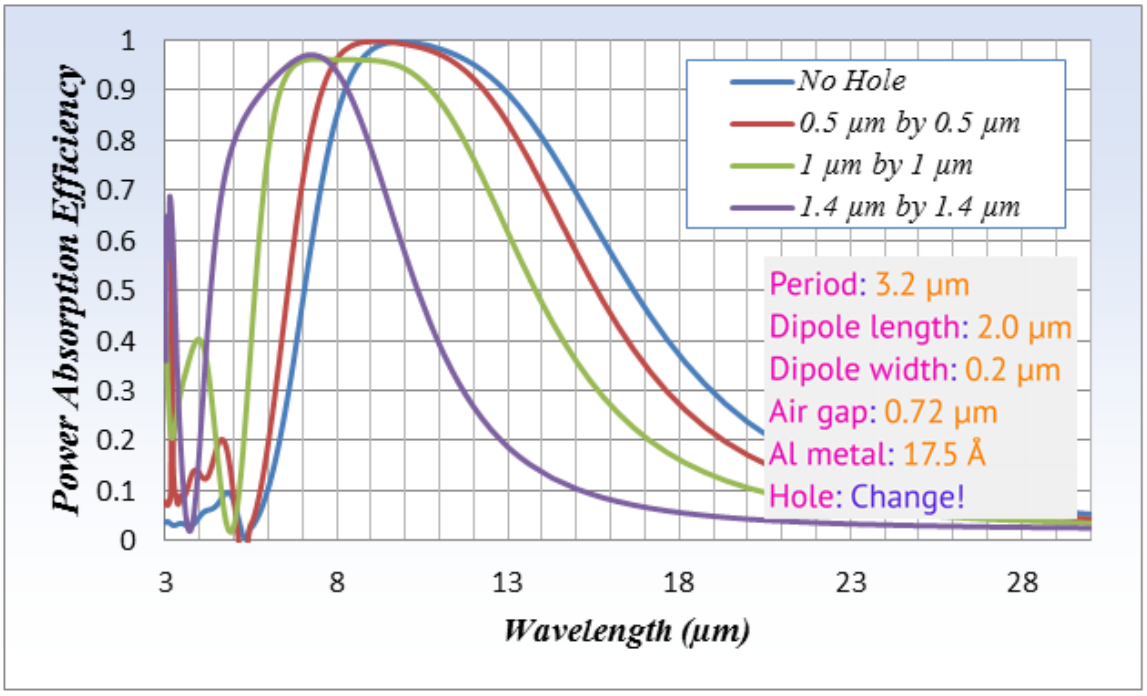

Figure 3.5 Dipole PRS with different hole sizes.

This peak shifts can be adjusted with the change of the pattern size and other parameter adjustments. Before compensating for the peak wavelength, the design is considered using different periods, which have more potential to increase hole size. Figure 3.6 introduces the different dipole size with the larger difference in period. This design has the same 10 μm peak absorption without holes. However, this design has more area due to the larger period for the unit cell. The length of the pattern is 1.7 μm, and the width of the pattern is 0.4 μm. The period is now 6.4 μm, which is twice the length the previous design, and the air gap 0.72 μm. The *Al* metal is used as a metal absorber with the thickness of 17.5 Å, which corresponds to *Rs* with 5 Ω.

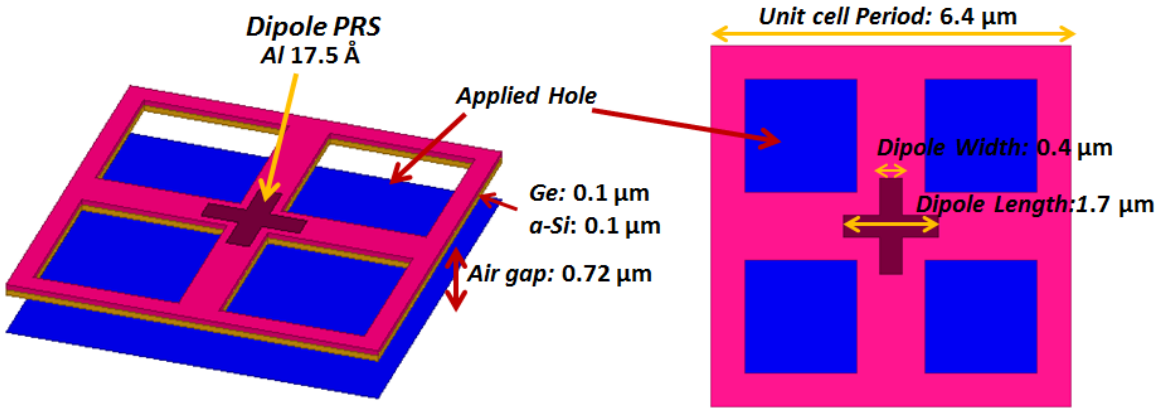

Figure 3.6 New selection for adding more holes.

Figure 3.7 shows spectral selectivity of the dipole PRS design with the larger period for the unit cell. As the individual hole size is increased from 0.0 µm (no hole) to 2.5 µm, the peak absorption shifts to the lower wavelength region. The shift to the lower wavelength is not unlike the previous case involving the smaller dielectric loading effect.

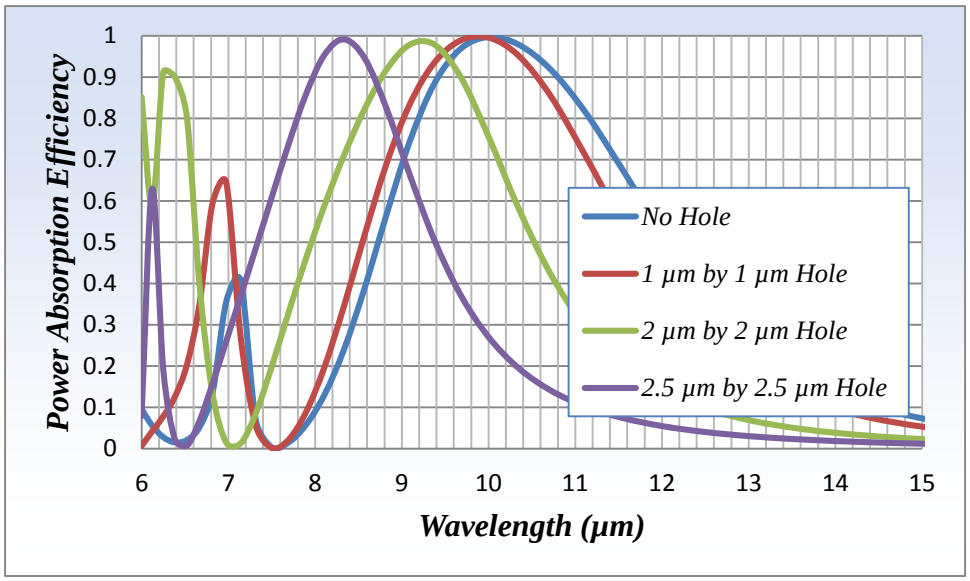

Figure 3.7 Spectral selectivity for new design: No hole, 1, 2, 2.5 µm hole from right to left.

To tune the 10 μm peak absorption, the length of the dipole PRS is increased based on the design rule that the longer, or larger, pattern size produces the longer wavelength peak absorption. Figure 3.8 shows the increase of the wavelength of the peak absorption. The length of the dipole is 2.4 μm for the 10 μm peak absorption. With this hole size, the fill factor of the unit cell is reduced by 61 percent, having the same 10 μm peak absorption, thereby maintaining spectral selectivity.

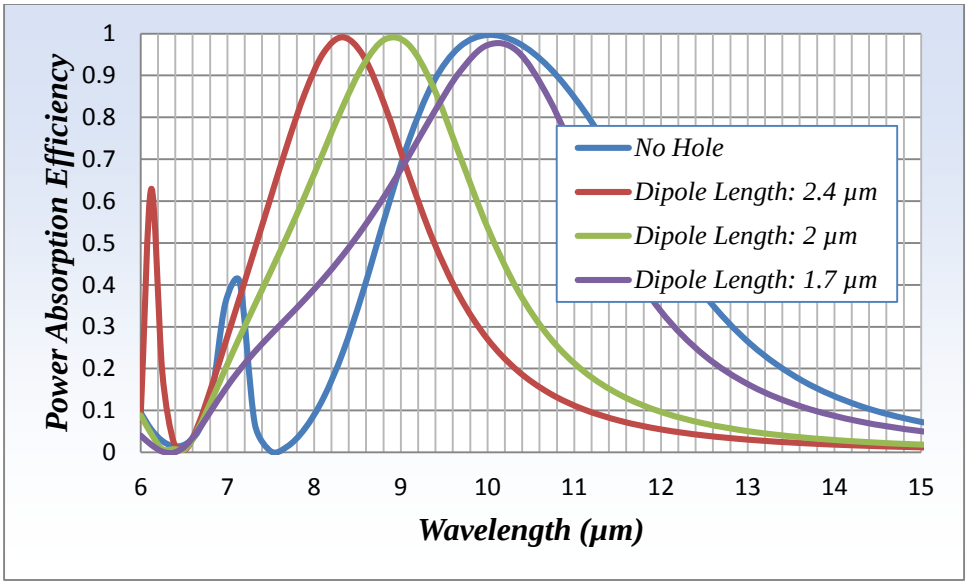

Figure 3.8 Dipole PRS length adjustment for 10 μm peak absorption: dipole length 1.7, 2.2, 2.4 μm change.

The previous test examined the effect of increasing hole size and also found that spectral selectivity is less influenced by the smaller holes. Therefore, if many small holes can be applied with minimal change to spectral selectivity, the reduced thermal mass design has more advantages in placing holes. Figure 3.9 shows the same dipole PRS design with many holes. With the dipole PRS of 2.3 μm length and 0.5 μm width, the study applied different sizes of small holes.

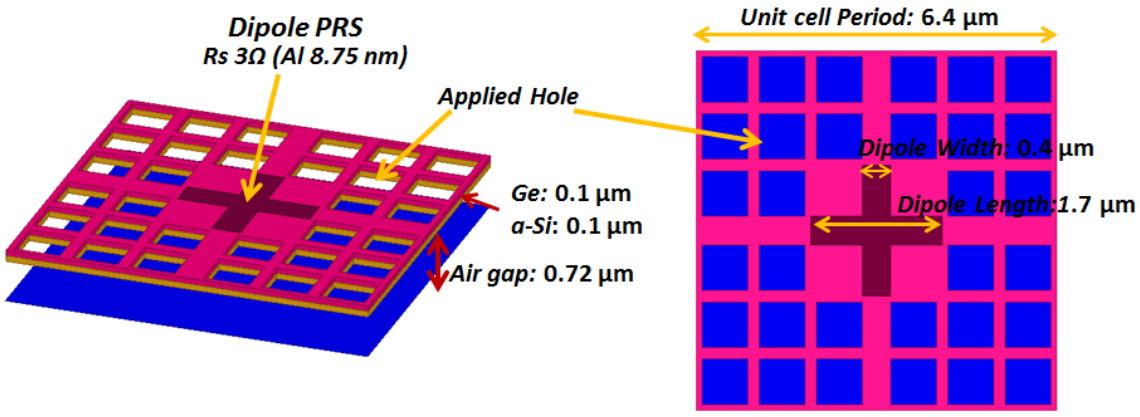

Figure 3.9 Thermal reduced mass design with small holes.

Figure 3.10 shows spectral selectivity for the 10 µm peak absorption of holes measuring 0.9 µm by 0.9 µm. These small holes reduce the thermal mass by 63 percent.

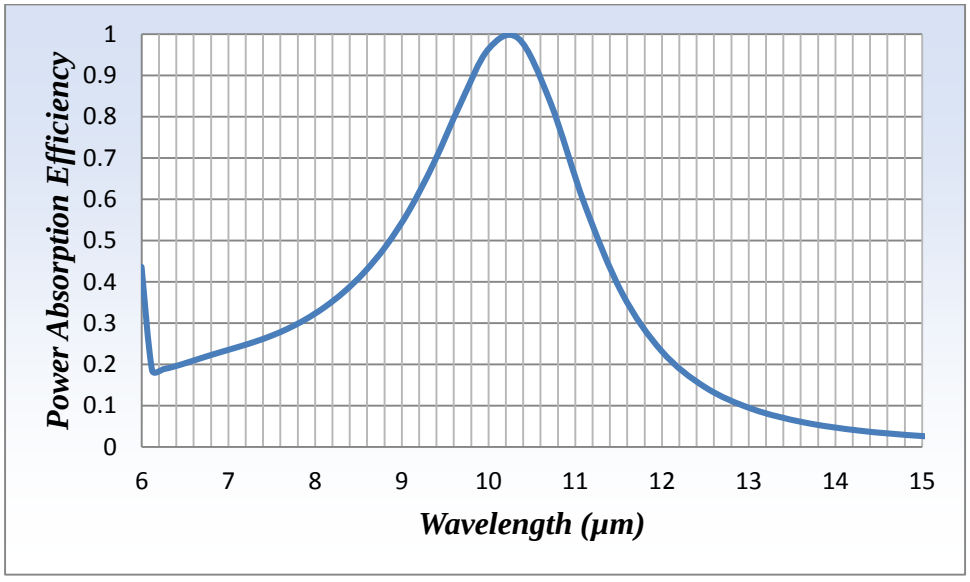

Figure 3.10 Spectral selectivity of the design with small holes.

3.2.2 Design of the square holes with dipole and slot-type PRS

In a complementary approach, the reduced thermal design for the slot PRS is introduced. Figure 3.11 shows the dipole PRS (a) and slot PRS (b) with square holes. The slot PRS case is different from that of the dipole PRS because the metal absorber layer includes both the dipole and hole patterns, whereas the dipole PRS is separated from holes in the dielectric layer. Therefore, applying holes in the slot PRS causes more shifting and change in its spectral selectivity.

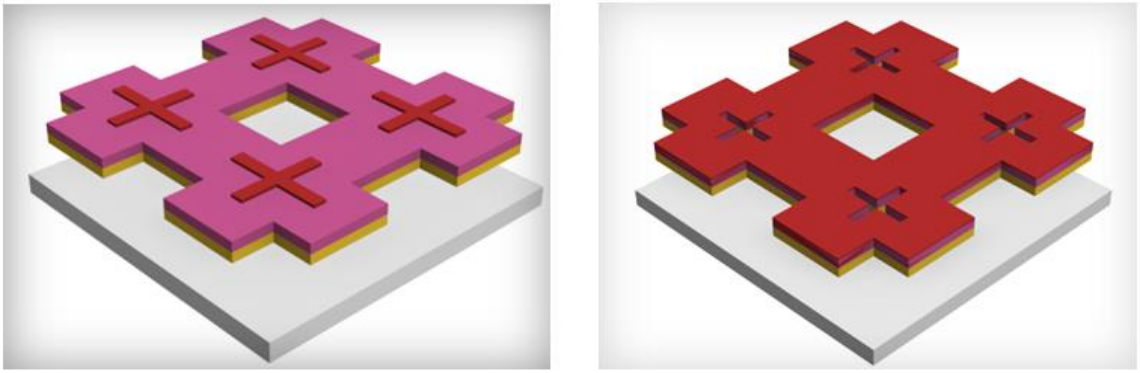

(a) (b)

Figure 3.11 Dipole and slot PRS complementary design.

First, after applying only holes in the design, spectral selectivity of the holes is monitored. Figure 3.12 shows two different ways to apply holes with a 6.4 μm period. The holes in Figure 3.12 (a) are applied within the area of the period. The holes in the Figure 3.12 (b) are applied at each edge to consider the entire pixel. In the first case, involving two different *Rs* (*Rs*=1.5 Ω and 10 Ω), the hole size varies from 1 μm by 1 μm to 2.5 μm by 2.5 μm.

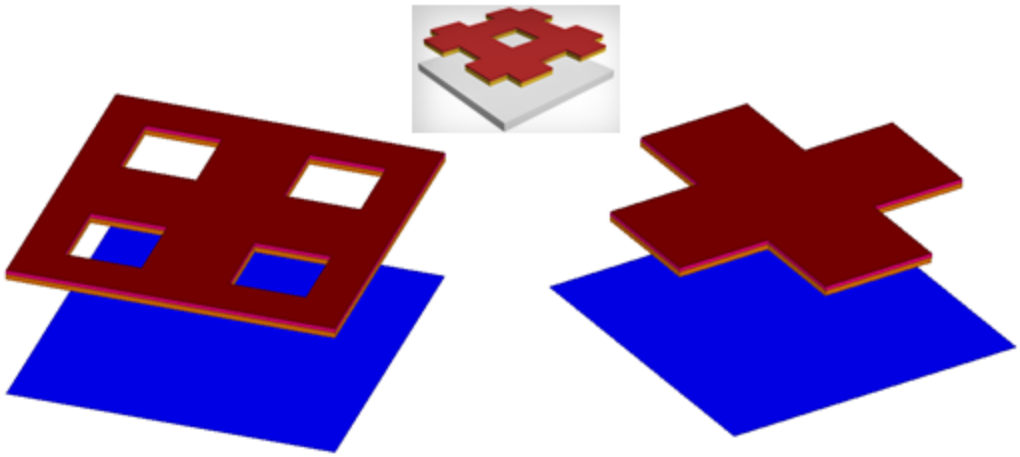

Figure 3.12 Applying only holes in the unit cell.

Figures 3.13 and 3.14 show spectral selectivity using *Rs* 1.5 Ω and 10 Ω respectively. Smaller holes measuring 1 μm by 1 μm do not absorb a significant amount of power; however, as the hole size increases to 2.5 μm, the peak absorption appears to be at 7 μm wavelength. This shows the hole has little absorption at 10 μm wavelength; therefore, 10 μm peak absorption remains, with little influence made by the holes. However, when we consider the general spectral selectivity of using both hole and slot PRS, the holes must be carefully selected to main peak absorption.

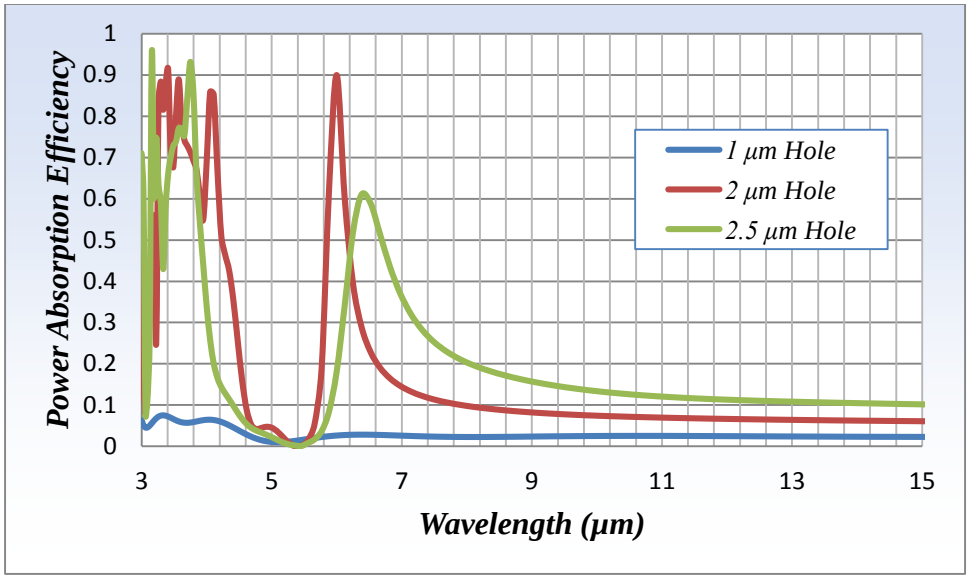

Figure 3.13 Hole size variation with 1.5 Ω: 1, 2, 2.5 μm.

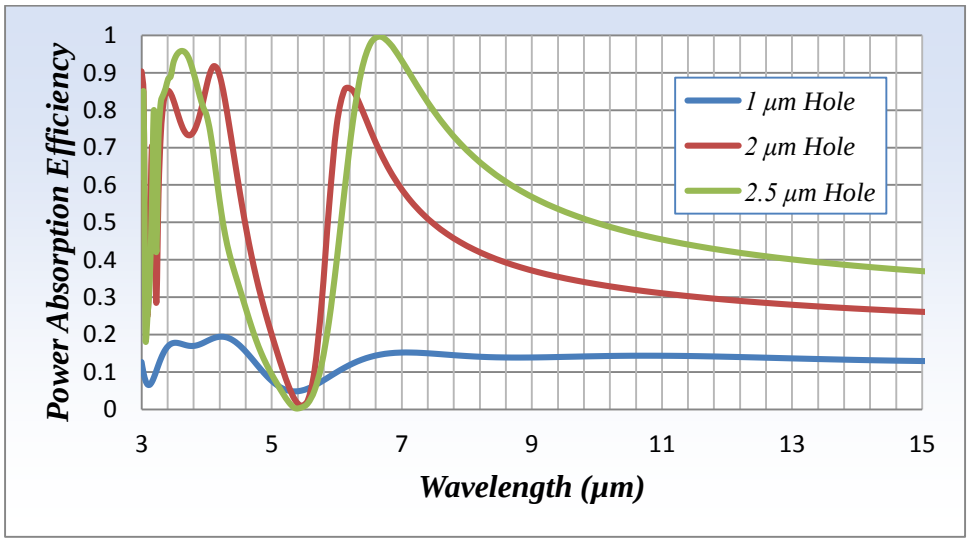

Figure 3.14 Hole size variation with 10 Ω: 1, 2, 2.5 μm.

For the second case of the holes at the edge, 2 μm, 2.5 μm, and 2.8 μm hole sizes are applied in the unit cell. When we consider the pixel, these holes are comparable with

the sizes of 4 μm, 5 μm, and 5.6 μm respectively. Figure 3.15 and 3.16 show the peak absorptions with *Rs* 1.5 Ω and 10 Ω.

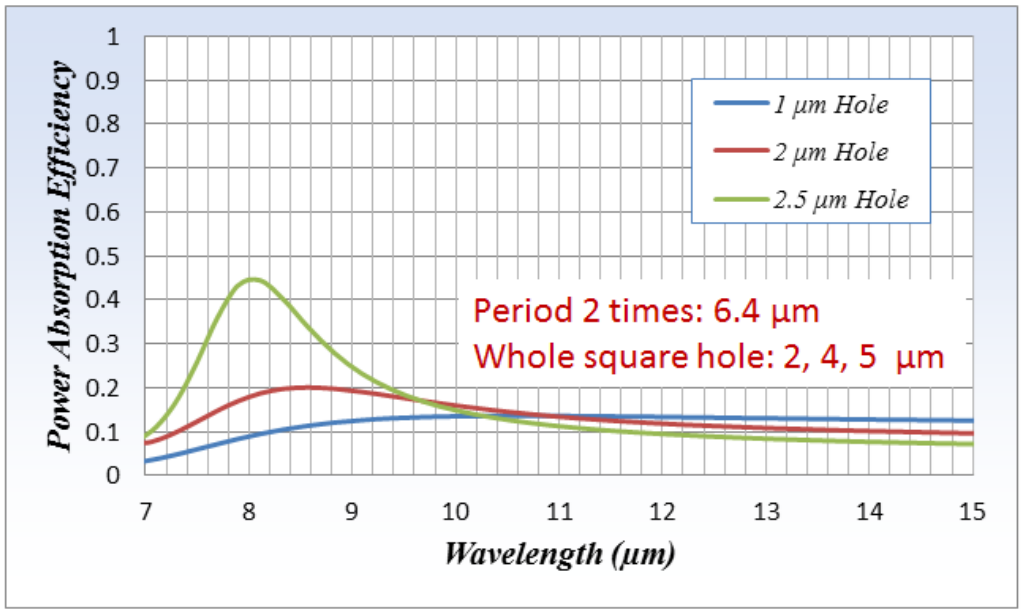

Figure 3.15 Hole size variation with 1.5 Ω: 1, 2, 2.5 μm.

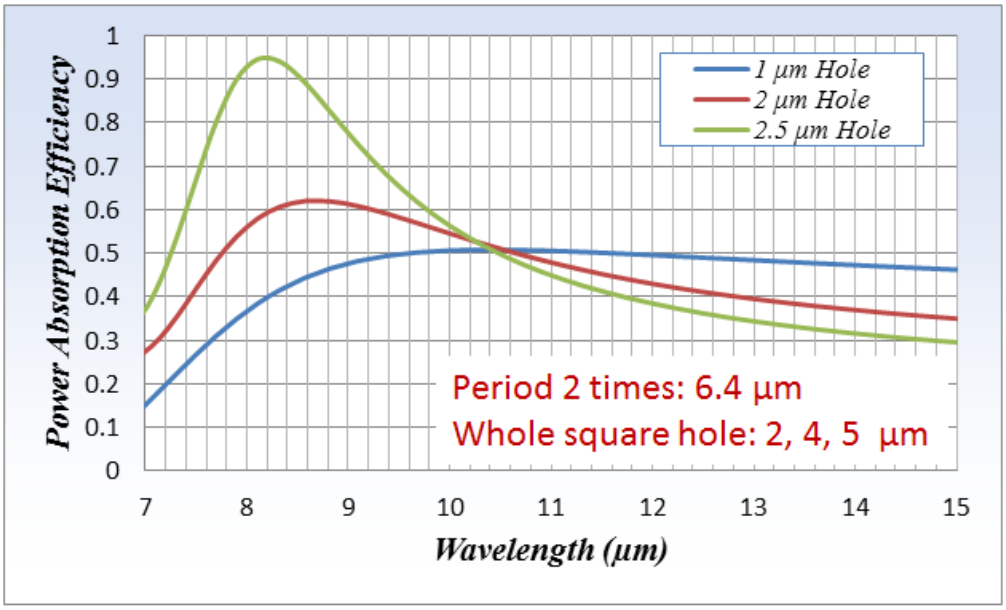

Figure 3.16 Hole size variation with 10 Ω: 1, 2, 2.5 μm.

Figure 3.17 shows the slot PRS with holes.

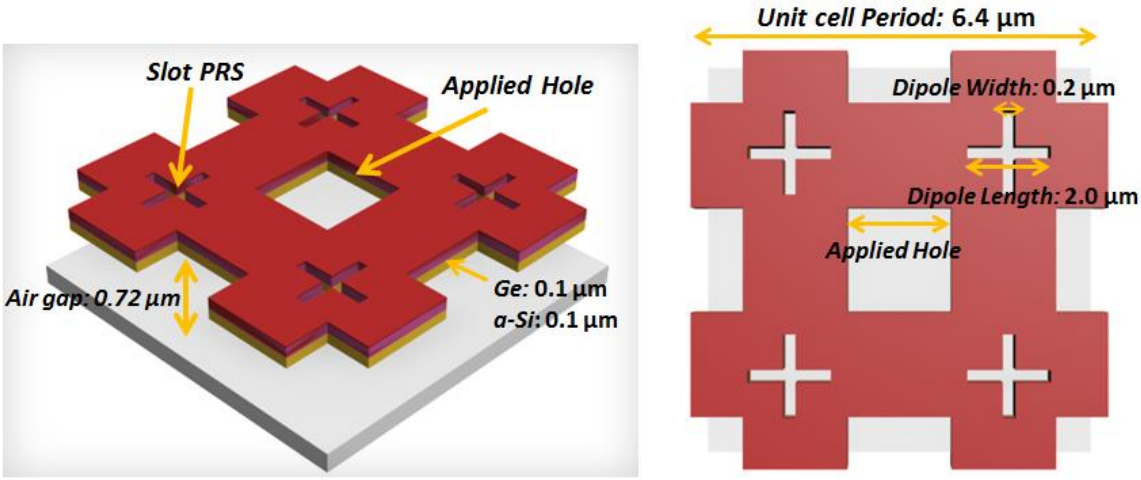

Figure 3.17 Slot PRS with holes.

Figure 3.18 shows the peak absorption at 10 µm peak. In this specific example, the square hole for the same 10 µm peak absorption was chosen. The slot length is 4.2 µm, and the width is 0.4 µm. The period is 6.4 µm with *Rs* 1.5 Ω, and the air gap is 2.5 µm.

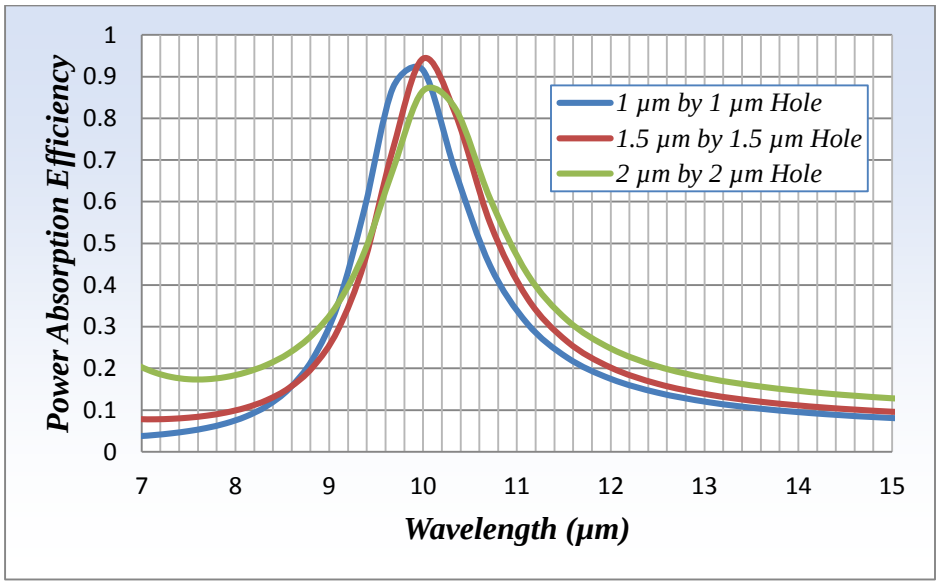

Figure 3.18 10 µm peak absorption slot PRS with hole design.

This chapter has examined square holes applied to patterned resistive sheets. Narrowband spectral selectivity in 10 μm peak absorption in both the dipole PRS and the slot PRS are maintained after applying the holes. Thermal mass can be reduced by 50 percent and still maintain spectral selectivity.

Chapter 4 3D Stacked Two-Color Microbolometer Design

Multispectral imaging requires more than two signals from the different bands to obtain different information from the same target, and several designs for dual-band microbolometer have been recently suggested. In the microbolometer design, the dual-band design is distinguished from the design that uses the photon detector as well as other antennae-based designs because the thermal detector is not able to discern the band of the signal absorption after receiving the signal. The thermal detector must receive and recognize the separate signal from the different bands, suggesting that dual-band design requires the absorptions in the two different bands, and moreover, each band must absorb the signal separately only from the targeted band.

The conventional microbolometer using the Jaumann absorber has limited use of the design parameters. Only adequate selections of the layer thickness and *Rs* can comprise the main parameters for the peak tuning. There are also degradations due to the inevitable interference that occurs between the layers. Moreover, finding adequate thicknesses of the layers is not easy, although we can use a parametric study such as the genetic algorithm to do so [26, 27]. Another approach utilizes actuation to adjust the peak absorption [30, 31]; however, this results in a complicated structure due to the bias in applying actuation. Such structure also degrades the absorptions in the target wavelengths. In this chapter, new unique dual-band design using stacked PRS is introduced to overcome the limits evinced in the previous designs.

4.1 TWO-COLOR DESIGN OF THE DUAL-BAND MICROBOLOMETER

The new design is composed of two stacked layers with different types of PRS and mirror. Both dipole and slot PRS achieve 100 percent power-absorption efficiency of the individual layer by using the appropriate size of patterns and layer thickness including the air gap [15]. Figure 4.1 (a) shows the out-of-band transmission characteristic of the dipole PRS. In the dipole PRS, all incident waves except the resonance wavelength can transmit and reach to the next layer. Figure 4.1 (b) shows the out-of-band reflection characteristic of the slot PRS. In slot PRS, all incident waves, except the resonance wavelength, are reflected. Therefore, the slot PRS can be considered to function as a mirror out of the resonant wavelength region if there is a layer on top of the slot PRS layer.

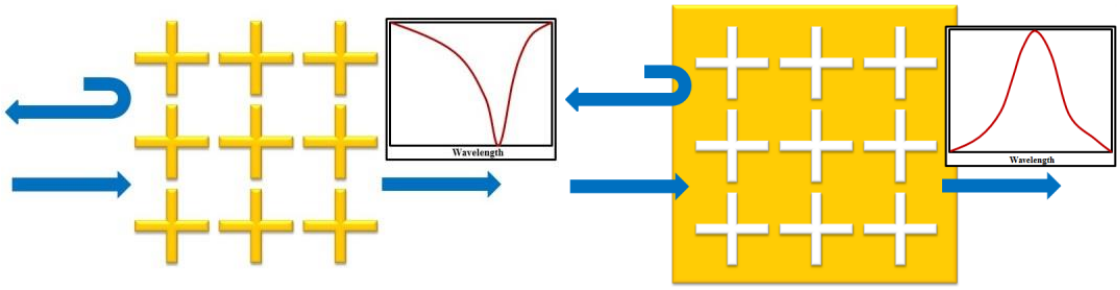

(a) (b)

Figure 4.1 Characteristics of PRS: (a) Out-of-band transmission characteristic of dipole patterned resistive sheet; (b) Out-of-band reflection characteristic of slot-patterned resistive sheet.

Figure 4.2 shows the peak absorption using dipole and slot PRS with mirrors. Figure 4.2 (a) is the peak absorption at 5 μm wavelength using the dipole PRS. Figure 4.2 (b) is the peak absorption at 10 μm wavelength using slot PRS.

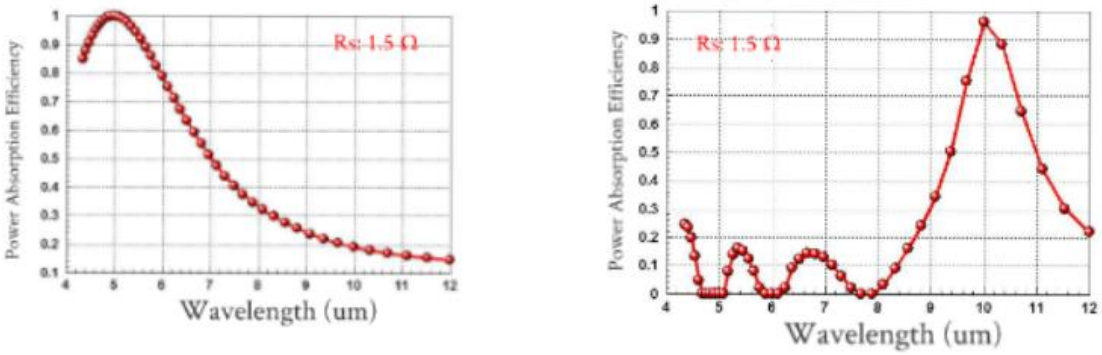

(a) (b)

Figure 4.2 Peak absorption using the dipole PRS at 5 μm wavelength (a) and slot PRS at 10 μm wavelength.

In single-band absorption, the single layers of each dipole or slot PRS with mirror achieve the peak absorption at the target wavelength without considering out-of-band transmission and reflection characteristics. The use of the single PRS considers only the power-absorption efficiency of the target wavelength. However, in the case of the stacked-layer microbolometer, there is a remarkable improvement of the power-absorption efficiency if the dipole PRS and slot PRS layers are used for the top and bottom layers respectively. In general, there are four cases of using PRS layers for the stacked structure. Each layer can use either the dipole PRS or slot PRS; therefore, four combinations of dipole and slot PRS are possible: (1) dipole-dipole PRS, (2) dipole-slot PRS, (3) slot-dipole PRS, and (4) slot-slot PRS pairs. Among these, the dipole-slot PRS is the most suitable selection for the dual-band application because of the layer's band

characteristics. In Figure 4.3, the top layer comprises the dipole PRS, and the bottom layer the slot PRS. Between each layer including the mirror, the λ/4 air gap as a quarter-wave transformer improves the absorption. First, the top dipole layer is designed to have a peak wavelength at 5 μm, and second slot layer is designed to have a peak wavelength at 10 μm.

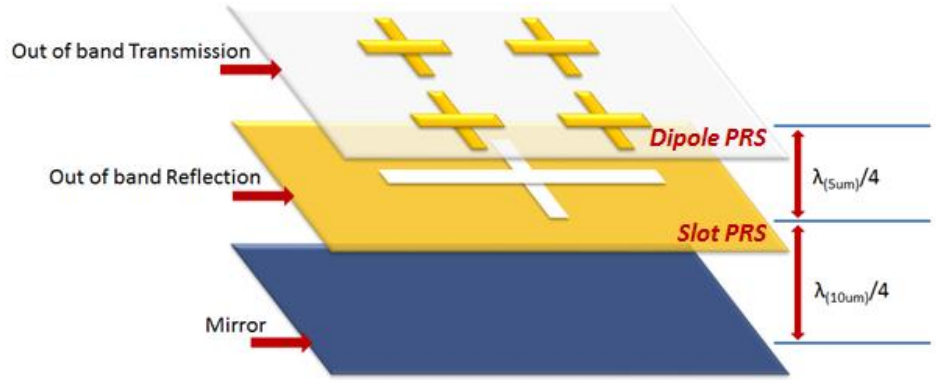

Figure 4.3 Dipole-slot-mirror-stacked structure for improved power-absorption efficiency.

This combination is changeable: the top dipole PRS layer can be designed for the 10 μm band and the bottom slot PRS layer can be designed for another band, 5 μm. As a first layer, the dipole PRS layer is selected because of its out-of-band transmission characteristic, which allows all bands except for the dipole resonant wavelength to have a possibility of being absorbed by the second layer. Moreover, the second layer has the slot PRS because of its out-of-band reflection characteristic, allowing the second layer to work as a mirror to the first layer for the improvement of power absorption. This also provides the advantage of reducing interference among the layers and manipulating stacked dual-band with improved power-absorption efficiency. Figure 4.4 shows the mechanism of the top dipole and bottom slot PRS layer designs to improve the peak absorptions using the out-of-band transmission and reflection characteristics.

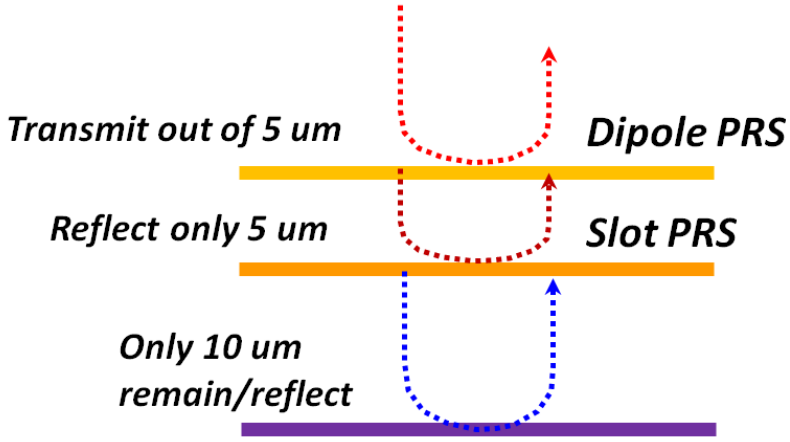

Figure 4.4 Dipole-slot-mirror-stacked structure for improved power-absorption efficiency.

The typical cross-dipole and cross-slot PRS are used because these patterns have no polarization preference. Generally any shape of the dipole and slot PRS can be used in this stacked structure to take advantage of the transmission and reflection characteristics.

4.2 VERIFICATION OF THE ABSORPTION MECHANISM

The dual-band microbolometer requires the separate layer's absorption to sense two different infrared signals. To verify the separate absorption, two approaches are used using full wave calculations (Ansoft HFSS^{TM}), which provide the scattering parameters and current distribution of the different layers. Utilizing the scattering parameters, waves that are transmitted, reflected, and absorbed can be calculated. With the current distribution, absorption can be calculated by integrating the current on each layer. In the following section, two approaches are introduced for verifying the dual-band design of the microbolometer.

4.2.1 Dual-band design verification using scattering parameter calculation

With simulated S_{11} and S_{21}, the normalized power efficiency of reflection and transmission can be calculated by taking the square of each scattering parameter. Then absorption-power efficiency can be calculated with the formula $1-|S_{11}^2|-|S_{21}^2|$. The $|S_{21}^2|$ represents the transmitted power. There is no transmitted power in the conventional microbolometer which has the mirror; therefore, $|S_{21}^2|$ should be zero. Figure 4.5 shows the freestanding structure with mirror which is tuned for the peak absorption at 5 μm target wavelength. The dipole length is 1.75 μm, and the width is 0.15 μm.

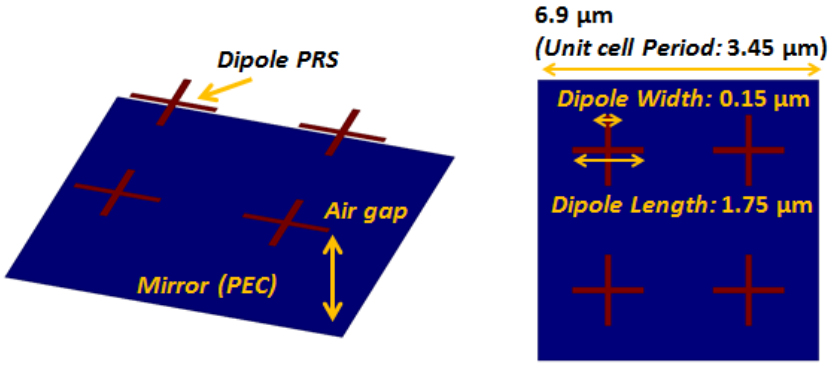

Figure 4.5 Dipole PRS with mirror for 5 μm target wavelength.

Figure 4.6 shows the power-absorption efficiency with different *Rs*. The absorption-power efficiencies are calculated with low (0.1 Ω, 1.5 Ω), high (15 Ω), and optimal (10 Ω) resistive sheet values in the case of the dipole PRS layer with mirror. The optimal *Rs* is 10 Ω for 100 percent power absorption.

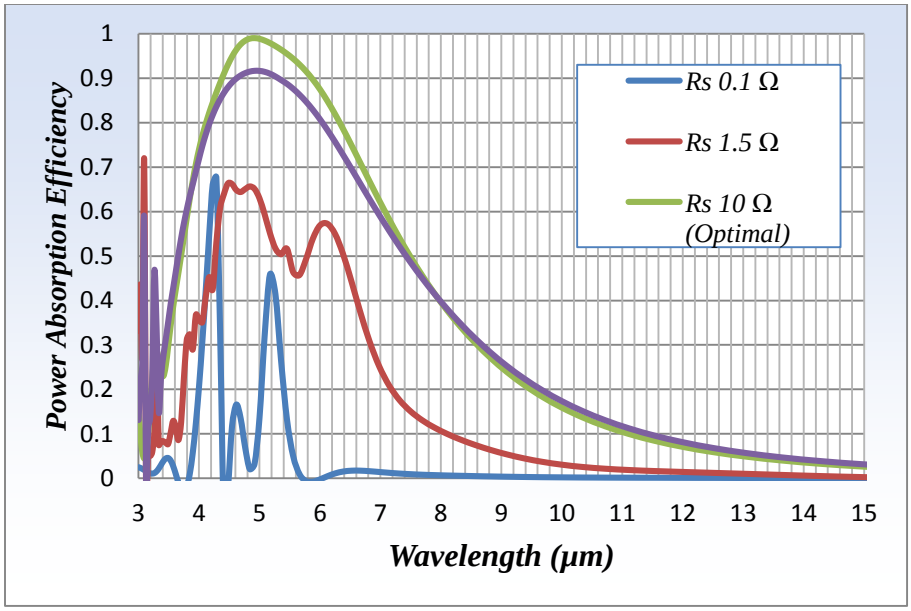

Figure 4.6 Power-absorption efficiency with different *Rs* in the dipole PRS with mirror.

To verify the absorption mechanism, considering the amounts of transmitted, reflected, and absorbed power, the mirror is removed to investigate the transmission, reflection, and absorption of the single layer. Figure 4.7 shows the freestanding dipole PRS single-layer structure for the 5 μm target wavelength without mirror. The dipole length is maintained with 1.75 μm, and the width is 0.15 μm. Resistance is changed in the same manner in the case with mirror.

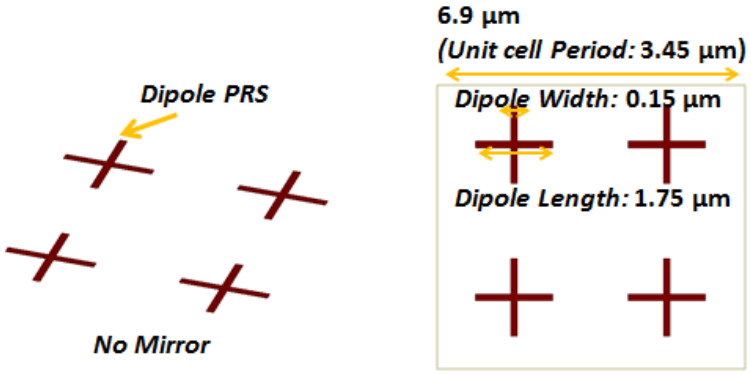

Figure 4.7 Dipole PRS without mirror for the 5 μm target wavelength.

Figure 4.8 shows the absorption, reflection, and transmission-power efficiencies with low, high, and optimal resistive sheet values for the dipole-patterned resistive sheet layer without mirror. The optimal value for the absorption-power efficiency of a single dipole layer is *Rs* 1.5 Ω with 50 percent power absorption. The low resistive sheet case (*Rs* 0.1 Ω) has both high reflection and high transmission, resulting in very little absorption. The high resistive sheet case (*Rs* 15 Ω) has very small reflection and relatively large transmission. Its absorption is reduced if the sheet resistance is increased compared to the optimal case of *Rs* 1.5 Ω. Figure 4.7 shows the out-of-band transmission characteristic of the dipole PRS. Other wavelength regions, except 5 μm, transmit most of the signal and shows the power-absorption efficiency near 1.

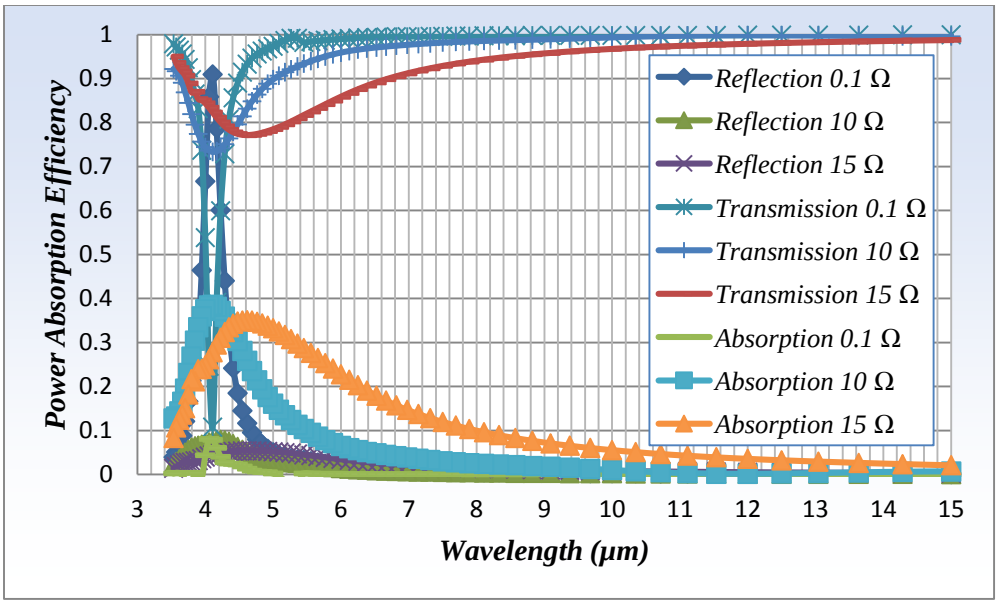

Figure 4.8 Absorption, reflection, and transmission power-absorption efficiencies for the dipole PRS.

The slot PRS structure is also examined. Figure 4.9 shows the slot PRS with mirror. The freestanding structure with mirror is tuned for peak absorption at 10 μm target wavelength. The slot length is 4.75 μm, and the width is 0.4 μm.

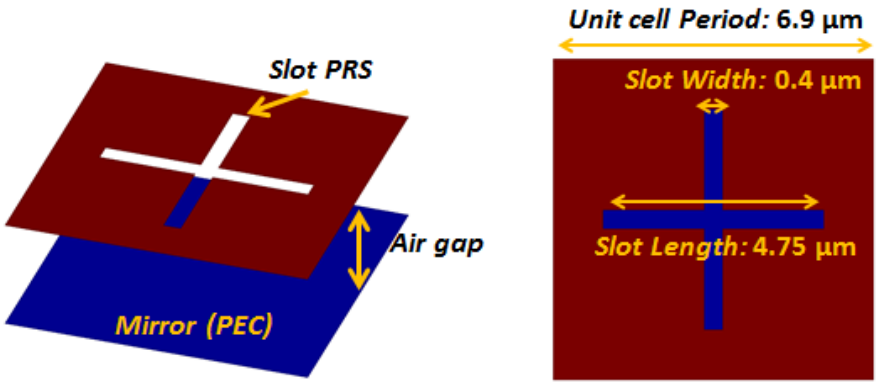

Figure 4.9 Slot PRS with mirror for 10 μm target wavelength.

Figure 4.10 shows the power-absorption efficiency with different *Rs*. The absorption-power efficiencies with low (0.1 Ω, 0.5 Ω), high (10 Ω), and optimal (1 Ω) resistive sheet values in the case of the slot PRS layer with mirror are simulated. The optimal *Rs* is 1 Ω, having almost 100 percent power absorption.

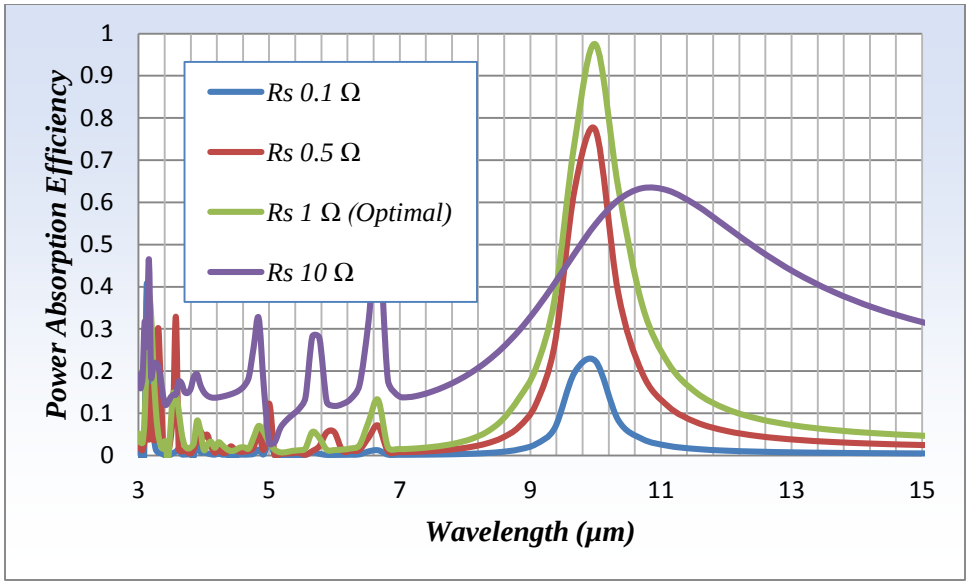

Figure 4.10 Power-absorption efficiency with different *Rs* in slot PRS with mirror.

The mirror is then removed in order to investigate the transmission, reflection, and absorption of the single layer. Figure 4.11 shows the freestanding slot PRS single layer structure for the 10 μm target wavelength without mirror. The dipole length is 4.75 μm, and the width is 0.4 μm. *Rs* is changed in the same manner in the case with mirror.

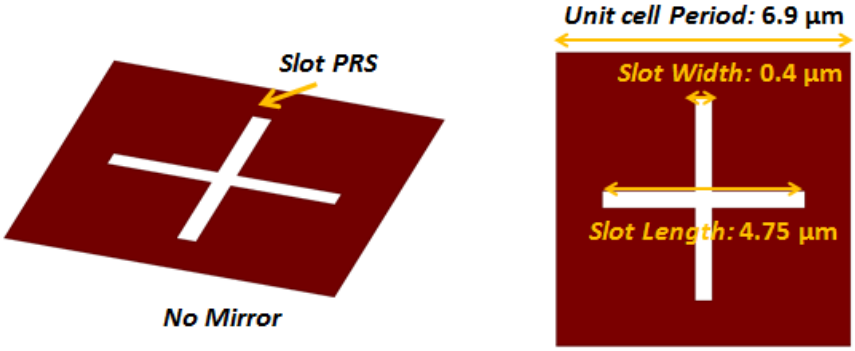

Figure 4.11 Slot PRS without mirror for 10 μm target wavelength.

Figure 4.12 shows absorption, reflection, and transmission power efficiencies with low, high, and optimal resistive sheet values in the case of the slot-patterned resistive sheet

layer without mirror. The optimal value for absorption-power efficiency of the single slot layer is also *Rs* 1.5 Ω with a 48 percent power absorption. For the low resistive sheet case, both reflection and transmission are high, and the absorption power is low. For the high resistive sheet case, absorption is less at the peak wavelength compares to the optimal case; moreover, it exhibits more broadband absorption as we increase sheet resistance.

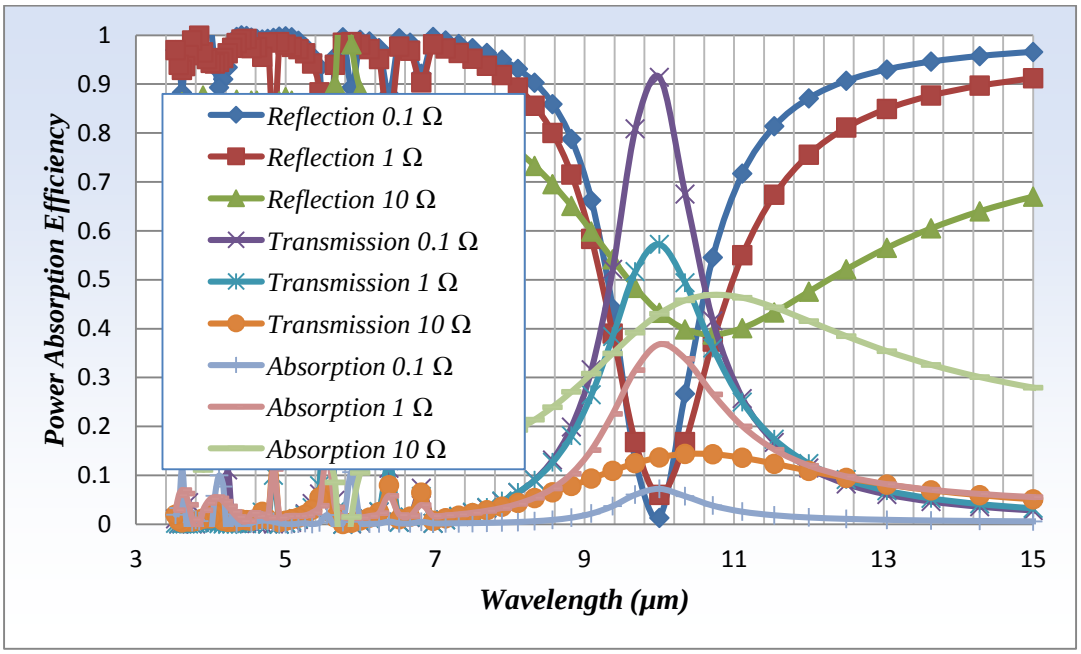

Figure 4.12 Absorption, reflection, and transmission power-absorption efficiencies for slot PRS.

Based on the verification process using scattering parameters, two layers are placed, and the optimal design parameters, including air gap, pattern shape and pattern size, are investigated. The parameters to determine better peak absorption at both the MWIR (5 μm) and LWIR (10 μm) bands are studied and optimized. A stacked-layer

structure has four possible combination selections: (1) slot-slot, (2) slot-dipole, (3) dipole-slot, and (4) dipole-dipole, for each layer's pattern type. The slot-slot layer case shows difficulty when functioning as a double-band absorber because the first slot layer reflects all out-of-band wavelength bands; therefore, the second layer exhibits mere absorption. The dipole-dipole case can work for dual-band absorber. However, the first layer is unable to benefit from the mirror due to the out-of-band transmission characteristic of the second layer. Interference between the second layer and the mirror makes the stack design challenging. In the slot-dipole case, the second layer cannot absorb the full incident radiation because of the first layer's out-of-band reflection. Our final option rests in is the dipole-slot case. The dipole-slot case benefits from the slot's out-of-band reflection. In this structure, the second slot-type layer works as a mirror to the first top layer. Moreover, the second layer's out-of-band reflection blocks the reflected waves from the mirror. Two different peaks and absorptions are obtained for individual layers. This will be introduced in the following section.

First, the freestanding design is considered for each layer in the stacked design. After finding the design parameters of the individual layer, the two individual layers are combined and the parameters are modified to achieve the desirable multispectral response. Design parameters are adjusted to obtain the maximum absorptions at the two peaks. Selected dipole and slot lengths are 1.75 μm and 4.75 μm respectively, which have two individual peaks at 5 μm and 10 μm. The width is also adjusted, and W1 (width for dipole PRS) and W2 (width for slot PRS) of 0.4 μm and 0.15 μm respectively are selected. For better absorption, the sheet resistances (*Rs1*, *Rs2*) and air gaps (g1, g2) are optimized. Unlike the single layer case, the sheet resistances have different optimum values for single layer (*Rs* 1.5 Ω) and dual layer (*Rs* 10 Ω) because of the different structure with stacked layers. Figure 4.13 compares dual-band absorptions and individual

absorptions. Optimal *Rs1* and *Rs2* of 10 Ω are used for the dual-band case. The traditional λ/4 gap for efficient quarter-wave absorption is applied for the air gap; however, the air gap can affect peak wavelength and bandwidth, although it is minor compared to the effects of pattern shape and size. After optimizing, 100 percent absorption at the expected peaks of the two wavelengths is obtained. This implies that the use of a dipole-slot pair stack layer improves absorption by 50 percent compared to the case of the dipole PRS without mirror, and by 52 percent compared to the slot-without-mirror case because of the mirror effect. The enhanced absorptions at both the MWIR (5 μm) and LWIR (10 μm) are achieved normalized power efficiency (see 1 in Figure 4.13).

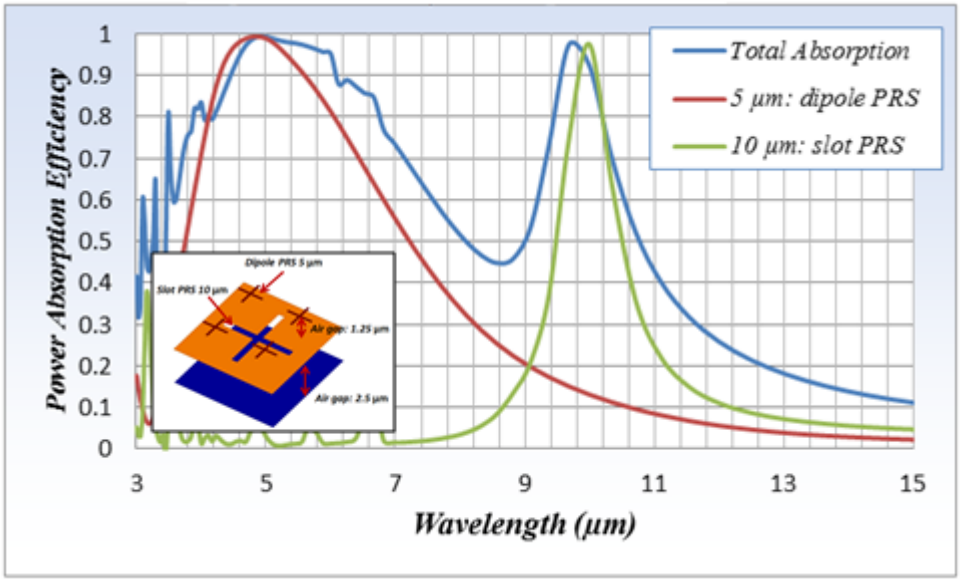

Figure 4.13 Absorption peaks between optimized dipole-slot stack layer and each individual layer; Red: MWIR, only dipole-patterned layer; Blue: LWIR (10 μm), only slot-patterned layer; Black: dual-band stacked layers.

Without the main design rule to maintain the top dipole PRS layer and the bottom slot PRS layer, each layer's target wavelength can be affected. Therefore, both top and

bottom layers can be designed to target both 5 μm and 10 μm wavelengths respectively. Figure 4.14 shows the example of the dipole PRS being used for 10 μm peak absorption and the slot PRS being used for 5 μm peak absorption. The air gap is also tuned for each layer's target absorption.

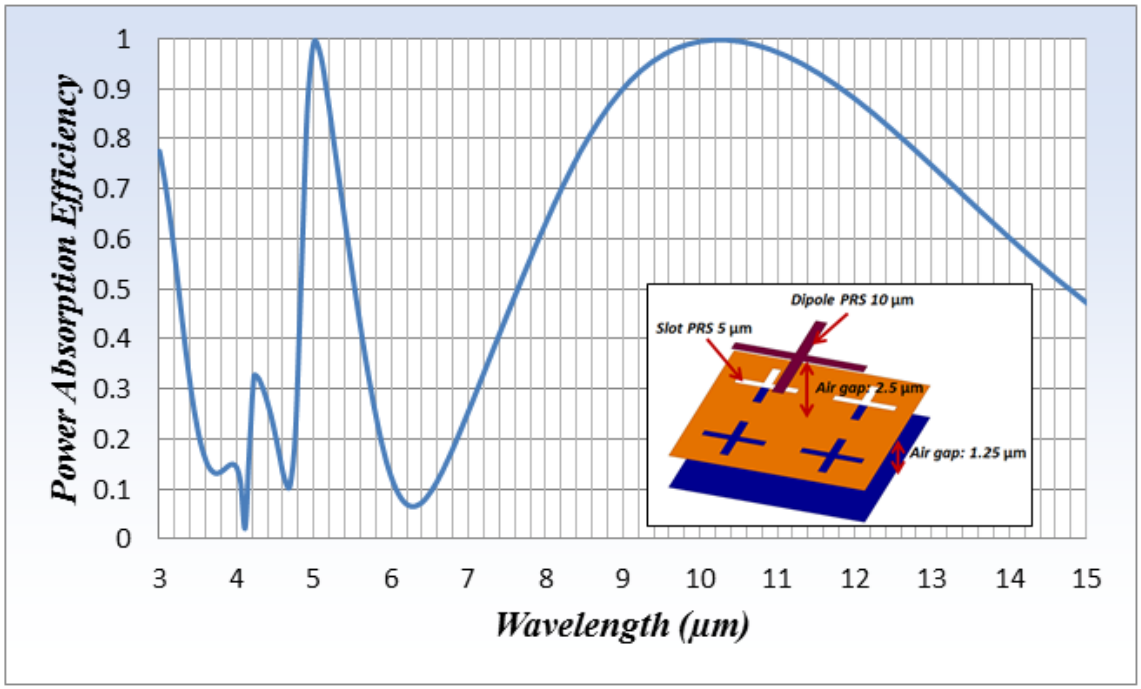

Figure 4.14 Dipole PRS for 10 μm peak absorption, Slot PRS for 5 μm peak absorption.

Two peaks can be clearly achieved by the stacked structure using dipole and slot PRS. However, this is not enough to eliminate the possibility of overlapping signals. Figure 4.15 shows the overlapped situation. In the Figure 4.15, the total absorption appears separated in each band (5 μm and 10 μm); however, the two peaks are generated with the sum of the mixed absorptions from both bands. Therefore, the design can be considered as a dual band; therefore, the approach to calculate the power-absorption

efficiency using scattering parameter cannot guarantee the separate signal absorptions in each layer.

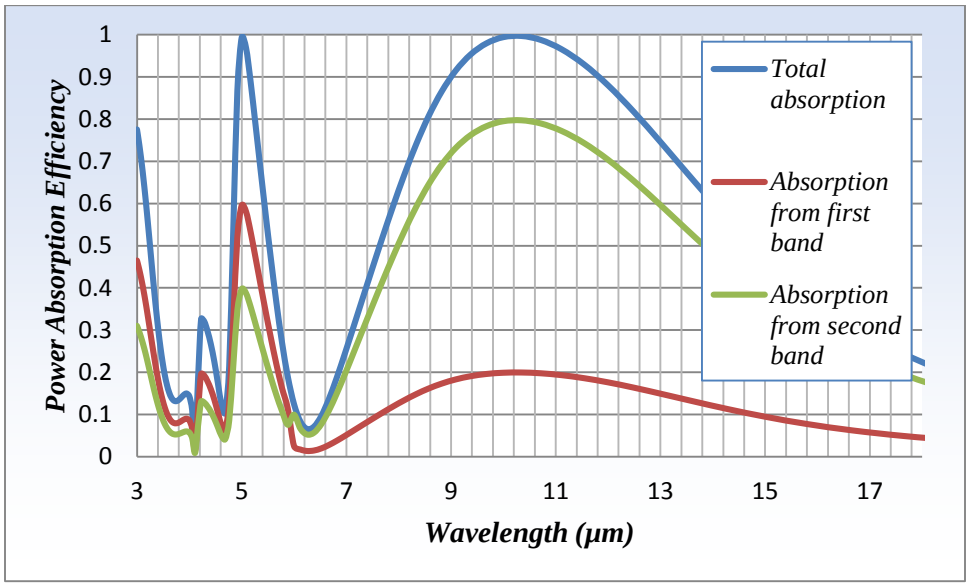

Figure 4.15 Example of the overlapped dual-band (not two-color) absorption.

4.2.2 Dual-band design verification using current distribution

In this section, the current distribution is introduced to verify each layer's individual absorption. Current distribution on the layer can be integrated and directly calculated into the absorbed power of the layer. Using the current distribution, we can observe the overlapped signal and distinguish the two-color absorptions. Same-stacked designs in the previous section are used to compare the power absorption between scattering parameters and current distribution. Figure 4.16 shows the power-absorption efficiency of the stacked design using a dipole PRS targeted at 5 μm and slot PRS targeted at 10 μm.

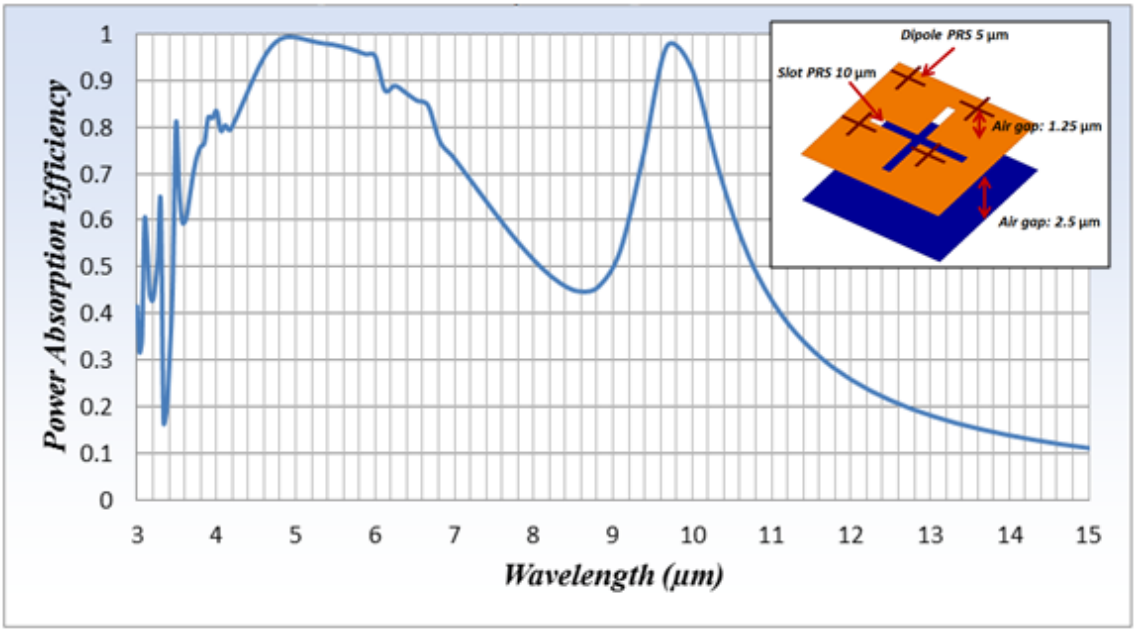

Figure 4.16 Power-absorption efficiency of the stacked design using a dipole PRS targeted at 5 μm and a slot PRS targeted at 10 μm.

Figure 4.17 shows current distributions of the stacked design using a dipole PRS targeted at 5 μm and a slot PRS targeted at 10 μm. For the first peak absorption at 5 μm, the dipole PRS absorbs the power dominantly, and the maximum surface current density (Jsurf: A/m) of the dipole PRS shows around 2.08×10^5 (A/m), whereas the bottom slot PRS shows around 3×10^2 (A/m) surface current density. For the second peak absorption at 10 μm, the bottom slot PRS has a dominant absorption which has 3.97×10^5 (A/m). Comparatively, the dipole PRS has a lower surface current density with 2.61×10^4 (A/m). In the middle junction of the 8.6 μm, the signals are absorbed by both the dipole PRS and slot PRS; moreover, the difference of maximum surface current density is less than the cases of the two peak absorptions.

	Top Dipole PRS Layer	Bottom Slot PRS Layer
1st Peak at 5 μm	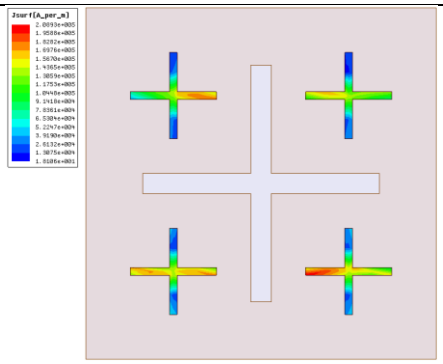	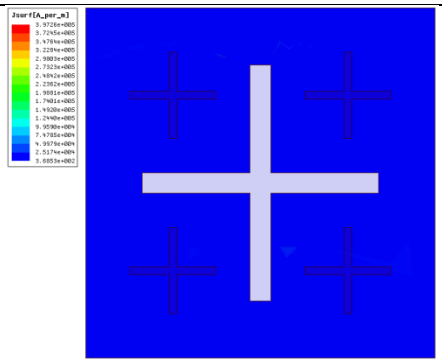
2nd Peak at 10 μm	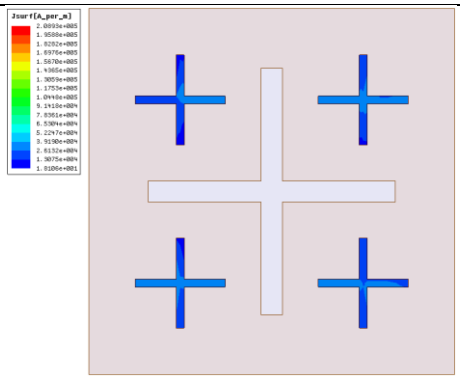	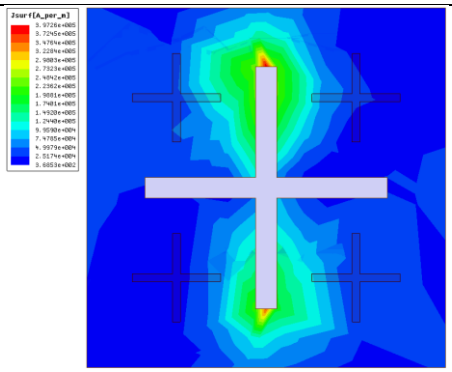
Middle junction at 8.6 μm	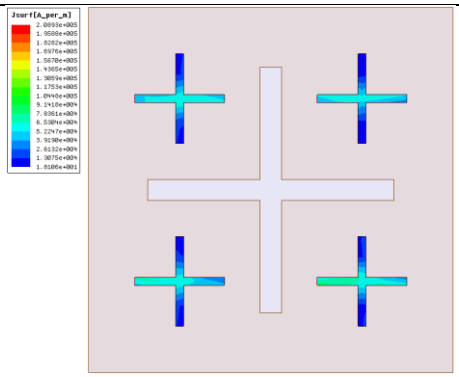	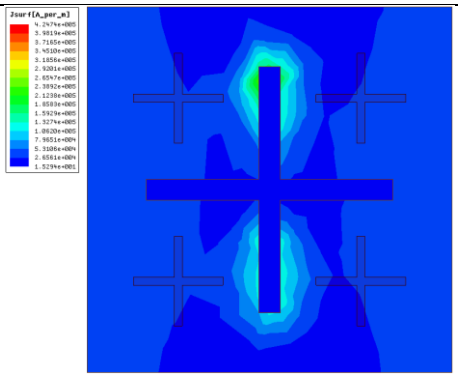

Figure 4.17 Current distributions of the stacked design using a dipole PRS targeted at 5 μm and slot PRS targeted at 10 μm.

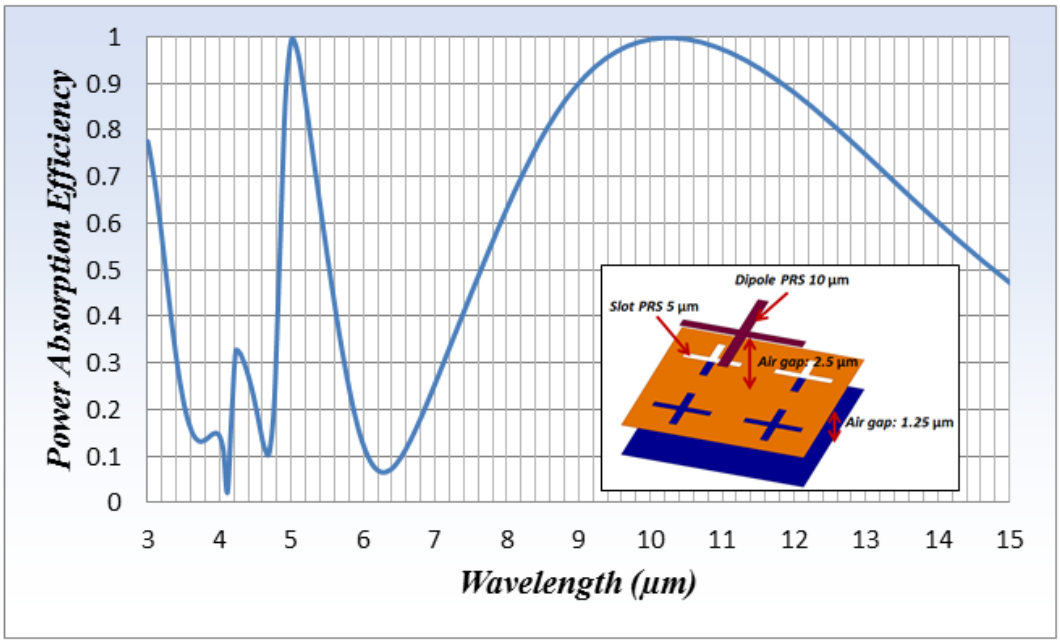

Figure 4.18 Power-absorption efficiency of the stacked design using a dipole PRS targeted at 10 μm and slot PRS targeted at 5 μm.

Figure 4.19 shows current distributions of the stacked design using a dipole PRS targeted at 10 μm and a slot PRS targeted at 5 μm. For the first peak absorption at 10 μm, the dipole PRS absorbs the power dominantly, and the maximum surface current density (Jsurf: A/m) of the dipole PRS shows around 2.52×10^5 (A/m), whereas the bottom slot PRS shows around 6.4×10^1 (A/m) surface current density. For the second peak absorption at 5 μm, the bottom slot PRS has a dominant absorption of 6.3×10^4 (A/m). Instead, the dipole PRS has a lower surface current density of 5.61×10^5 (A/m). In the middle junction of the 6.4 μm, the signals are absorbed by both the dipole PRS and slot PRS; moreover, the difference of maximum surface current density is less than the cases of two peak absorptions.

	Top Dipole PRS Layer	Bottom Slot PRS Layer
1st Peak at 5 μm	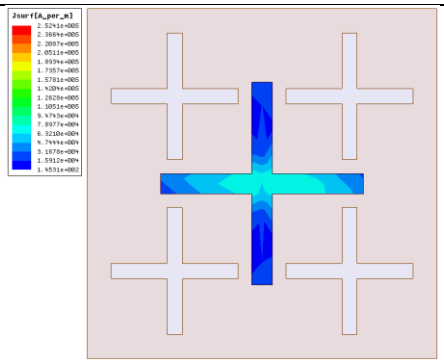	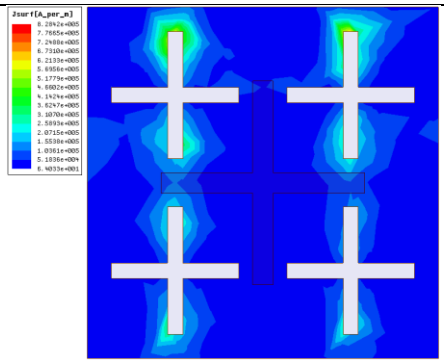
2nd Peak at 10 μm	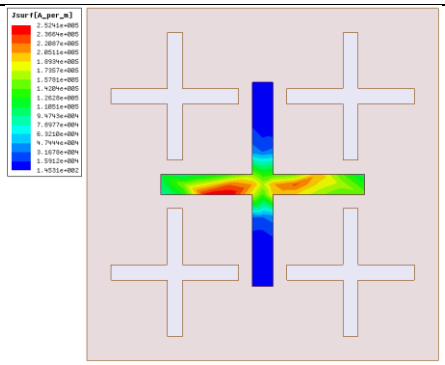	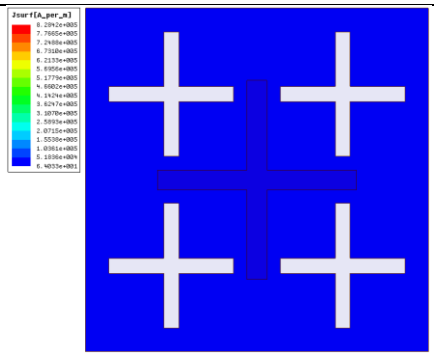
Middle Junction at 6.4 μm	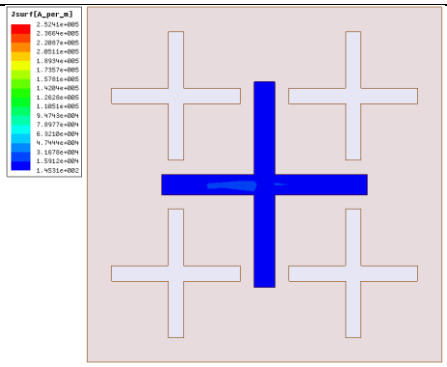	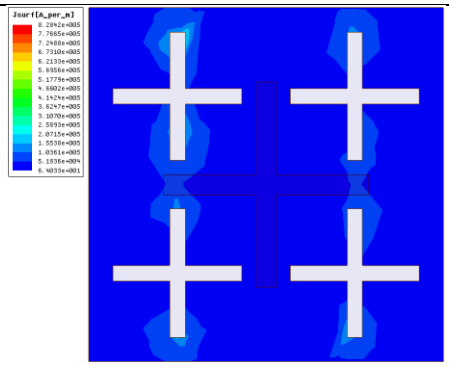

Figure 4.19 Current distributions of the stacked design using a dipole PRS targeted at 10 μm and slot PRS targeted at 5 μm.

The above two examples of stacked design demonstrate that the separate signal absorptions are not perfectly achieved, and powers are generated both top and bottom layers in the first peak at 5 μm. In the following section, more realistic stacked design

with dielectric layers are considered; moreover, the approach to minimize the overlapped signals is studied.

4.2.3 Dual-band design verification using different PRS patterns

The suggested stacked designs use the top dipole PRS and bottom slot PRS structure to improve the peak absorptions of individual layers. Although the pattern shape is changed, the order of the stacked dipole and slot-type PRS layers provides an advantage in improving the absorptions of individual layers. Figure 4.20 shows the circular patterns which are applied for the dual-band stacked microbolometer. This design applies only to different pattern shape and circular pattern, and maintains other design parameters such as pattern type and air gap. The radius of the circular pattern is optimized for the maximum peak absorption in the desired band, and sheet resistances of the patterns are optimized to achieve the peak absorption at the desired wavelength. Compared to the cross-shaped PRS patterns, the circular (or comparable) pattern design provides an advantage in fabrication because of its simple patterning. Its example verifies the hypothesis that the use of dipole- and slot-type PRS with any shape works to take advantage of out-of-band transmission and reflection, under the condition that the dipole PRS is used for the top layer and the slot PRS is used for the bottom layer.

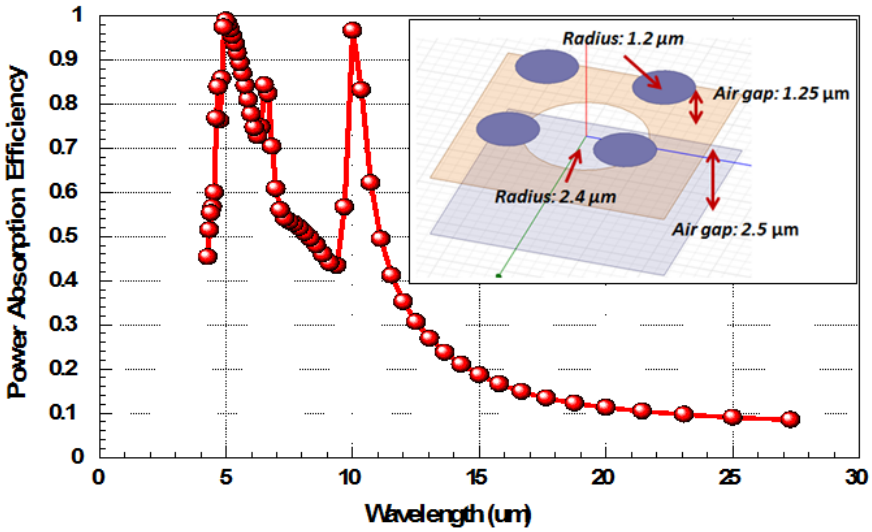

Figure 4.20 Applying circular shape PRS for the dual-band stacked microbolometer.

4.3 ADDING DIELECTRIC LAYER AND BOLOMETRIC LAYER

Like the single layer design, the freestanding structure in the stacked design should be supported with a dielectric supporting layer. Moreover, the metal absorber and bolometric layer should be added for more realistic design. In this section, the dielectric layers are applied, and the two-color separate absorptions are implemented by optimizing design parameters. The design using a top dipole PRS for 10 μm and a bottom slot PRS for 5 μm is mainly considered among the different candidates. With this initial design, fabrication of small patterns can be easier because of the dielectric effect. The slot PRS with undercut is selected for the bottom layer for 5 μm. The pattern size can be considerable compared to the case of the freestanding structure. Moreover, top dipole

PRS patterns can be selected for the longer wavelength of 10 μm with the advantage of using a larger pattern size that provides easier patterning in fabrication. In the previous examination of the dielectric loading effect, it was shown that the peak absorptions are shifted to the longer wavelength, and these shifts can be tuned using smaller patterns and adjusting other parameters. Figure 4.21 shows the suggested stacked structure with dielectric layers. The main design parameters are the size and sheet resistances of the dipole and slot PRS and the two air gaps. Based on the previous study, these parameters here are optimized for the two-color–stacked design. The power-absorption efficiency is first achieved by the parametric study. Then, the surface current density in each layer is investigated to obtain the two separate absorptions.

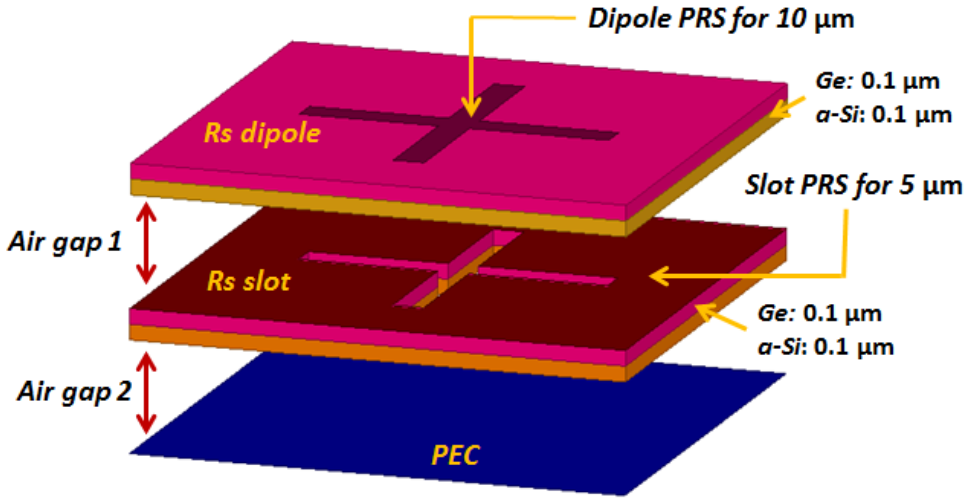

Figure 4.21 Applying dielectric layers with reduced dipole/slot size for wavelength peak tuning.

4.3.1 EXTRACTION OF THE DESIGN PARAMETERS

To find the initial design of the two-color–stacked microbolometer, the design parameters are studied and selected based on the parameters used in the previous sections. Target wavelengths are 5 µm in the MWIR and 10 µm in the LWIR. The top dipole layer is designed for 10 µm, and the bottom layer is designed for 5 µm. In the previous chapter, the dielectric loading effect in the design using the Salisbury screen was studied. Moreover, the 10 µm peak absorption was obtained by reducing the air gap in the structure using dielectric layers. The air gap was reduced from the quarter-wavelength of 2.5 µm to 0.72 µm. In the stacked layer, the target wavelength of the bottom slot layer was 5 µm. Figure 4.22 shows the shift of the peak absorption after adding the dielectric layers (0.1 µm *Ge* and 0.1 µm *a-Si*).

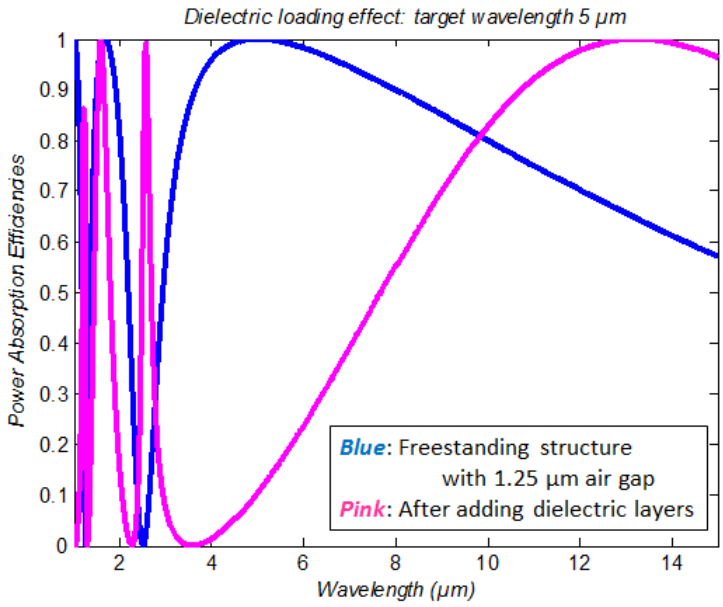

Figure 4.22 Dielectric loading effect at the target wavelength 5 µm.

The peak absorption is shifted to the longer wavelength, which is around 13 μm. In Figure 4.23, the air gap is reduced by 0.14 μm in order to tune the peak absorption at 5 μm.

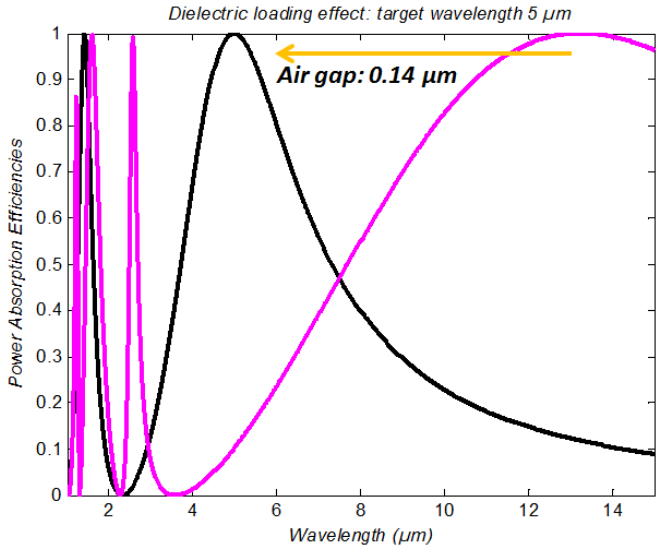

Figure 4.23 Tuning the peak absorption by reducing the air gap.

The air gaps of 0.72 μm and 0.14 μm are for the peak absorptions of 10 μm and 5 μm, respectively. In the stacked design, the air gap of 10 μm is varied from 0.72 μm to 2.5 μm, and the air gap for 5 μm is swept from 0.14 μm to 1.25 μm. The *Rs* from 0.5 Ω to 10 Ω is applied to both layers to optimize the peak absorption and reduce the interference between the bolometric layers.

The sizes of the dipole PRS and slot PRS can be obtained from the investigation of the single layer. Figure 4.24 shows the initial pattern sizes both in the top and bottom layers.

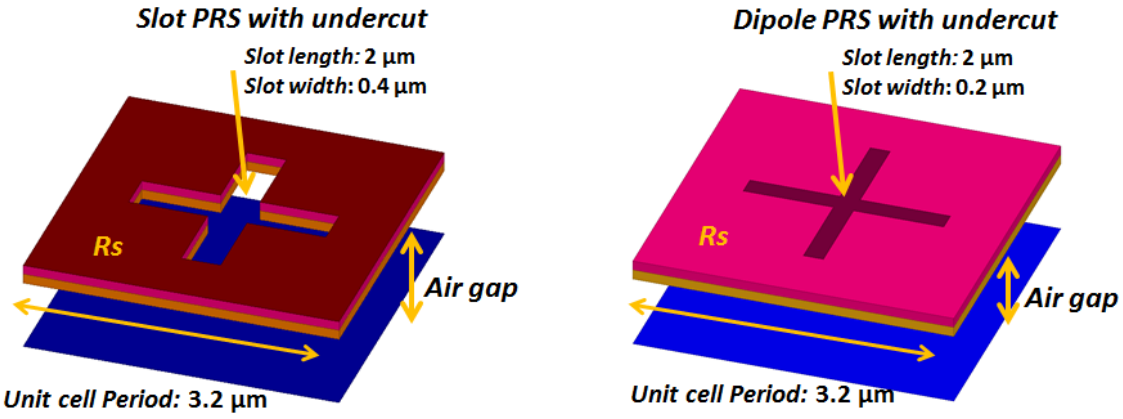

(a) (b)

Figure 4.24 Initial pattern sizes both in the top layer and the bottom layer.

4.3.2 OPTIMIZED TWO-COLOR–STACKED MICROBOLOMETER

The two-color–stacked microbolometer design is introduced, and the target peak absorptions are optimized by changing the design parameters. The main design parameters are the pattern size, air gap, and *Rs*. From the parametric study in the previous chapters, the candidates of each parameter are selected and used to find the optimal design. For both layers, *Rs* of 1 Ω, 1.5 Ω, 10 Ω are used initially. Three air gaps are applied, and three dipole lengths are used for the initial tuning. In the worst case, the number of trials is around 729. This trial number is estimated from the use of two layers with three parameters, 3^2 x 3^2 x 3^2. Figure 4.25 shows the optimized full microbolometer

with a stacked structure using a dipole and slot PRS. More tuning can be desirable to maximize peak absorption.

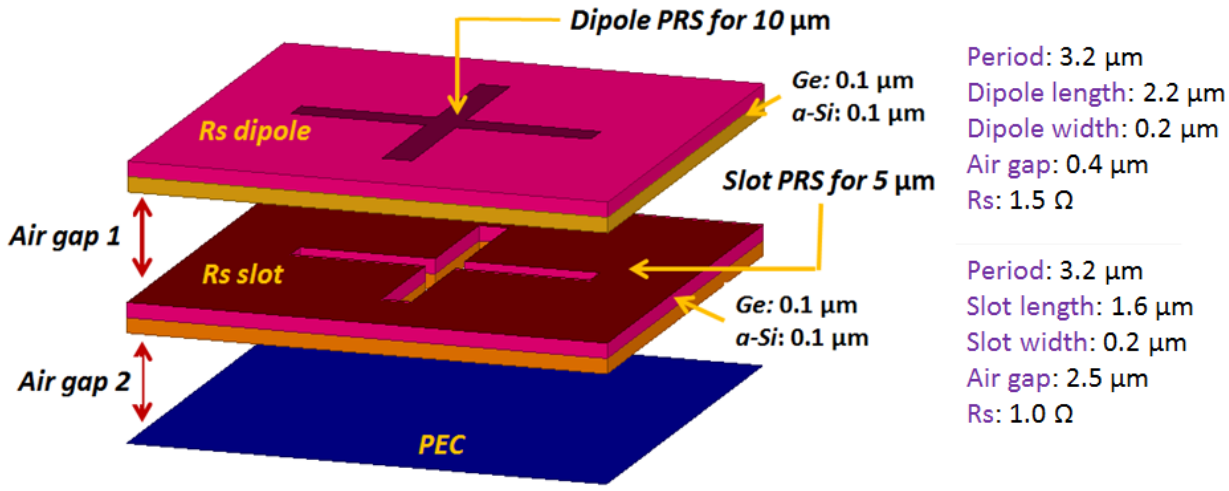

Figure 4.25 Optimized stacked design.

This design achieves dual bands at 4.83 µm and 9.37 µm with more than 99 percent power-absorption efficiency; moreover, these peak absorptions are improved compared to those in the designs of previous research [22-30] which show less than 70 ~ 80 percent power absorption efficiency. Figure 2.26 shows the power-absorption efficiency. However, there are undesirable peaks nearby the shorter target wavelength in MWIR which are generated by the second or third resonant mode from both top and bottom PRS layers.

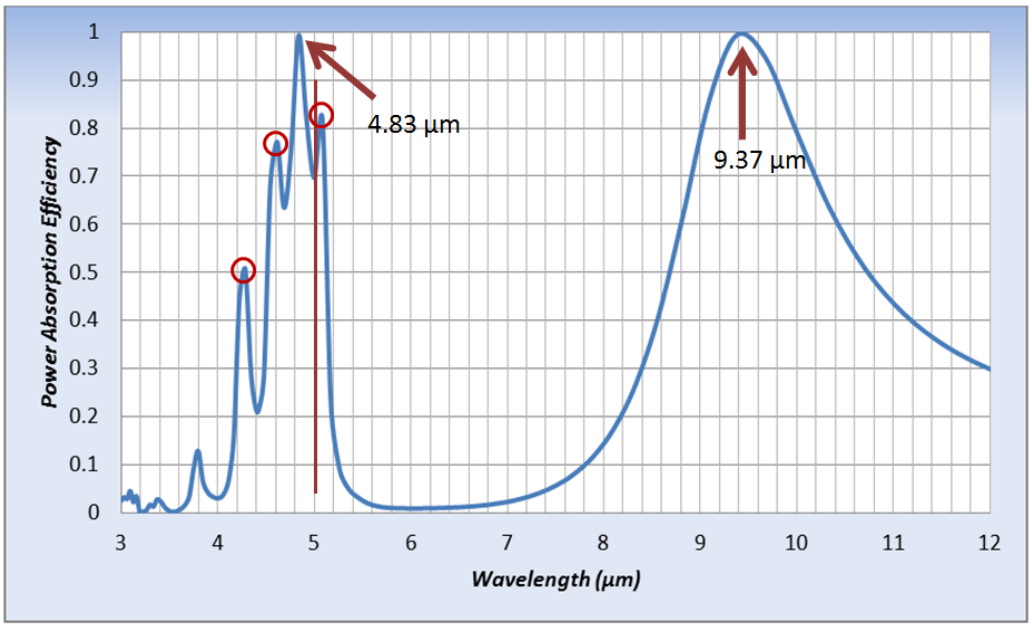

Figure 4.26 Applying dielectric layers with reduced dipole/slot size for wavelength peak tuning

Figure 4.27 shows the surface current density of each layer for the target wavelength. For each target wavelength, one layer has the maximum current distribution whereas the other layer shows very small current distribution, demonstrating that the two-color signals are absorbed and absorbed separately.

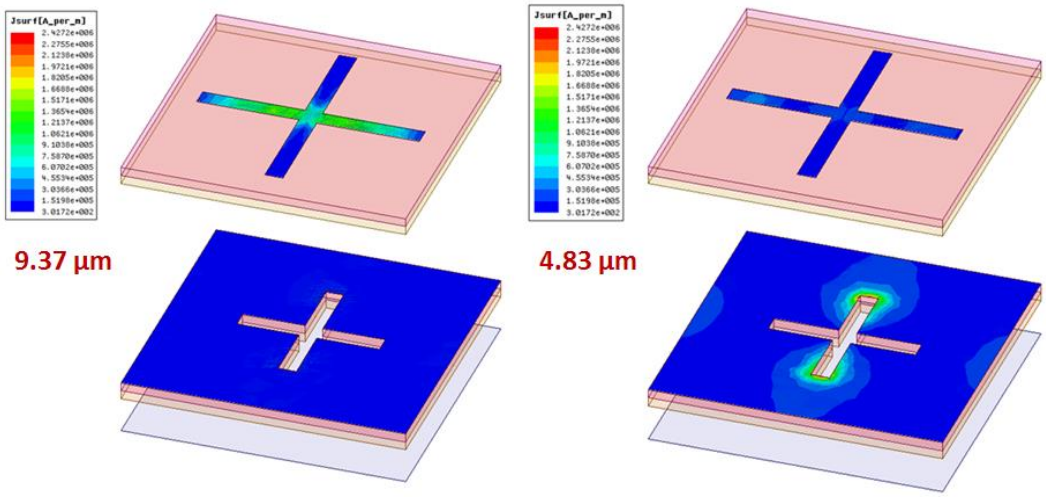

Figure 4.27 Individual absorptions at each layer (4.83 µm and 9.37 µm) and its current distribution at the corresponding wavelength.

The maximum surface current density (Jsurf: A/m) of the dipole PRS shows around 2.42x106 (A/m), whereas the bottom slot PRS shows around 3.0x102 (A/m) surface current density. In the shorter target wavelength in MWIR, the top dipole PRS layer shows higher surface current density around 3.0x105 (A/m) partially on the dipole pattern. However, 10 times difference of surface current density which is 102 times difference in the power is fairly good separation compared to other researches [22-30] which provides not only dual band absorption but also two color separate absorption.

Chapter 5 Conclusions

In this study, the fundamentals of patterned resistive sheets (PRS) are introduced for the potential application in the microbolometer. From the basic Salisbury screen to dual-band stacked application, the design parameters are thoroughly observed and investigated to verify the design process.

In Chapter 2, design parameters such as sheets resistance (*Rs*), air gap, material characteristics, including the skin depth and the dielectric-loading effect, were investigated. Moreover, the flexibility in the design using the parameters is introduced. The real metal (*Al*) which corresponds to the ideal resistive sheets is applied in the design. Both using *Rs* and real metal in the design has a good agreement. Moreover, it verifies that the use of resistive sheets in the design process can reduce simulation time without compromising the accuracy of the results.

In Chapter 3, designs using holes to reduce thermal mass are introduced. As initial designs, the adequate dipole and slot PRS are carefully selected based on the parameter study. Then, the holes are applied to reduce the thermal mass for the faster response. The differences between the dipole PRS and slot PRS emerge when the holes are applied; moreover, the suggested designs are shown to minimally change spectral selectivity while reducing thermal mass by more than 50 percent.

In Chapter 4, stacked dual-band designs are examined. These designs use the out-of-band transmission and reflection characteristics of each dipole and slot PRS. The suggested design contains the first top layer with dipole PRS and the second bottom layer with slot PRS for maximizing the peak absorptions at the target wavelengths. Moreover, the design shows better absorptions compared to other previous designs and obtains more robustness against interference between the layers. In addition, circular patch designs demonstrate that any dipole and slot-type PRS can be applied in the design process.

There are many possible trajectories for manufacturing based on this study. Adding holes in the stacked design is one clear application. Moreover, broadband design should be considered. The incident angle is also an important factor when we think of different applications using a few pixels. As the pixel size decreases, the number of periodic patterns in the PRS should be considered, and the small pixel itself may affect spectral selectivity.

Reference

1. Maxwell, J.C., *A dynamical theory of the electromagnetic field.* Philosophical Transactions of the Royal Society of London 155, 1865: p. 459–512.
2. Montwill, A. and A. Breslin, *Let there be light : the story of light from atoms to galaxies*. 2008, London Singapore ; Hackensack, NJ: Imperial College Press ;Distributed by World Scientific Pub. Co. xxxiii, 595 p.
3. *http://www.merriam-webster.com/*.
4. *Discovery of Infrared Light*.
5. *Cool Cosmos* http://coolcosmos.ipac.caltech.edu/cosmic_classroom/classroom_activities/herschel_experiment.html.
6. Cowles, T.H.B.a.R.B., *Physiology of an Infrared Receptor: The Facial Pit of Pit Vipers.* Science p. 541-543.
7. *http://www.nature.com/news/2010/100314/full/news.2010.122.html*.
8. Budzier, H., *Thermal infrared sensors : theory, optimization, and practice*. 2010, Chichester, West Sussex, U.K.: Wiley.
9. Rogalski, A., *Infrared detectors* 2nd ed. 2011, Boca Raton, FL CRC Press.
10. Kruse, P.W., *Uncooled Thermal Imaging: Arrays, Systems, and Applications*. 2001: SPIE Press.
11. Robert K. Willardson, E.R.W., David D. Skatrud, Paul W. Kruse, *Uncooled Infrared Imaging Arrays and Systems Volume 47 of Semiconductors and semimetals*. 1997: Academic Press.
12. Wood, R.A. *Uncooled thermal imaging with monolithic silicon focal planes*. Place of Publication: San Diego, CA, USA. Country of Publication: USA.: SPIE SPIE.
13. Tissot, J.L., *IR detection with uncooled sensors.* Infrared Physics & Technology, 2004. **46**(1–2): p. 147-153.
14. Hwang, T.L., S.E. Schwarz, and D.B. Rutledge, *Microbolometers for infrared detection.* Applied Physics Letters, 1979. **34**(11): p. 773-776.
15. Munk, B.A., *Frequency Selective Surfaces : Theory and Design*. 2005, Hoboken: John Wiley & Sons.
16. *http://www-lep.gsfc.nasa.gov/code693/tdw03/proceedings/docs/session_2/Ngo.pdf*.
17. Rogalski, A., *Infrared detectors for the future.* Acta Physica Polonica A, 2009. **116**(3): p. 389-406.
18. Rogalski, A. *Competition of infrared detector technologies*. in *Proceedings of the SPIE - The International Society for Optical Engineering*. 2003. Place of Publication: Kiev, Ukraine. Country of Publication: USA.: SPIE-Int. Soc. Opt. Eng. SPIE.
19. Rogalski, A., *Recent progress in third generation infrared detectors.* Journal of Modern Optics, 2010. **57**(18): p. 1716-1730.

20. Rogalski, A., *Third generation infrared detectors.* Elektronika, 2006. **47**(3): p. 19-27.
21. *http://www.ircam.de/produkte/geminis_rerie_e.php*.
22. Rogalski, A., *Dual-band infrared detectors.* Journal of Infrared and Millimeter Waves, 2000. **19**(4): p. 241-258.
23. Reibel, Y., et al. *Infrared dual-band detectors for next generation*. Place of Publication: Orlando, FL, USA. Country of Publication: USA.: SPIE - The International Society for Optical Engineering.
24. Rogalski, A. *Dual-band infrared focal plane arrays*. Place of Publication: Moscow, Russia. Country of Publication: USA.: SPIE-Int. Soc. Opt. Eng. SPIE SPIE.
25. Almasri, M., X. Bai, and J. Castracane, *Amorphous silicon two-color microbolometer for uncooled IR detection.* IEEE Sensors Journal, 2006. **6**(2): p. 293-300.
26. Sangwook, H., J. Joo-Yun, and P.N. Dean. *Multilayer Fabry-Perot microbolometers for infrared wavelength selective detection*. Place of Publication: Orlando, FL, USA. Country of Publication: USA.: SPIE - The International Society for Optical Engineering.
27. Han, S.W., Y.S. Park, and D.P. Neikirk, *Broadband infrared detection using Jaumann absorbers with genetic algorithm.* Electronics Letters, 2005. **41**(24): p. 1307-1308.
28. Yu-Guang, G., et al., *Uncooled infrared detection with two-color microbolometers using a micro-optoelectromechanical systems tunable micromirror.* Journal of Microlithography, Microfabrication, and Microsystems, 2010. **9**(3): p. 031005.
29. Henan, Z., et al. *Study on Optical Properties of Two-Color Microbolometers*. Place of Publication: Dalian, China. Country of Publication: USA.: SPIE - The International Society for Optical Engineering.
30. Woo-Bin, S. and J.J. Talghader, *Design and characterization of adaptive microbolometers.* Journal of Micromechanics and Microengineering, 2006. **16**(5): p. 1073-1079.
31. Keskin, S. and T. Akin. *The first fabricated dual-band uncooled infrared microbolometer detector with a tunable micro-mirror structure*. 2012.
32. Yong-qiang, P., Z. Yong-jiang, and W. Jun, *Equivalent circuit method analysis of the influence of frequency selective surface resistance on the frequency response of metamaterial absorbers.* Journal of Applied Physics, 2011. **110**(2): p. 023704.
33. Yongzhi, C. and Y. Helin, *Design, simulation, and measurement of metamaterial absorber.* Microwave and Optical Technology Letters, 2010. **52**(4): p. 877-880.
34. Chihhui, W., et al., *Large-area wide-angle spectrally selective plasmonic absorber.* Physical Review B (Condensed Matter and Materials Physics), 2011. **84**(7): p. 075102.

35. Yongzhi, C., et al., *Perfect metamaterial absorber based on a split-ring-cross resonator.* Applied Physics A: Materials Science & Processing, 2011. **102**(1): p. 99-103.
36. Terracher, F. and G. Berginc. *Thin electromagnetic absorber using frequency selective surfaces*. in *IEEE Antennas and Propagation Society International Symposium. Transmitting Waves of Progress to the Next Millennium. 2000 Digest. Held in conjunction with: USNC/URSI National Radio Science Meeting (Cat. No.00CH37118)*. Place of Publication: Piscataway, NJ, USA; Salt Lake City, UT, USA. Country of Publication: USA.: IEEE Agilent Technol. Agilent Technol.
37. Jiaming, H., et al., *High performance optical absorber based on a plasmonic metamaterial.* Applied Physics Letters, 2010. **96**(25): p. 251104.
38. Seman, F.C., R. Cahill, and V. Fusco. *Performance Enhancement of Salisbury Screen Absorber Using a Resistively Loaded High Impedance Ground Plane*. in *Proceedings 4th European Conference on Antennas and Propagation (EuCAP 2010)*. Place of Publication: Piscataway, NJ, USA; Barcelona, Spain. Country of Publication: USA.: IEEE.
39. Jung, J.-Y., *Methods to achieve wavelength selectivity in infrared microbolometers and reduced thermal mass microbolometers* in *Electrical and Computer Engineering*2010, University of Texas at Austin: Austin, Tex.
40. Dumas, M.J., *A parametric exploration of the dual layer resistive microbolometer*, 2011, Florida Institute of Technology. p. 204.
41. Neikirk, D.P., W.W. Lam, and D.B. Rutledge, *Far-infrared microbolometer detectors.* International Journal of Infrared and Millimeter Waves, 1984. **5**(3): p. 245-278.
42. Weling, A.S., et al. *Antenna-coupled microbolometers for multispectral infrared imaging*. Place of Publication: Orlando, FL, USA. Country of Publication: USA.: SPIE - The International Society for Optical Engineering.
43. Jong Yeon, P., et al. *Fabrication and characterization of wavelength selective microbolometers using a planar self-aligned process for low deformation membranes*. Place of Publication: San Francisco, CA, USA. Country of Publication: USA.: SPIE - The International Society for Optical Engineering SPIE SPIE.
44. *http://www.ulis-ir.com/index.php?infrared-detector=ULIS-technology*.
45. Hongchen, W., et al., *IR microbolometer with self-supporting structure operating at room temperature.* Infrared Physics & Technology, 2004. **45**(1): p. 53-57.
46. Mottin, E., et al. *Enhanced amorphous silicon technology for 320times240 microbolometer arrays with a pitch of 35 mum*. Place of Publication: Orlando, FL, USA. Country of Publication: USA.: SPIE-Int. Soc. Opt. Eng. SPIE SPIE.
47. *Handbook of optical constants of solids*. 1985-1998, Orlando: Academic Press.
48. Jung, J.-Y., J.Y. Park, and D.P. Neikirk. *Wavelength-selective infrared detectors based on cross patterned resistive sheets*. 2009. Orlando, FL, USA: SPIE.